The Pennsylvania State University

The Graduate School

College of Engineering

ON THE IMPACT OF ELECTRODE GEOMETRY ON THE PIEZOELECTRIC PROPERTIES OF PZT 5A FIBERS

A Thesis in

Mechanical Engineering

by

Travis J. Carroll

© 2017 Travis J. Carroll

Submitted in Partial Fulfillment
of the Requirements
for the Degree of

Master of Science

May 2017

The thesis of Travis J. Carroll was reviewed and approved* by the following:

Zoubeida Ounaies
Professor of Mechanical Engineering
Thesis Advisor

Timothy W. Simpson
Paul Morrow Professor of Engineering Design and Manufacturing

Karen Thole
Professor of Mechanical Engineering
Distinguished Professor and Department Head

*Signatures are on file in the Graduate School.

Abstract

Lead zirconate titanate (PZT) is a ceramic material that can be classified as a smart material. This ceramic material exhibits a piezoelectric behavior, which means it is capable of transforming mechanical motion into an electrical charge and vice versa. In order to enhance its use in structural health monitoring systems, PZT, which is typically available in wafer form, is extruded into fibers and used to fabricate active fiber composites (AFCs). In a typical AFC, PZT fibers that are aligned side by side are embedded into an epoxy matrix. Since PZT exhibits both the direct and converse piezoelectric effects, AFCs can be used as actuators, sensors, or both. In order to exploit its piezoelectricity, interdigitated electrodes (IDEs) are applied to the AFC assembly. Due to the special design of the electrodes, the applied electric field is along the fiber's length, known as the '3' direction. Poling of the fibers is accomplished using these IDEs which results in a poling direction along their length; therefore, the directions of poling and mechanical actuation are the same. This directional manipulation is beneficial because the piezoelectric properties directed along the fiber's length, or '33' properties, are stronger than those through their thickness, or '31' properties. The piezoelectric response of AFCs is lower than that of bulk PZT due to various factors. Many models have been developed to predict the electromechanical behaviors of AFCs, and many studies have been performed on the mechanical properties of the material components in an AFC. However, very little research has been done on determining the piezoelectric properties of individual PZT fibers in an IDE setup without the presence of the epoxy matrix affecting them. The goal of this thesis is to characterize individual PZT fiber piezoelectric properties in an IDE setup in order to make recommendations for improving the design of AFCs, further optimizing their performance and applications.

To accomplish this goal, special attention is focused on how these fibers behave in an IDE setup in order to understand how they would respond electromechanically in an AFC. As previously mentioned, very little research has been done to characterize the piezoelectric properties of individual PZT fibers ex-situ using an IDE setup. To the best of our knowledge, only one research study on electromechanical characterization of

individual fibers in an IDE setup has been performed. In this study, done by a former group member, the values obtained through experimental processes and computer-modeling differed. The difference was believed to be caused mostly by various issues with the experimental processes developed at the time. Therefore, this research study extends the previous electromechanical characterization process of individual PZT fibers by improving different aspects of the experimental processes used. The rationale is that improving the experiments will help close the gap between experimentally obtained and model predicted piezoelectric coefficients.

The piezoelectric e_{33} and d_{33} coefficients are the main focus in this study. Experimental values for the induced stress coefficient (e_{33}) are determined for individual fibers in both a parallel electrode and IDE configuration. Various aspects of the experiments are altered in order to improve the reported coefficient values. Additionally, the induced strain coefficient, d_{33}, of individual fibers in an IDE setup is measured. Due to a lack of published results in the literature, finite element analysis (FEA) models are developed in order to validate the induced strain responses of a fiber in both a parallel electrode and IDE setup. Experimentally, e_{33} values are found to be 4.8 C/m^2 in a parallel electrode setup and 3.5 C/m^2 in an IDE setup. The IDE coefficient value was about 73% of the parallel electrode value, which was expected from the design characteristics of the IDE setup. Computer models of a fiber in a parallel electrode setup and IDE setup predict the d_{33} coefficients to be 256 pm/V and 185 pm/V respectively. Again, the IDE value is found to be about 72% of the parallel electrode value. Experimental results report an IDE d_{33} value of 166 pm/V. The main conclusion of this study confirms that the PZT fiber properties differ from those of bulk PZT; therefore, incorporating these fiber properties into AFC models will lead to more accurate predictions of AFC electromechanical behavior, driving the optimization of AFCs forward.

Table of Contents

List of Figures vii

List of Tables x

Acknowledgements xi

Chapter 1 Introduction 1

1.1 Introduction and Motivation for Study 1
1.2 Background on Piezoelectricity 8
1.3 Obtaining the Piezoelectric Constitutive Equations 14
1.3.1 Mechanical and Dielectric Property Equations 14
1.3.2 Piezoelectric Effect 15
1.3.3 Constitutive Equations 16
1.3.4 Tensor Simplification 18
1.4 Literature Review 19
1.4.1 AFC and IDE Design 19
1.4.2 AFC Performance Improvements 25
1.4.3 PZT Fiber Electromechanical Characterization 31
1.5 Scope of Thesis 37
1.5.1 Goals and Tasks 37
1.5.2 Organization of Thesis 38

Chapter 2 Experimental Characterization of the Piezoelectric Coefficients of PZT Fibers 39

2.1 Introduction and Fiber Materials 39
2.2 Experimental Equipment 42
2.2.1 Fiber Poling Equipment 42
2.2.2 Electromechanical Testing Equipment 42
2.2.3 Parallel Electrode Setup 45
2.2.4 IDE setup 46
2.3 General Poling Procedure 47
2.4 Electromechanical e_{33} Testing 48
2.4.1 Parallel Electrode e_{33} Testing Procedures 48
2.4.2 IDE e_{33} Testing Procedure 52
2.5 Electromechanical d_{33} Testing 55

Chapter 3 Determination of the Experimental Piezoelectric Coefficients: e_{33} and d_{33} 58

3.1 Parallel Electrode Experiments: e_{33} results 58
3.1.1 The Effect of Boundary Conditions 58
3.1.2 The Effect of the Pre-load Magnitude 62
3.1.3 The Effect of Electrode Contact 63
3.2 Interdigitated Electrode Experiments: e_{33} results 66

3.2.1 The Effect of Boundary Conditions 66
3.2.2 The Effect of Varying Fiber Properties 69
3.2.3 A New IDE Design 71
3.3 Interdigitated Electrode Experiments: d_{33} results 74
3.4 Calculation of g_{33} Coefficient 77

Chapter 4 FEA Modeling of PZT Fibers 80

4.1 Modeling a Fiber using Two Electrode Configurations: Parallel and IDE 80
4.1.1 Parallel Electrode Fiber Model 80
4.1.2 IDE Fiber Model 83
4.2 Comparisons 89
4.2.1 Comparison of Parallel Model to IDE Model Results 89
4.2.2 Comparison of IDE d_{33} Experimental to Model Values 90

Chapter 5 Conclusions and Recommended Future Work 92

5.1 Summary of Work 92
5.2 Conclusions 93
5.3 Suggested Future Work 99

References 101

Appendices 105

Appendix A IDE Screen Printing Process 105

Appendix B Fiber-Optic Sensor Calibration 109

Appendix C Material Properties Programmed into ABAQUS Models 112

Appendix D Scanning Electron Microscopy Imaging of the PZT Fiber Tips 113

List of Figures

Figure 1.1: General active fiber composite (AFC) schematic 3

Figure 1.2: Illustration of the electrical field lines for parallel electrodes (A) and IDEs (B) [16] 6

Figure 1.3: PZT paraelectric cubic cell structure above T_c (left) and offset-center unit cell structure below T_c (right) [27] 9

Figure 1.4: Phase diagram of PZT [28] 10

Figure 1.5: Dipole arrangement during poling: (A) original dipolar domains are random in the material, (B) application of electric field causes dipoles to orient with field direction, (C) dipoles “relax” once the field is removed [16] 11

Figure 1.6: Hysteresis loop behavior in a ferroelectric material [16] 12

Figure 1.7: Example polarization directions of the tetragonal and rhombohedral unit cell phases [28] 13

Figure 1.8: First AFC concept [2] 20

Figure 1.9: Conventional parallel electrode (Top) and interdigitated electrode (Bottom) [7] 21

Figure 1.10: Effect of increasing electrode gap on piezoelectric response estimated using FEM and Rayleigh-Ritz model [7] 23

Figure 1.11: Finite elements model of a fiber in an epoxy matrix [9] 24

Figure 1.12: AFC experimental results in comparison with model values [9] 25

Figure 1.13: S-glass fibers embedded within the matrix (left) and glass-ply laminated AFC (right) [29] 26

Figure 1.14: Representative volume element of an AFC incorporating a contact angle [30] 30

Figure 1.15: Effective piezoelectric constants with respect to contact angle variations [30] 31

Figure 1.16: Parallel electroded composite created to determine the d_{33} coefficient of PZT fibers [14] 33

Figure 1.17: Radially poled hollow PZT fiber [12] 34

Figure 1.18: Individual fiber piezoelectric e_{33} coefficients found between parallel electrodes (a) and IDEs (b) [16] 36

Figure 2.1: PZT fibers supplied by Advanced Cerametrics Inc. 41

Figure 2.2: TA Instruments DMA used for e_{33} testing (a), tensile/compression grips (b), 3-point bending grips (c) 43

Figure 2.3: Electromechanical testing equipment setup 44

Figure 2.4: Parallel electrode setup concept 45

Figure 2.5: IDE assembly setup concept 46
Figure 2.6: Wyckoff IDE design (bottom) compared to AFC IDE design (top) [16] 47
Figure 2.7: Parallel electrode experimental setup in the DMA 50
Figure 2.8: e_{33} measurement process 52
Figure 2.9: IDE experimental setup in the DMA 54
Figure 2.10: d33 measurement process 57
Figure 3.1;Hysteresis behavior of a PZT fiber in a parallel electrode setup tested at 0.1 Hz under a 1 MV/m AC electric field with a +1 MV/m DC offset applied 60
Figure 3.2: Parallel electrode e_{33} results using a constant stress poling boundary condition 60
Figure 3.3: Parallel electrode test e_{33} results using a 4 MPa testing pre-load 63
Figure 3.4: Parallel electrode test e_{33} results using silver-tipped fibers and a 2 MPa pre-load stress 65
Figure 3.5: Hysteresis behavior of a PZT fiber in an IDE assembly tested at 0.1 Hz under a 1MV/m AC electric field with no DC offset applied 67
Figure 3.6: IDE test e_{33} results using a constant stress poling boundary condition 68
Figure 3.7: IDE assembly installed into the DMA for testing 69
Figure 3.8: IDE test e_{33} results using a 45 mm testing gap 70
Figure 3.9: A comparison of the new IDE design to the old design 71
Figure 3.10: New IDE test e_{33} results using a 40 mm gap 72
Figure 3.11: Averaged IDE test d_{33} coefficient results 75
Figure 3.12: Optical microscope images of an IDE electrode (left) and an IDE electrode gap (right) 77
Figure 4.1: Parallel electrode fiber FEA model 82
Figure 4.2: Displacements (shown in meters) of the meshed elements in the parallel electrode setup 83
Figure 4.3: IDE RVE: Red areas act as the positive electrodes and blue as the ground electrodes. Dashed outlines indicate electrodes on the bottom of the RVE 85
Figure 4.4: Mesh refining for IDE RVE 87
Figure 4.5: Predicted d_{33} values in relation to mesh refinements: d_{33} values settle at around 100000 mesh elements 88
Figure 4.6: Electric field lines in the parallel electrode model (top) and IDE model (bottom) 89
Figure A.1: IDE printing screens 105
Figure A.2: Screen printer setup 106

Figure A.3: IDE printing screen and frame 107
Figure B.1: PZT fiber in an IDE aligned with the fiber-optic sensor probe 109
Figure B.2: MTI-Instruments fiber-optic sensor..... 109
Figure B.3: Sensor calibration curve 111
Figure D.1: PZT fiber partially fractured tip surfaces (a) and silver-tipped PZT fiber tip (b)..... 113

List of Tables

Table 1.1: Voigt convention rules for matrix notation [26] 18

Table 1.2: Materials and Dimensions of a typical AFC [8] 28

Table 1.3: Peak actuation strains for varying p/h ratios [8] 29

Table 2.1: Electromechanical properties of interest for bulk PZT 5A [31] 40

Table 3.1: Experimental and model predicted values from a previous study [16] 59

Table 3.2: Comparing the new poling condition parallel e_{33} value to previously published data 61

Table 3.3: Induced stress coefficients measured from each parallel electrode experimental alteration implemented 65

Table 3.4: Comparing the new poling condition IDE e33 value to previously published data 68

Table 3.5: Induced stress coefficients measured from each IDE experimental alteration implemented 73

Table 4.1: Boundary conditions applied to the parallel electrode model 82

Table 4.2: Boundary conditions applied to the IDE model 85

Table 4.3: Mesh refinement data 88

Table C.1: General material properties for ABAQUS models 112

Acknowledgements

I would first like to express my gratitude to Dr. Zoubeida Ounaies. Through your drive towards excellence, you have continuously pushed me to expand the limits of my knowledge and research productivity and never ceased to offer up wisdom and guidance during my pursuit towards my Master of Science degree. I truly could not have accomplished this without your help.

I would like to thank Dr. Timothy Simpson for your time and patience acting as my faculty reviewer. Your comments have been much appreciated. I would also like to express my thanks to my colleagues in the Electro-Active Materials Characterization Lab. You all have been very supportive and insightful concerning my research, providing me with excellent personal experiences that helped guide my experimental processes. I wish you all the very best and brightest futures the world has for you.

Lastly and most importantly, I would like to express my love and gratitude to my family. Your love and support has given me the strength to push the bounds of life and reach higher levels of personal success. To my parents, I would like to thank you for helping provide the opportunity to study at The Pennsylvania State University and also for instilling in me a hunger for excellence. To my grandmother, I would like to thank you for acting as a third parent, expecting from me nothing but the best that I could give. To my siblings, I would like to thank you for making life interesting. I would like to dedicate this thesis to my parents and grandmother.

This research was supported in part by the National Science Foundation under Grant No. CMMI 1437437.

Chapter 1
Introduction

1.1 Introduction and Motivation for Study

In this thesis, experimental determination of the coupled electromechanical properties of individual piezoelectric ceramic fibers is performed. Specifically, this research study focuses on characterizing the piezoelectric ceramic fibers under two configurations: (1) parallel electrode and (2) interdigitated electrode configurations. Results are used to inform the modeling and design of active fiber composites.

Piezoelectric ceramic fibers are a type of smart material. These materials, according to Takagi, can be defined as "materials which respond to environmental changes at the most optimum conditions and manifest their own functions according to the changes" [1]. In other words, smart materials are materials that are capable of transforming energy from one physical domain into energy in another physical domain. For example, piezoelectric materials are capable of transforming mechanical motion into electrical energy and vice versa. Smart materials, specifically piezoelectric materials, have been studied since the late 19^{th} century, but new applications of these types of materials are constantly being discovered and utilized. One such application is the use of piezoelectric materials in smart composites known as piezoelectric (or active) fiber composites [2, 3, 4].

Active fiber composites, or AFCs, are composite materials that exhibit the piezoelectric effect. The direct piezoelectric effect refers to the generation of electrical energy from mechanical deformation. A material exhibiting this type of piezoelectricity is known as a sensor. The converse piezoelectric effect refers to the induced mechanical deformation of a material under an electrical load. A material exhibiting this type of piezoelectricity is known as an actuator.

First designed by Hagood and Bent [2], AFCs were created as a solution for enhanced structural actuation using a piezoceramic material known as lead zirconate titanate (PZT). Originally, individual monolithic PZT wafers were used in structural monitoring and actuation applications. Hagood and Bent explain that these wafers were typically either surface bonded to the structure or embedded within the composite material of the structure [5, 6] for sensing and actuation purposes. The practice of surface bonding the wafers was extremely time-consuming considering the small wafer sizes often used. For example, Hagood *et al*. [7] utilized wafers that were 6.l mm x 9.l4 mm x 0.1905 mm in dimension. Additionally, surface bonding sites of the piezoceramic wafers were mainly limited to flat surfaces on the structure because of the brittle nature of the wafers. Embedding the wafers only caused more problems with unnecessary stress concentrations in the parent material. A study by Crawley and de Luis [6] showed that composite materials with piezoceramic wafers embedded within them actually exhibited reductions in ultimate strength by up to 20 percent of the parent material. To address these challenges, Hagood and Bent [2] developed the AFC, which utilized the same piezoceramic material as the wafers, but in fiber form. The AFCs were an answer to the lack of scalability and rigidity of the PZT wafer. Scaling up the size of the sensor/actuator was accomplished by simply including more fibers into the AFC. Additionally, the PZT fibers exhibited a much greater flexibility than the wafers, creating the possibility of "conformable" actuators and sensors [2], negating their "flat surface only" limitation.

Active fiber composites today are composed of four main components: (1) piezoceramic fibers, (2) an epoxy matrix, (3) Kapton polyimide tape, and (4) electrodes [3, 4]. Multiple fibers of the same length are embedded next to one another in a unidirectional fashion inside of an epoxy matrix. The unidirectional layout of the fibers creates the possibility of orthotropic actuation. In the AFCs designed by Hagood and Bent [2], these fibers were made from PZT, which is the same material used in the AFC designs currently due to its strong electromechanical performance. For a typical modern AFC, the PZT fibers used are fabricated to a diameter of about 250 μm [8]. The epoxy

matrix surrounding the aligned fibers provides a structure for the fibers to hold them in place during use; it also enhances the mechanical integrity of the fibers while simultaneously maintaining a flexible nature. Electrical connections to the fibers are made via two electrode layers that sandwich the combination fiber-epoxy material. For these two electrode layers, specially designed interdigitated electrodes (IDEs) are used. IDEs are designed to have evenly spaced electrode "fingers" along the length of the fiber. The fingers alternate in electrical polarity from positive to negative repeatedly. Originally, Bent and Hagood [3] etched the IDEs onto a copper/Kapton thin film, but today, the IDEs are typically screen printed onto a Kapton polyimide tape, and the Kapton-electrode assemblies are adhered to the epoxy-fiber matrix. The electrodes placed on top and bottom of the assembly are designed to be mirror images of one another. Placing the fibers between the mirrored electrodes essentially creates an electric field along the length of the fiber. The combination of these four components allows for AFCs to be much more conformable to application surfaces than ordinary piezoceramic wafers. A basic schematic of a typical AFC can be seen in Figure 1.1.

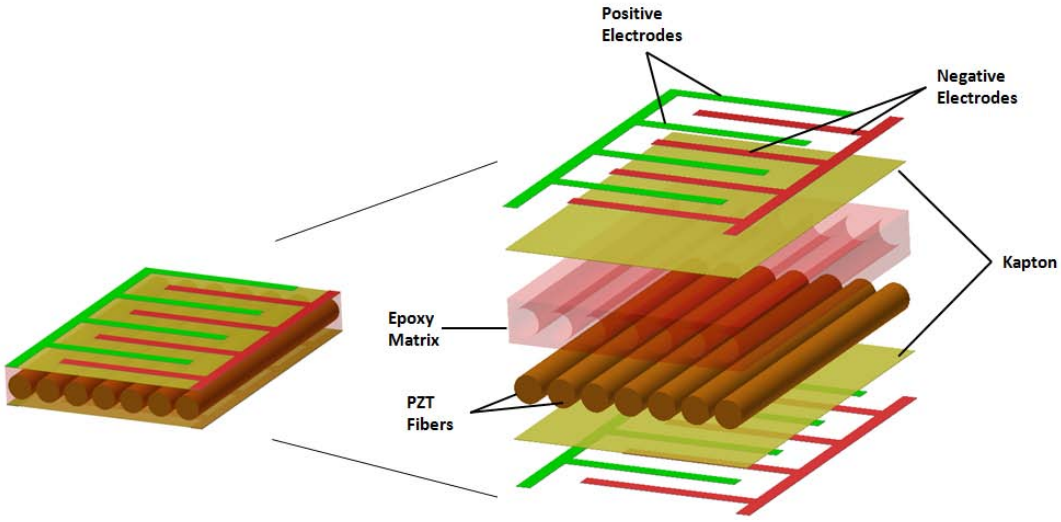

Figure 1.1: General active fiber composite (AFC) schematic

Over the years since their emergence, AFCs have been modeled and experimented with many times as researchers try to optimize the composite material's piezoelectric performances [3, 9, 10]. In most studies, different designs were studied by varying the

epoxy matrix material used, varying the electrode design or dimensions of the AFC, or varying the sizes of the fibers used. In its early stages, the AFC utilized parallel electrodes. A drive for a different mode of actuation in the fibers inspired Hagood *et al.* to create the IDE design [7]. Through modeling and experimentation, they were able to characterize the effects that different design criteria would have on the performance of a specific IDE design. This led to the modeling and experimentation of AFCs between IDEs for their electromechanical behaviors [3]. Next, the fiber properties and the epoxy matrix properties were considered for design optimization. For most of the studies, the properties of the PZT fibers used in the AFC models were drawn from the properties of bulk PZT since bulk PZT properties have been extensively published. However, the manufacturing process of PZT fibers causes changes within the PZT material itself, which can create large differences in material properties between the fibers and the bulk material [11, 12]. Since the epoxy matrix is meant to protect the fibers, studies were done to determine the mechanical properties of individual fibers [11, 13]. Results showed that increased porosity of the fibers did have an effect on their mechanical properties.

Since the mechanical properties and microstructures of PZT fibers differed from those of bulk PZT, it was expected that the dielectric and piezoelectric properties of the fibers would therefore also be different. It was originally estimated that a fiber's electromechanical properties would be about 65-75% of PZT bulk material properties [12]. Studies such as the one by Nelson *et al.* [14] have been done to determine the electromechanical properties of PZT fibers. The issue, however, is that most of these studies are carried out on fibers already embedded into the AFC composite or in some other type of composite assembly. The composite assemblies are tested electromechanically, and the dielectric and piezoelectric properties of the fibers are extracted from the data gathered. These studies do not actually test properties of individual fibers, but rather fibers that are already being influenced by the surrounding fibers, epoxy, and electrodes.

There are a few studies that have been done to characterize individual fiber electromechanical properties. In a study by Heiber *et al.* [15], individual PZT fibers were

tested in order to determine their free-strain "butterfly" and polarization loops. In this study, fibers were cut to a length of about 3.5 mm, and one of the fiber's tips was placed vertically into a hole on a Poly(methyl methacrylate) (PMMA) disk-shaped holder while electric fields were applied. Although this study does in fact test individual fibers, it only provides information on the polarization properties and free strain tendencies of PZT fibers without mention of a single fiber's specific piezoelectric coefficients in comparison to those of bulk PZT. In another study by Guillot *et al.* [12], individual fibers were tested for their electrical energy generation due to mechanical deformation. However, the fibers tested were hollow fibers, not solid fibers like those found in AFCs. The hollow fibers were dipped into a nickel chloride and sodium hypophosphite solution in order to apply electrodes onto the inner and outer surface of the fiber. This style of electroding creates a significant difference between the electromechanical behavior of one of these hollow fibers and the behavior of a solid PZT fiber found in an AFC. Rather than investigating their properties in an IDE configuration, the hollow fibers are tested radially using essentially a parallel electrode configuration. Therefore, the electromechanical behavior of individual fibers from an AFC cannot be related to the behavior of the hollow fibers from this study.

Parallel electrodes and IDEs are used to create directionally oriented electrical fields between the electrodes. However, the electrical field lines they create are not similar. A parallel electrode configuration, as seen in Figure 1.2 (A), creates an electric field in which all of the field lines are uniform, unidirectional, and perpendicular to the surfaces of the electrodes. An IDE configuration, illustrated in Figure 1.2 (B), does not create a uniform electric field. As before, the electric field lines "leave" and "enter" the electrodes perpendicular to the electrode surfaces. However, since the positive and negative electrode surfaces are in plane, the electric field lines bend in order to leave the positive electrode and enter the negative electrode. Since the field lines follow elliptical paths, a net electric field flowing from the positive to the negative electrode is created. This net field, though, is less in magnitude than that of parallel electrodes. The differences in electric fields created by these two electrode configurations is the main

reason why PZT fibers found in AFCs need to be individually studied using an IDE setup in order to properly characterize their electromechanical properties.

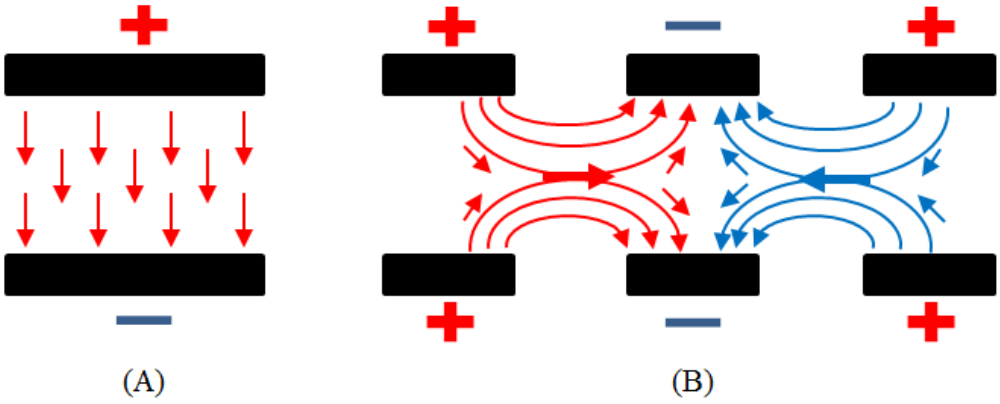

Figure 1.2: Illustration of the electrical field lines for parallel electrodes (A) and IDEs (B) [16]

To date and to the best of our knowledge, the only study to investigate individual PZT fibers in an IDE setup is that done by Nicholas Wyckoff, a former group member, [16], where he characterized the mechanical, dielectric, and piezoelectric properties of individual PZT fibers using both a parallel electrode configuration and an IDE configuration. More specifically, individual PZT fibers were successfully tested without the presence of an epoxy matrix using an IDE configuration, and their dielectric and piezoelectric behaviors were measured. Wyckoff found that a fiber's properties differed in comparison to the properties of bulk PZT. More significantly, he found through experimentation and FEA modeling that various mechanical and piezoelectric properties of the PZT fibers did not all follow the general assumption that fiber properties are about 65-75% [12] of the of their published bulk PZT property counterparts.

All of the research done with AFCs has been driven by a need for enhanced performance as required by engineering applications. As mentioned previously, AFCs can be used as sensors. Most commonly, they are applied to structural health monitoring systems [17, 18, 19, 20]. Many engineered structures are designed to withstand vibration or even operate under a controlled vibration motion. However, excessive vibration of a structure could lead to its catastrophic failure. Therefore, continuous monitoring of the

structure's "health" is highly desired. This was the motivation for mounting AFCs onto surfaces of interest of a structure or within specific members of a structure. As the structure deforms, the AFC simultaneously deforms, generating a voltage that can be recorded and mapped. The data from the AFC provides information on whether or not the structure is deforming within its allowable limits or if it is approaching failure.

In addition to sensing applications, AFCs can be used as actuators. Actuation applications have been much more diverse than sensing applications since actuation can be utilized in many different ways. The majority of applications, though, involve vibration control [20, 21, 22, 23, 24]. Due to an AFC's ability to act as both a sensor and an actuator, applications of AFCs can involve using the material as both sensors and actuators in the same system, commonly referred to as self-sensing actuators. An example of this type of application was investigated by using AFCs embedded into the wings of an unmanned aerial vehicle (UAV) [25]. For this application, the fiber composites were able to deform the shape of the wings in order to achieve optimal lift forces. Additionally, the fiber composites could also act as structural sensors for the wings, monitoring their performance.

For many years, focus was directed toward optimizing the performance of AFCs for their numerous applications. However, even though countless experiments and applications have been designed and studied, a fundamental problem still exists. Data that is gathered experimentally and data that is gathered through modeling of the systems do not align. As mentioned previously, models of AFCs assign property values to the PZT fibers based on the values of a bulk PZT material. This means that the fiber properties used in these models are first guesses and are potentially not indicative of a fiber's true electromechanical behavior. While almost every other parameter of the AFC has been studied, there has been a significant lack of focus on characterizing the true electromechanical properties of individual PZT fibers. This gap in the literature is the motivation for the research in this thesis. In this study, piezoelectric behavior of individual PZT fibers is systematically studied in an effort to fill the void in AFC research and help drive AFC optimization forward.

1.2 Background on Piezoelectricity

The coupling of the mechanical and electrical domains in piezoelectric materials is achieved through structural polarization changes within the piezoelectric material, which is related to the unit cell structure of the material. Crystalline unit cell structures can be separated into two major groups: centrosymmetric and noncentrosymmetric [26]. Piezoelectric material unit cells are noncentrosymmetric. This means that the unit cell structure of the material does not have a center of symmetry. Furthermore, piezoelectric materials can be divided into polar and non-polar sub groups. Piezoelectric polar materials, also known as pyroelectric materials, exhibit a unique polar axis and are capable of exhibiting a spontaneous polarization. Non-polar piezoelectric materials are also capable of exhibiting spontaneous polarizations, but only when an external electric field or mechanical load is applied to the material.

A special subset of pyroelectric materials, known as a ferroelectric material, is a material in which the direction of the spontaneous polarization of the material can be altered by applying an electric field. When an electric field is applied to a ferroelectric material, the spontaneous polarization directions in each crystalline domain align with the field and remain in their new orientations when the field is removed. PZT is a piezoelectric material that exhibits this ferroelectric behavior below its Curie temperature (T_c). When PZT crystallizes, it crystallizes in the Perovskite crystal structure, which typically follows a general formulation of ABO_3 where A represents lead (Pb), B represents either zirconium or titanium (Zr or Ti), and O represents oxygen (O). When PZT is above its T_c, its unit cell structure is in a simple cubic structure, also known as the paraelectric phase. In this phase shown on the left in Figure 1.3, the lead atoms form the corners of a cube, the oxygen atoms are in the centers of each face of the cube, and the small zirconium or titanium atoms are exactly in the center. There is a central symmetry in the unit cell so that there is no dipole moment present; hence, this phase is centrosymmetric and not piezoelectric. However, when PZT material is below its Curie temperature, each unit cell becomes noncentrosymmetric and experiences a dipole moment due to a spontaneous offset of the Zi or Ti atom from the center of the cell. Even though the unit cell is no longer electrically neutral, this offset-center structure is the unit

cell's lowest energy configuration; therefore, it is stable. One of the common types of offset-center unit cells that PZT exhibits is the tetragonal unit cell structure and is also shown in Figure 1.3 on the right.

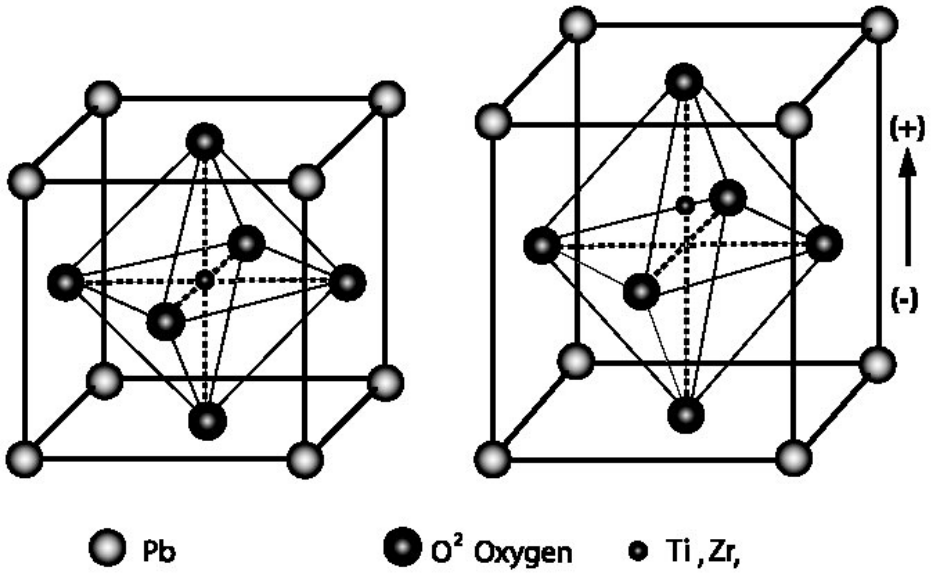

Figure 1.3: PZT paraelectric cubic cell structure above T_c (left) and offset-center unit cell structure below T_c (right) [27]

The tetragonal unit cell structure is one of two possible structures that PZT crystallizes into below the Curie temperature. The other structure is known as the rhombohedral orientation. The unit cell structure that PZT will crystallize into below T_c is dependent on the composition of the material. There exists also a slight temperature dependence, but only at temperatures near the Curie temperature of the material. Figure 1.4 shows the crystalline orientation phase diagram of PZT with respect to both temperature and composition. The composition axis refers to the amount of $PbZrO_3$ and $PbTiO_3$ present together in the parent material being studied. The top region of the diagram represents the temperatures at which certain compositions are above Curie temperature, and the crystals are therefore in the paraelectric cubic phase (P_c). Then, cooling below Curie temperature, the crystals in the material will either take on the ferroelectric tetragonal structure (F_T) or ferroelectric rhombohedral structure (F_R) mentioned earlier. The resulting structure taken depends on the composition of the

material. Materials that have higher $PbZrO_3$ concentrations will take on the F_R structure whereas materials with higher $PbTiO_3$ will take on the F_T structure.

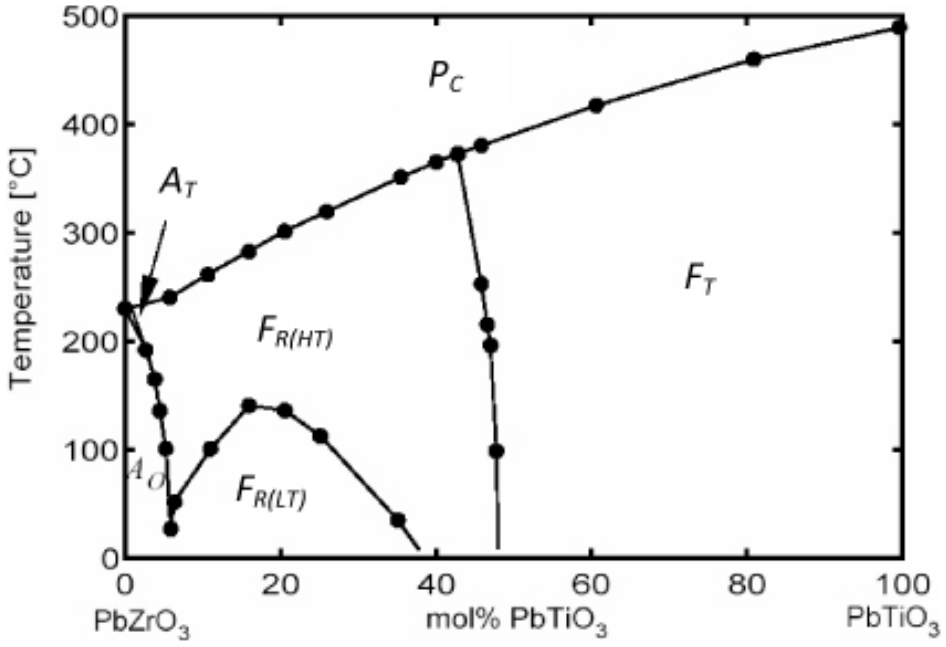

Figure 1.4: Phase diagram of PZT [28]

The individual crystals each have a spontaneous polarization creating dipoles in the material. Unit cells with the same dipolar orientation that are next to each other form ferroelectric domains. These domains, however, are usually naturally randomly oriented within the material. Therefore, even though each domain has a spontaneous polarization, the overall parent material will have a neutral polarization. This is because ferroelectric domains with opposing dipolar directions will cancel each other out, resulting in a net polarization of zero. However, these dipolar domains can be reoriented through a process called poling. When a material is being poled, a high direct current (DC) electric field is applied through the material. The dipolar regions then reorient themselves to be in line with the electric field. If a high enough field is applied for a long enough period of time, the reorientation of the dipolar regions can become semi-permanent. When the high DC electric field is removed, the dipoles that were completely in line with the direction of the field "relax," which means that they slightly rotate out of line with the direction of the previously applied field, but they do not reorient themselves back to their original directions. The result of these slight rotations is that the dipoles remain mostly oriented

with the applied field direction. This creates a collective spontaneous polarization, known as remnant polarization, through the whole material. A diagram of the poling process can be seen in Figure 1.5.

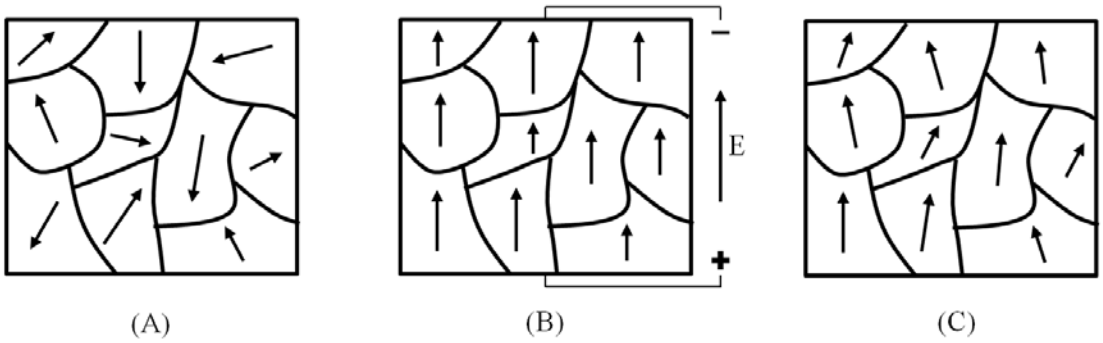

Figure 1.5: Dipole arrangement during poling: (A) original dipolar domains are random in the material, (B) application of electric field causes dipoles to orient with field direction, (C) dipoles "relax" once the field is removed [16]

The dipolar behavior of a ferroelectric material gives rise to a polarity property of the material known as a ferroelectric hysteresis loop, which implies that a maximum remnant polarization can be achieved if a high enough electric field is applied. If a sufficiently high enough electric field is applied to a material, then the material will reach a saturation polarization. When the field is removed, the dipoles slightly relax, as discussed, resulting in a remnant polarization, which is always lower than the saturation polarization. Due to the ferroelectric nature of the dipoles, the net polarization in the material can actually be brought back to zero if a certain strength electric field, known as the material's coercive field (E_c), is applied in the direction opposite that of the poling field. Then, if this opposite field is strong enough, a remnant polarization equal to the one achieved through poling can be again achieved in the opposite direction via the same dipolar movement mechanism. This ability to switch polarization directions in a material from varying electric field strengths and directions is due to ferroelectricity, and a diagram outlining this behavior can be found in Figure 1.6.

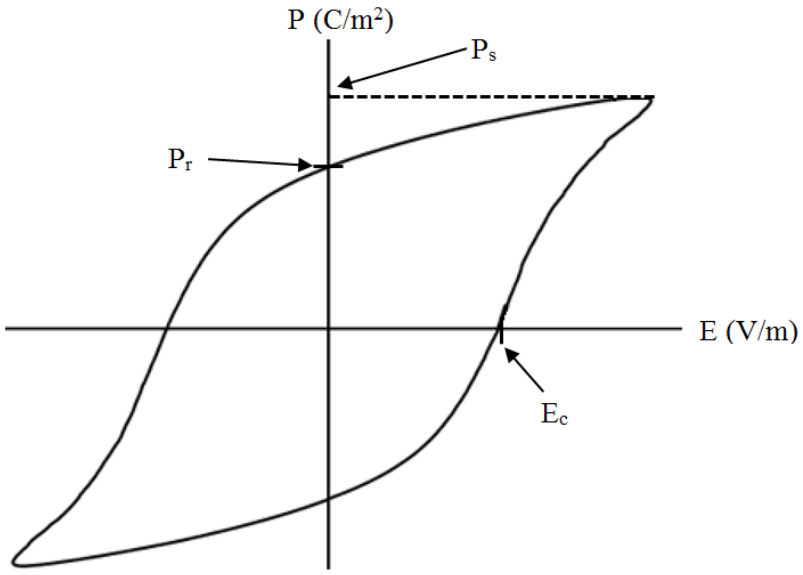

Figure 1.6: Hysteresis loop behavior in a ferroelectric material [16]

The purpose of poling a ferroelectric material in the first place is that a poled material exhibits amplified piezoelectric properties. From an electromechanical viewpoint, amplified piezoelectric properties in a material leads to greater magnitudes of actuation under smaller electric field loads, or greater electrical energy generation values from smaller deformations of the material. Thus, poling a ferroelectric material is highly desirable, but the material itself can provide limitations on how poling can be done. Recall that in PZT, the crystals will take on a tetragonal or rhombohedral unit cell structure depending on the composition of the material. In the tetragonal phase, the central Zr or Ti atom of a unit cell offsets towards one of the body center oxygen atoms. Since there are 6 body center oxygen atoms (6 faces), the tetragonal phase can be poled in 6 directions. In the rhombohedral phase, the central Zr or Ti atom offsets towards one of the corner Pb atoms. Since there are 8 corner Pb atoms (8 corners), the rhombohedral phase can be poled in 8 directions. Figure 1.7 shows examples of poling directions in tetragonal and rhombohedral phase structures.

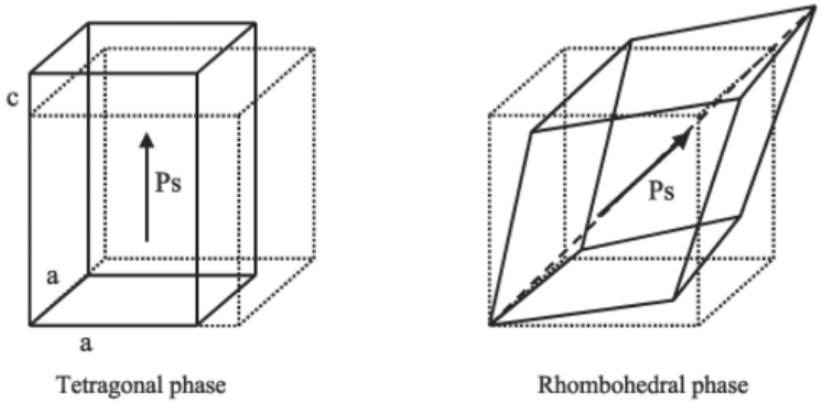

Figure 1.7: Example polarization directions of the tetragonal and rhombohedral unit cell phases [28]

Limitations on poling directions within the crystal unit cells can be problematic since the crystalline unit cells themselves are randomly arranged in the material. For example, when an electric field is applied to PZT with crystals of the tetragonal phase, the crystal "faces" would not all be perpendicular with the field; so, the polarization of the crystals would not truly align with the field, resulting in a lower overall polarization than one would expect. Thus, the more potential poling directions available in a material, the more likely a maximum remnant polarization can be reached.

For PZT, it is possible to achieve more than the 6 or 8 potential poling directions of its two common crystalline phases by creating PZT of a very specific composition. On the phase diagram in Figure 1.4, the dividing boundary between the tetragonal and rhombohedral phases is known as the morphotropic phase boundary [26]. Along this compositional boundary, the free energies of both the tetragonal and rhombohedral phases are the same, so both phases can exist simultaneously. This means that unit cells can switch between tetragonal and rhombohedral phases during the poling process, creating effectively 14 different potential poling directions in the material. PZT samples with a composition along the morphotropic phase boundary are therefore highly desired for application purposes.

1.3 Obtaining the Piezoelectric Constitutive Equations

This section provides the basic derivation of the important piezoelectric constitutive equations for this study. Equations are given in tensor notation, assuming the reader has previous understanding of tensor notation [26].

1.3.1 Mechanical and Dielectric Property Equations

Many materials are linearly elastic materials up to a certain stress. This linear elastic relationship is described by Hooke's law [26] given in Equation (1.1). Here, S_{ij} (m/m) represents the second-rank strain tensor, s_{ijkl} (m^2/N) represents the fourth-rank elastic compliance tensor, and T_{kl} (N/m^2) represents the second-rank stress tensor.

$$S_{ij} = s_{ijkl}T_{kl} \tag{1.1}$$

Hooke's Law can also be written in an inverse relationship shown in Equation (1.2) where c_{ijkl} (N/m^2) represents the fourth-rank elastic stiffness tensor.

$$T_{ij} = c_{ijkl}S_{kl} \tag{1.2}$$

PZT not only exhibits linear elasticity, but it is a dielectric material meaning it can be polarized by applying an electric field. A simple relationship between polarization and electric field is shown in Equation (1.3).

$$P_i = \chi_{ij}E_j \tag{1.3}$$

In this equation, P_i (C/m^2) represents the second-rank polarization tensor, χ_{ij} (F/m) represents the second-rank dielectric susceptibility tensor, and E_j (V/m) represents the first-rank applied electric field vector. PZT's dielectric behavior, like all other dielectric materials, is characterized by its permittivity, which can be derived from its dielectric displacement, polarization, and applied electric field. This relationship is shown in Equation (1.4).

$$D_i = \varepsilon_0 E_i + P_i \tag{1.4}$$

Here, D_i (C/m^2) represents the first-rank dielectric displacement (or charge density) vector and ε_o (F/m) represents the permittivity of free space. ε_o is a scalar constant that equals 8.85e^{-12} F/m. Using Equations (1.3) and (1.4), the dielectric displacement can be rewritten as:

$$D_i = \varepsilon_0 E_i + \chi_{ij} E_j = \varepsilon_0 \delta_{ij} E_j + \chi_{ij} E_j = (\varepsilon_0 \delta_{ij} + \chi_{ij}) E_j = \varepsilon_{ij} E_j \tag{1.5}$$

In Equation (1.5), ε_{ij} (F/m) represents the material's second-rank dielectric permittivity tensor and δ_{ij} represents Kronecker's symbol ($\delta_{ij} = 1$ for $i = j$, $\delta_{ij} = 0$ for $i \neq j$) [26]. However, the material's relative dielectric permittivity, or dielectric constant, is most commonly used. Equation (1.6) shows how to get a material's dielectric constant.

$$\varepsilon_r = \frac{\varepsilon_{ij}}{\varepsilon_0} \tag{1.6}$$

1.3.2 Piezoelectric Effect

Piezoelectric materials like PZT are materials that are capable of being polarized not only by the application of an electric field, but also through the application of a mechanical load. This behavior is known as the direct piezoelectric effect [26]. There is a linear relationship between the stress of the load applied and the resulting charge density generated in the material. This relationship is shown in Equation (1.7).

$$D_i = d_{ijk} T_{jk} \tag{1.7}$$

Here, d_{ijk} (C/N) represents a third-rank piezoelectric coefficient tensor. Additionally, materials that exhibit the piezoelectric effect exhibit the ability to mechanically deform when an external electric field is applied. This behavior is known

as the converse piezoelectric effect [26]. The linear relationship of the strain induced in a material due to an electric field is:

$$S_{ij} = d_{kij}E_k \tag{1.8}$$

where $d_{kij} = d_{ijk}{}^T$. This relationship, however, is only linear at low electric fields. Even though the piezoelectric *d* coefficients for the direct and converse effect are thermodynamically identical, the converse effect is more frequently referenced; so, this piezoelectric coefficient is commonly referred to as the induced strain coefficient.

1.3.3 Constitutive Equations

PZT is a material that experiences both dielectric and piezoelectric effects simultaneously. Therefore, both mechanical and electrical responses need to be coupled together in order to capture the electromechanical behavior of PZT. The coupled behavior is shown in Equations (1.9) and (1.10).

$$S_{ij} = s_{ijkl}T_{kl} + d_{kij}E_k \tag{1.9}$$

$$D_i = d_{ijk}T_{jk} + \varepsilon_{ij}E_j \tag{1.10}$$

Equations (1.9) and (1.10) together are known as the strain-charge form of a material's piezoelectric constitutive equations, and they utilize the piezoelectric induced strain coefficient (*d)*. Under the converse effect, pure piezoelectric strain can only be achieved through a zero stress condition. Under this type of condition, it is seen that the strain coefficient is solely a function of the strain induced from an applied electric field, shown in Equation (1.8). For the direct effect, pure piezoelectric charge can only be achieved through a zero electric field condition, shown in Equation (1.7).

The strain-charge equations are obtained through a series of thermodynamic derivations with specifically chosen independent variables. By choosing different

independent variables, other forms of piezoelectric constitutive equations are obtainable [26]. For this study, the other major form of piezoelectric constitutive equations used is in the stress-charge form. The stress-charge form can be seen in Equations (1.11) and (1.12).

$$T_{ij} = c_{ijkl}S_{kl} - e_{kij}E_k \tag{1.11}$$

$$D_i = e_{ijk}S_{jk} + \varepsilon_{ij}E_j \tag{1.12}$$

The stress-charge form of the constitutive equations utilizes the piezoelectric *e* coefficient, commonly known as the induced stress coefficient. It can be seen under the converse effect that a pure piezoelectric stress can only be achieved through a zero strain condition. Applying a zero strain condition, therefore, shows that the induced stress coefficient is solely a function of the stress induced in a material from an applied electric field, shown in Equation (1.13). Under the direct effect, a pure piezoelectric charge can only be obtained through a zero electric field condition, shown in Equation (1.14).

$$T_{ij} = -e_{kij}E_k \;\rightarrow\; e_{kij} = \frac{-T_{ij}}{E_k} \tag{1.13}$$

$$D_i = e_{ijk}S_{jk} \;\rightarrow\; e_{ijk} = \frac{D_i}{S_{jk}} \tag{1.14}$$

Since PZT also exhibits the direct piezoelectric effect and is often used for sensing applications, another form of the piezoelectric constitutive equations used is the strain-voltage form equations. These can be seen in Equations (1.15) and (1.16). The strain-voltage equations utilize the piezoelectric *g* coefficient, commonly referred to as the voltage coefficient. It can be seen for the direct effect that under a zero electric displacement condition, the voltage coefficient is solely a function of the electric field induced from an applied stress, shown in Equation (1.17).

$$S_{ij} = s_{ijkl}T_{kl} + g_{kij}D_k \tag{1.15}$$

$$E_i = -g_{ijk}T_{jk} + \beta_{ij}D_j \tag{1.16}$$

$$E_i = -g_{ijk}T_{jk} \;\rightarrow\; g_{ijk} = \frac{-E_i}{T_{jk}} \tag{1.17}$$

1.3.4 Tensor Simplification

Tensor notation of the constitutive equations can be simplified through an understanding of tensor symmetry and using the nomenclature rules of the Voigt convention. These rules can be found in Table 1.1. Using the Voigt convention for the strain-charge form of the constitutive equations, the simplified tensor notations are shown in Equations (1.18) and (1.19). Similarly, for the stress-charge form, the simplified tensor notations can be seen in Equations (1.20) and (1.21).

Table 1.1: Voigt convention rules for matrix notation [26]

Tensor notation	Corresponding matrix notation
$ii = 11, 22, 33$	$m = 1, 2, 3$
$ij = 23$ or 32, 13 or 31, 12 or 21	$m = 4, 5, 6$
s_{ijkl}	s_{mn}, both m and $n = 1, 2, 3$
$2s_{ijkl}$	s_{mn}, m or $n = 4, 5, 6$
$4s_{ijkl}$	s_{mn}, both m and $n = 4, 5, 6$
d_{ijk}	d_{im}, $m = 1, 2, 3$
d_{ijk}	$\frac{1}{2}d_{im}$, $m = 4, 5, 6$
Q_{ijkl}	Q_{mn}, $m = 1, \ldots, 6$, $n = 1, 2, 3$
$2Q_{ijkl}$	Q_{mn}, $m = 1, 2, \ldots, 6$, $n = 4, 5, 6$

$$S_m = s_{mn}T_n + d_{im}E_i \tag{1.18}$$

$$D_i = d_{im}T_m + \varepsilon_{ij}E_j \tag{1.19}$$

$$T_m = c_{mn}S_n - e_{im}E_i \tag{1.20}$$

$$D_i = e_{im}S_m + \varepsilon_{ij}E_j \tag{1.21}$$

1.4 Literature Review

1.4.1 AFC and IDE Design

Active fiber composites were originally designed and created by Hagood and Bent [2] as a response to a need of improved piezoelectric structures used for vibration suppression. In one of their studies, Hagood and Bent [2] developed AFCs to replace piezoelectric wafers used in structural actuation application. Typically, monolithic piezoelectric wafers were used as actuators in structures to help control or suppress vibrations. These wafers were either bonded to the surfaces of the structures or embedded within composites. The main issue with the piezoelectric wafers is that large-scale applications are not realistically feasible. The wafers themselves could not be enlarged due to their inherently brittle nature. The wafers would crack during the fabrication process, rendering them significantly less useful. Since the wafers could not be scaled up, more had to be used. Surface mounting numerous wafers was labor intensive, and incorporating more into composite materials created too many stress concentrations, impacting the overall strength of the structures in which they were used.

The desire to monitor and potentially control structural vibration brought about the push for developing a new piezoelectric device. However, PZT, which is the material that the wafers were typically made from, was still desired in these applications because of how strongly it couples mechanical and electrical domains. Hagood and Bent [2] pioneered the drive to figuring out a way to incorporate PZT into larger scale piezoelectric sensor and actuator applications. They came up with the idea of using PZT in fiber form instead of wafer form. PZT fibers were significantly more flexible than their counterpart wafers. However, the individual fibers were extensively more brittle than the wafers, and individually, they could only support fractions of the forces the wafers could. Hagood and Bent [2] realized, though, that when used together, groups of fibers could better distribute loads as well as help support each other. Plus, the purpose of creating new devices is scalability, and adding more fibers was an extremely simple way to scale up the size of this new device.

Bent and Hagood's [2] idea for a new piezoelectric sensor and actuator involved placing numerous fibers evenly spaced next to each other along the same uni-axial direction. The fibers were then enveloped within an epoxy matrix. The matrix serves as a protective layer for the fibers against external damage while simultaneously distributing any loads applied to the composite across all of the fibers. Additionally, the epoxy provided an extra mechanical stiffness while allowing the entire assembly to flex. On each side of the fiber-epoxy composite, an electrode was put in place. The end result, shown in Figure 1.8, was the first AFC idea concept.

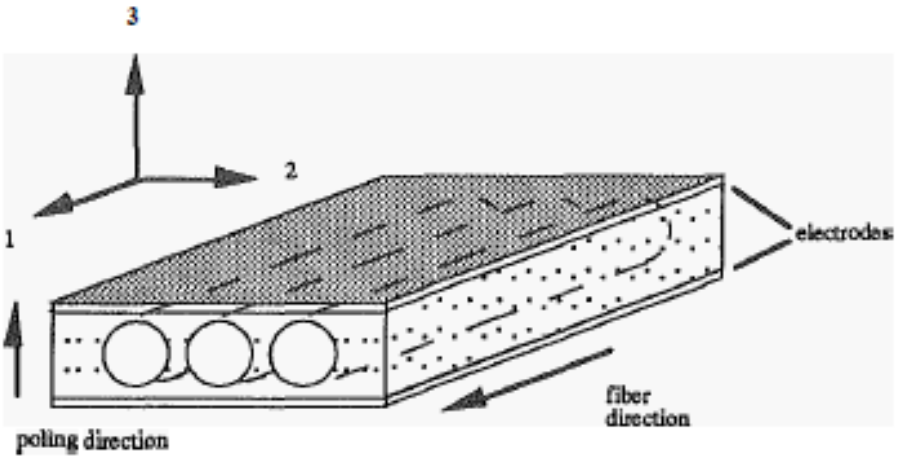

Figure 1.8: First AFC concept [2]

The electrodes used created a poling field through the thickness (diameter) of the fibers, similar to the poling field though the thickness of the PZT wafers previously used. This direction, therefore, was defined as the '3' direction of the AFC. For this study deformation along the '1' direction was studied in order to compare the d_{31} of the new composite to the wafer. According to their model, the d_{31} values should be very comparable, but the experimental value they achieved ended up being noticeably less than expected. Hagood and Bent [2] reasoned that this significant difference in values could be attributed to poor modeling as well as the epoxy used blocking the full strength of the electric field from reaching the fibers.

Around the same time, Hagood *et al*. [7] did a study on improving actuation in the piezoelectric ceramic wafers by using a specially designed electrode pattern. Typically, piezoceramic wafers were electroded in such a way that they were poled through their thickness. This type of electrode orientation is commonly referred to as a parallel electrode design. For parallel electrodes, the electric field everywhere between the electrodes is uniform in magnitude and direction. For conventional poled piezoceramic wafers, the poling direction and the direction of planar actuation are orthogonal to one another, shown in Figure 1.9. Because of this, the piezoelectric strain is a result of the transverse piezoelectric effect represented by the d_{31} coefficient. However, a material's piezoelectric properties are stronger if the directions of poling and mechanical actuation are the same rather than orthogonal to one another. If instead an IDE is used on a piezoceramic wafer, a significant portion of the electric field can be applied in the direction of planar actuation, shown in Figure 1.9, and this new poling direction is taken as the material's '3' direction. Since the poling direction is in line with planar actuation, piezoelectric strain is a result of the longitudinal piezoelectric effect represented by the d_{33} coefficient. The longitudinal effect is usually preferred over the transverse effect because it produces induced strains typically 2.4 times greater. Additionally, the longitudinal effect induces stresses up to 4 times greater ($e_{33}/e_{31}=4$) [7].

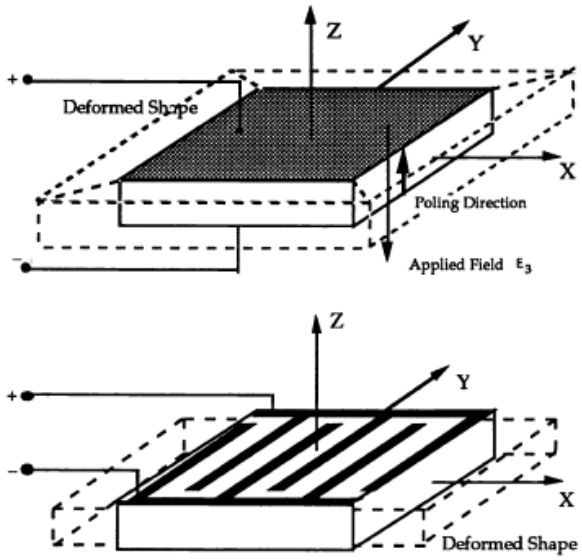

Figure 1.9: Conventional parallel electrode (Top) and interdigitated electrode (Bottom) [7]

The largest issue with using IDEs is that the electric field that they produce is not uniform like it is for parallel electrodes. This non-uniformity results in a weaker overall component of the field in the direction of actuation for a given applied voltage than would be created between parallel electrodes. However, this net directionality could be maximized by altering the geometry of the IDE design. Hagood *et al*.'s study highlights their research done toward maximizing the component of the electric field in the plane of the wafer by studying the design of the IDE used on the wafer. Specifically, the study focused on the performance capabilities of an actuator as a function of the electrode gap to sample thickness ratio. Two different models were created and analyzed. The first was a simple approximate Rayleigh-Ritz model, and the second was a piezoelectric finite element model created in ANSYS.

Through analysis of the two models, an interesting relationship between the strain response in the wafer and the electrode gap to sample thickness ratio was found. According to both models, if the electrode gap is increased and the electric field is held constant, then the strain response of the material increases, indicating that the component of the electric field in the direction of actuation increased. Figure 1.10 shows this increased strain response. The relative strain is defined as the strain capability of the IDE actuator normalized by the strain capability of a conventional piezoceramic wafer under the same applied electric field. The relative strain values are negative since the strains produced by the IDE wafer and a conventional wafer are opposite in phase. A positive field applied to a conventionally electroded wafer would induce a negative planar strain, but a positive field applied to an IDE wafer would induce a positive planar strain. It can further be seen from Figure 1.10 that Hagood *et al.* determined that the increase in strain response asymptotes to a value of 1.8 for a gap to thickness ratio of 6 to 7. This means that further increasing the electrode gap would no longer produce a significantly larger strain response. Based on the models, the study determined that through the use of an IDE, the d_{33} actuation could produce strains up to 1.8 times larger than d_{31} actuation. The deviation from the typical value of 2.4 times larger can be attributed to the non-uniform field that the IDEs create in the material. Likewise, the models were used to

study how IDEs would alter the induced stresses within the material. The results of increasing the gap to thickness ratio, shown in Figure 1.10, indicate that relative stresses up to 3.1 can be achieved. Similar to relative strain, the maximum relative stress predicted by the model is lower than the typical e_{33}/e_{31} value of 4 for a piezoceramic, which can again be attributed to the non-uniform field created by the IDEs.

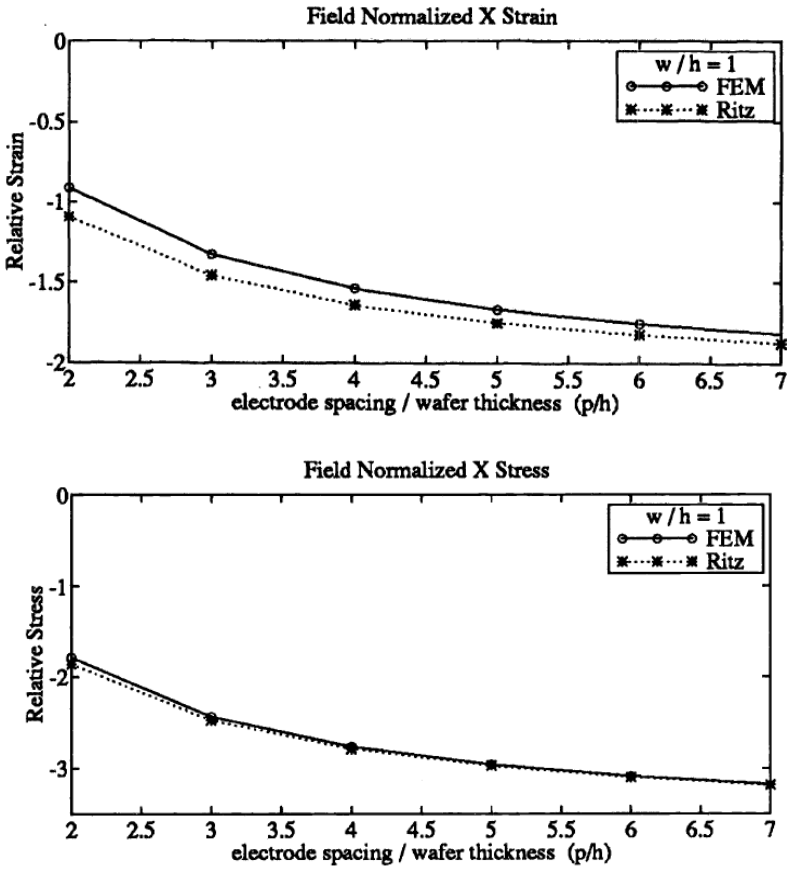

Figure 1.10: Effect of increasing electrode gap on piezoelectric response estimated using FEM and Rayleigh-Ritz model [7]

In the last part of their study, experiments were carried out to validate the results of the two models. Wafers were electroded with an IDE design and poled. The IDE design used had an electrode gap to wafer thickness ratio of 6 in order to compare to the values determined by FEM and Rayleigh-Ritz models. Through experimentation, it was found that the wafers exhibited about 1.53 times higher planar strain than conventional piezoceramic wafers. This result agrees well with the two computer models. The

experiments validated the results that the benefits of poling in the direction of planar strain with an IDE outweigh the issue of creating a non-uniform electric field in the material.

The next major step in AFC research was taken up again by Bent and Hagood [9]. Still focused on finding an alternative for monolithic piezoceramic wafers for structural sensing and actuation applications, they studied the coupling of their previously generated AFC design and the non-conventional IDE pattern. The hope was to improve the performance of the fiber composites. As previously discussed, the use of an IDE allows for the large component of the electric field to be applied in the same direction as planar actuation of the material. For AFCs, deformations of the fibers occur along their lengths. Having an electric field directed along a fiber's length would therefore be advantageous since the piezoelectric properties directed along a fiber's length, '33' properties, are stronger than those directed through a fiber's thickness, '31' properties. In their study, Bent and Hagood [9] studied two different models for their AFC: a uniform fields model and an FEM. The uniform fields model is a generalized mathematical model based on the effective properties of two-phase materials. This model was used to study different property cases to determine the resulting geometries. The finite elements model used was similar to the model used for the previously performed IDE design study. The model itself, shown in Figure 1.11, was created to represent a fiber embedded within an epoxy matrix. Due to symmetry, it was only necessary to model a one quarter section. Both models were used to study the effective d_{33} actuation of the AFC with IDEs, and they agreed with one another quite well.

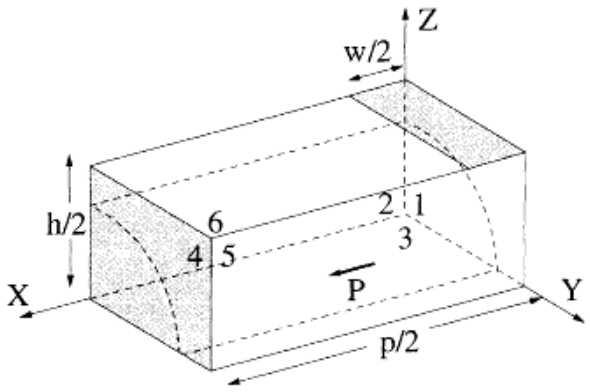

Figure 1.11: Finite elements model of a fiber in an epoxy matrix [9]

The last part of Bent and Hagood's study involved the experimental verification of the results found from the two models. This involved the fabrication and testing of AFCs between IDEs. For the AFCs, PZT fibers that were roughly 8.2 cm long with a diameter of 130 μm were embedded within a two-phase epoxy composite matrix. The matrix was composed of a low-viscosity epoxy and fine high dielectric particulates. The IDEs were etched onto a copper/Kapton thin film with guide holes for alignment. Everything was assembled on an aluminum vacuum plate and cured to create an AFC. After poling for 20 minutes, tests on the AFC were done. Figure 1.12 shows that the experimental d_{33} results did not always agree well with the values from the models. Agreement improved in AFCs with higher overall percentages of the fiber material. This means that a better understanding of the composite materials used is necessary, as well as an improvement of the model to incorporate the different characteristics of the composite materials.

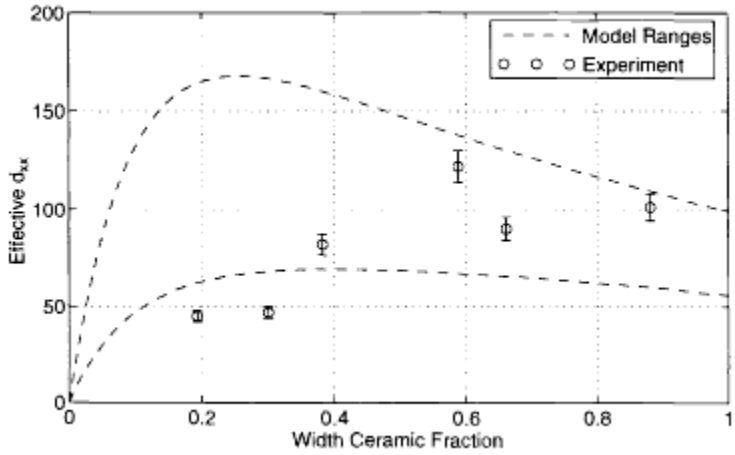

Figure 1.12: AFC experimental results in comparison with model values [9]

1.4.2 AFC Performance Improvements

The inconsistencies of AFC model results and experimental results found by Bent and Hagood [9] fueled research on improving the performance of both AFC models and fabricated devices. The goal was to increase AFC performance levels to close the gap between them and the performance levels of bulk PZT. Additionally, since the number of

applications for AFCs was so great, a standardized design and fabrication method was desired for optimized performance. In one of the earliest studies focusing on this topic, Rogers *et al*. [29] observed that varying the matrix composite material around the fibers affected the performance of the AFC. Specifically, they took a look at reinforcing an AFC in two different ways and comparing experimental results of these two new designs with a baseline AFC design. The baseline AFC was manufactured using the same method that Bend and Hagood [9] had previously created. The first alternative AFC design configuration involved incorporating high modulus S-glass filaments embedded within the matrix material surrounding the fibers. The goal of adding these glass filaments into the AFC composite material was to help improve mechanical load transfer to the fibers of an AFC in use. The second configuration involved laminating a previously manufactured and pre-poled baseline-style AFC with E-glass fabric plies, basically creating a 3-ply composite material. The goal of laminating an AFC with the glass fabric plies was to increase the mechanical stiffness of the AFC, providing an enhanced structural integrity to the system without altering the composite material of the initial system. Cross-sectional images of the two alternative AFC designs can be seen in Figure 1.13.

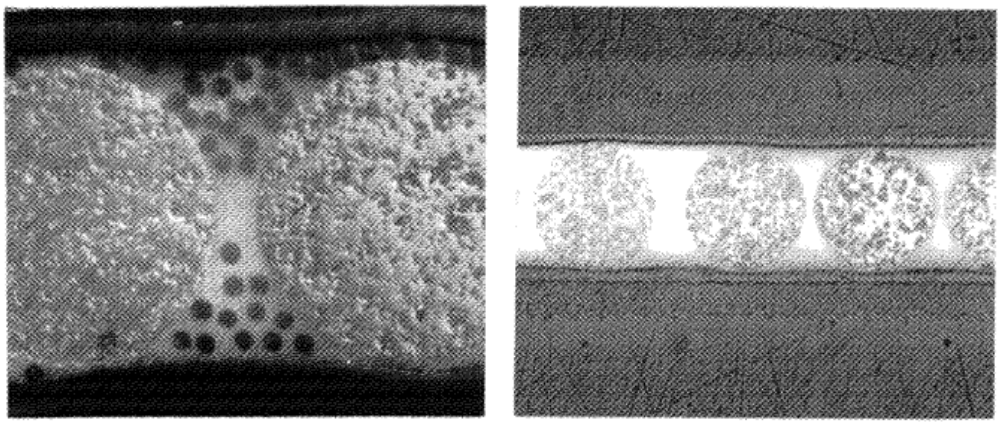

Figure 1.13: S-glass fibers embedded within the matrix (left) and glass-ply laminated AFC (right) [29]

In their study, Rodgers *et al.* [29] performed a series of passive and active property and performance tests on the three AFC designs. The passive property and performance tests studied each design's stiffness, ultimate strength, capacitance, and long

term mechanical fatigue. Results from the passive experiments showed that the values of stiffness for the two glass-reinforced AFCs were not significantly impacted in comparison to the baseline AFC, which was expected based on mathematical predictions using the combined material properties. Although the stiffness values were not significantly altered, the ultimate tensile strength values were. Using ultimate strength tensile tests, it was determined that average failure stresses and strains of the glass-reinforced AFCs were an order of magnitude higher than those of the baseline AFC. It was also found that the capacitance of the AFC of glass embedded within the matrix surrounding the fiber was greatly reduced in comparison with the baseline AFC. This was due to the difficulty of properly embedding the glass fibers. Instead of residing only between the PZT fibers, the glass fibers were many times located between the electrode and the PZT fiber. Their much lower dielectric properties blocked significant portions of the electric field from reaching the PZT fibers. A definite conclusion on how the capacitance of the laminated AFCs was altered could not be made due to the possible inconsistencies in initial IDE alignment.

The active property and performance tests [29] studied each design's induced stress and strain capabilities, long-term electrical fatigue, and actuation under load. Results of the active experiments showed that the low field strain capabilities of the glass-reinforced AFCs were significantly impacted in comparison to the baseline AFC's performance. The low-field d_{33} coefficient for the baseline design was, on average, about 116 pm/V. The low-field d_{33} coefficient of the glass-ply laminated AFC was reduced to about 50% of the baseline AFC's value, and its representative strain work cycle was reduced to about 30%. These results are primarily due to mechanical clamping effects of the E-glass plies. For the embedded glass fiber AFC design, the low-field d_{33} coefficient could not be determined. Part of the issue was due again to mechanical clamping effects, but the major problem was the electric field blockage by the glass fibers from the electrodes to the PZT fibers. Similarly to the laminated AFC, the glass-embedded AFC design had a significantly reduced representative strain work cycle.

AFCs have since been continuously studied and redesigned in order to try and optimize their piezoelectric capabilities. By 2000, the general design of the AFC had reached a semi-standardized state. Rossetti *et al.* [8] did a study on this so called "state-of-the-art" design. Having been originally designed using PZT-5H fibers, AFC design had made a move toward using PZT-5A fibers instead because they exhibited much lower coercive fields, making them much easier to pole. The '-5H' and '-5A' terms refer to different doping of a base PZT material to achieve different properties, which is discussed in Section 2.1. Furthermore, the typical fiber diameter and AFC dimensions had become "standardized." The typical materials and design dimensions used can be found in Table 1.2.

Table 1.2: Materials and Dimensions of a typical AFC [8]

IDE ELECTRODE, MATRIX, AND FIBERS	**COMPONENT MATERIALS**
Substrate Material	Kapton®
Conductive Ink	Silver-Loaded Epoxy
Polymer Matrix	Epoxy Film Adhesive
Fiber Type	PZT-5A
AFC GEOMETRY	**DIMENSIONS**
Overall Thickness	330 μm
Length X Width	13.5cm X 5.5cm
Fiber Diameter	250 μm
Fiber Line Fraction	85% - 90%
Fiber Volume Fraction	50% - 55%

Rossetti *et al.* [8] also reviewed the study of varying electrode pitch and fiber diameter simultaneously. As discussed previously, varying the spacing between the electrodes as well as the thickness of the fibers alters the p/h ratio of the AFC. The proper p/h ratio of an AFC design depends on the application of the AFC. Designs with a smaller ratio allow actuation at lower fields, but are much less efficient due to the

significantly lessened portion of the electric field in the direction of actuation. Alternatively, designs with larger ratios require much higher voltages for actuation. Changing either the electrode spacing or the fiber thickness would have a significant impact on the behavior of the AFC. Table 1.3 provides the resulting peak strain values achieved for various p/h ratios.

Table 1.3: Peak actuation strains for varying p/h ratios [8]

p/h Ratio	p : h (µm : µm)	Voltage (V)	Strain (ppm)
2.7	635 : 239	± 850	960
4.6	635 : 137	± 850	1131
8.3	1143 : 137	± 1500	1350
16.7	2286 : 137	± 3000	1580

Even though AFC fabrication was becoming more and more standardized, accurate predictions of the AFC's electromechanical behavior were still lacking. Originally, analytical and numerical models were used to try and predict the behavioral performances of AFC. However, the geometry of an AFC is complex and cannot be accurately accounted for in the mathematical models. So, the next step was to turn to finite element (FE) modeling. Using FE modeling, the variations in the electric field throughout the fiber could be better captured and quantified.

In an attempt to predict AFC performance better than before, Belloli *et al.* [30] tried to enhance the FE models being used by adding a new concept and design into the model. Originally, fiber-to-electrode contact was modeled as a tangential contact. The area beneath this contact is known as the "dead zone" because actuation of the fiber here is supposedly negligible. However, Belloli *et al.* found that instead of a tangential point contact, there was usually a larger region of contact between the electrode and the fiber. They defined the portion of the circular cross-section of the fiber that was in contact with the electrode as the contact angle and implemented it into their FE model. A schematic

view of a representative volume element (RVE) of the AFC FE model used in their study is shown in Figure 1.14.

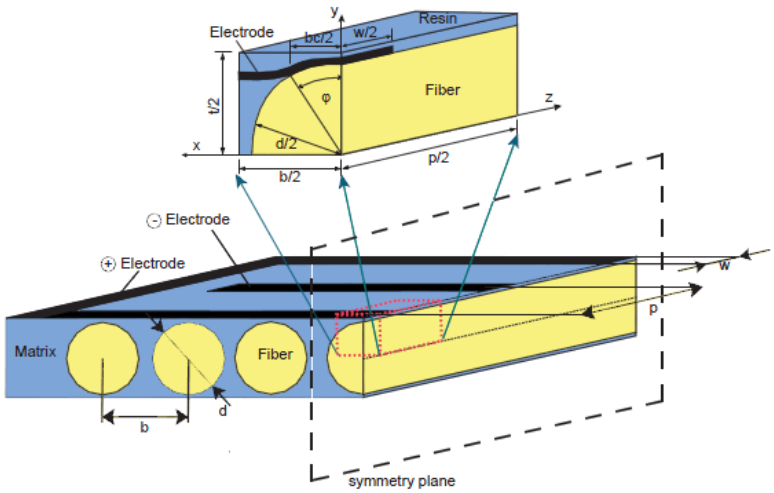

Figure 1.14: Representative volume element of an AFC incorporating a contact angle [30]

In their study, the FE model of the RVE was used to study the effects of the contact angle in an AFC. It was believed that varying the contact angle would have a significant impact on the electromechanical behavior of an AFC. As mentioned previously, there is a "dead zone" under the electrode where the electric fields produced are significantly weaker than those produced in the gaps, and these fields are more perpendicular rather than parallel to the actuation direction. However, the presence of a contact angle in this zone creates a better distribution of the electric field due to a lack of an epoxy matrix to distort the field. Using the model, it was seen that an increased contact angle enhanced the piezoelectric constant of the AFC. Belloli *et al.* then performed experiments where the contact angle was increased and found results that compared well with the numerical predictions. The experimental results of varying the contact angle on the effect piezoelectric coefficient can be seen in Figure 1.15.

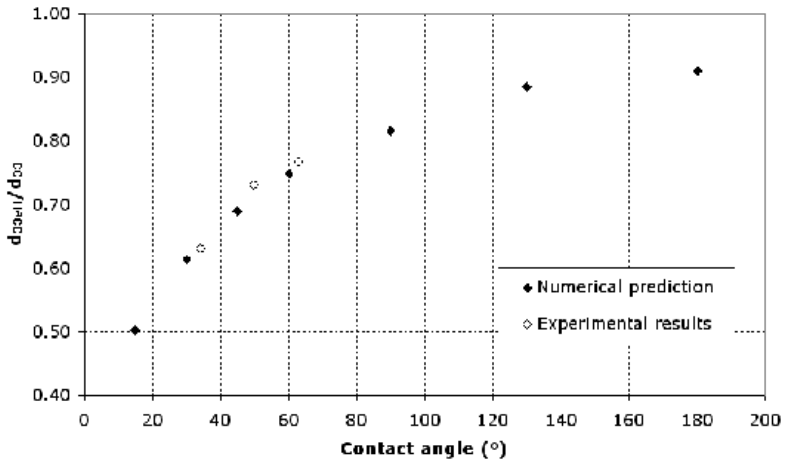

Figure 1.15: Effective piezoelectric constants with respect to contact angle variations [30]

1.4.3 PZT Fiber Electromechanical Characterization

Active fiber composites have been a focus of the smart materials community for many years; however, a gap between the theoretical piezoelectric behaviors and the actual experimental behaviors of AFCs still exists. Extensive research has been done in designing and redesigning new AFCs to optimize their electromechanical outputs. Additionally, numerous numerical and computational models have been created to better predict the behavior of specifically designed AFCs. These models, however, share a similar issue. The properties of the fibers used in the models are taken from the properties of bulk PZT. This is because the mechanical and electrical properties of bulk PZT have been extensively studied and well documented. Conversely, research data for the properties of individual PZT fibers is drastically less available. The small diameters and commonly used techniques for characterization make experimentation extremely difficult or even impossible; thus, very little fiber property data is available. Among the data that is available for individual fibers, a large portion is from research studies done to determine mechanical properties. Through these studies, it was found that the PZT fiber did in fact have different mechanical properties than bulk PZT, which meant that the electromechanical properties would more than likely also be different [11, 12, 13].

Studies have been done to determine the electromechanical properties of individual PZT fibers. In one study by Nelson *et al.* [14], experimentation was done in order to determine the d_{33} coefficient of individual PZT fibers. These experiments were motivated by the fact that previous research into the electromechanical properties of PZT fibers had only focused on fibers in a 1-3 style composite. Fibers were cut and placed into a mould while a low viscous epoxy was poured into the mould under vacuum. Once cured, the composite was painted with a silver paint on its flat faces and the fiber composite was poled along the length of the fibers. Through testing, a d_{33} coefficient for PZT fibers was determined to be 270 pm/V, which is expectantly less than the bulk PZT value of 374 pm/V.

Although this study was able to determine a piezoelectric d_{33} coefficient, there are a few issues with the experiments that were carried out. First, the assembly, which can be seen in Figure 1.16, was created and tested using a parallel electrode style configuration. When piezoceramic fibers are used in AFCs, IDEs are used to take advantage of the '33' direction of the fibers, but the IDEs create a non-uniform electric field as discussed earlier. Therefore, the results of this study do not provide a direct characterization of how fibers would behave electromechanically in an AFC. Second, the fibers were embedded within an epoxy matrix. This means that the fibers were continuously being influenced by the epoxy, causing all results found to be behavioral results of the fiber-epoxy combination rather than just the fibers themselves. Lastly, the electromechanical d_{33} behavior of a PZT fiber found was an interpolated value extracted from data gathered via testing the composite material, making the reported coefficient not a true direct characterization of an individual PZT fiber. Most of the research studies done to characterize individual fibers exhibit similar issues during experimentation: the fibers are not tested individually.

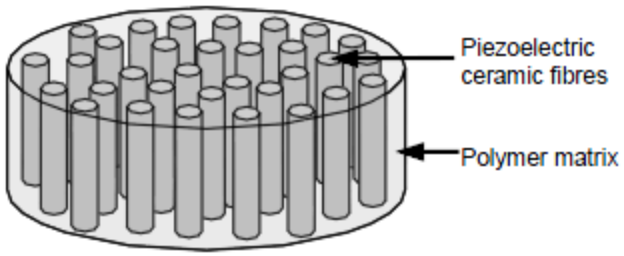

Figure 1.16: Parallel electroded composite created to determine the d_{33} coefficient of PZT fibers [14]

There are a few exceptions, however, where studies have been performed on individual PZT fibers. In one study by Heiber *et al*. [15], individual fibers were tested in order to determine their ferroelectric properties in correlation with microstructure features. In this study, PZT fibers were cut to 3.5 mm lengths and placed vertically into a PMMA disk. Both ends of the fiber were coated with a silver paint to act as the electrodes. During testing, electric fields ranging from -30kV/cm to 30kV/cm were applied to the fiber and ferroelectric hysteresis loops were measured and recorded. Through this study, the polarization and free strains were found as functions of the applied electric field to the fiber. Additionally, the effects of microstructure on strain and polarization were tested as well. It was found that differences in microstructure showed significant impact on the free strain of a fiber as well as its possible remnant polarization. Specifically, increased porosity in a fiber causes reduced saturation and remnant polarization magnitudes in a fiber. Furthermore, increased grain sizes allow for lower coercive fields in a fiber, making them easier to pole. Although this experiment studies individual PZT fibers, direct measurements of the piezoelectric stress and strain behaviors of the fibers were not studied. Furthermore, the data gathered is representative of fiber between parallel electrodes rather than fibers in an IDE assembly as in a typical AFC.

In another study, hollow fibers were tested electromechanically in order to characterize their piezoelectric behaviors. This study by Guillot *et al*. [12] was motivated by the desire to integrate PZT fibers into woven fabrics in order to create energy harvesting fabrics. However, a typical PZT fiber could not be added to the fabric without adding the IDE assembly with it, making implementation of typical solid fibers

impossible. Instead, they examined the electromechanical behaviors of hollow PZT fibers. Hollow fibers were studied because an electrode could be placed on both the inner and outer diameters of the fiber. The hope was that this style of electroding would maximize the capacitance of the fibers since the electrodes would be in direct contact with the fiber, and that this amplified capacitance would overcome the drawback of relying on the less effective d_{31} coefficient. For their study, small diameter hollow PZT fibers were electroded by dipping the fibers into a solution of nickel chloride and sodium hypophosphite. After a 90 minute immersion time, the fibers were removed, and an electrode layer roughly 25 μm thick was left on the outer and inner diameters of the hollow fiber. Then, some of the fibers were encased in a heat shrink polymer tube for protection, and the fibers were poled. A concept of the electroded and poled fibers can be seen in Figure 1.17.

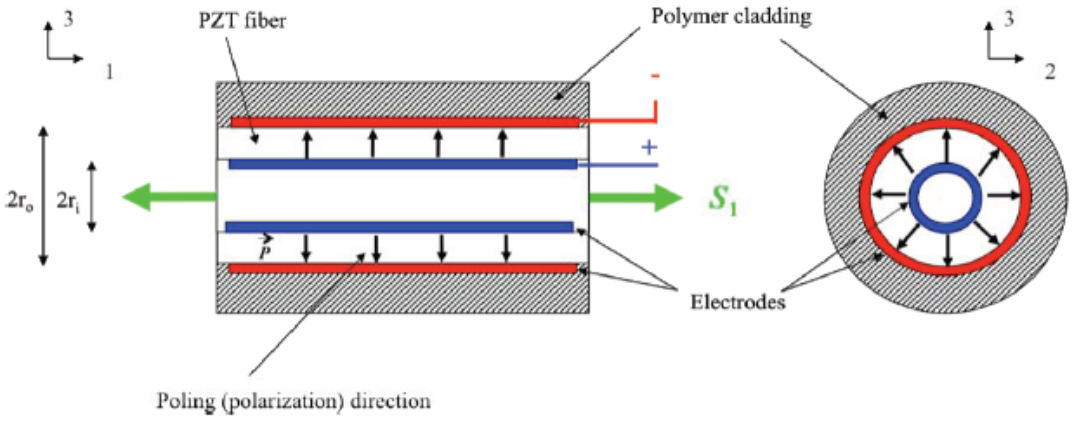

Figure 1.17: Radially poled hollow PZT fiber [12]

For electromechanical testing, capacitance of the poled fibers was found using an impedance analyzer over a 100Hz to 5kHz frequency range. Then, the d_{31} coefficients were determined using a laser Doppler vibrometer using the converse piezoelectric effect. Results showed an average d_{31} value of -105 pm/V for individual hollow PZT fibers, which was about 55% of the bulk PZT value. Although this study does in fact experimentally test for the electromechanical responses of individual PZT fibers, there are a few issues when considering AFCs. First and foremost, the hollow fibers used in this study do not provide a good representation of the solid fibers used in typical AFCs.

Second, the electrode configuration takes advantage of the d_{31} piezoelectric behavior of the fiber, not the d_{33} as AFCs typically do. Furthermore, the electrode configuration represents a parallel electrode rather than an IDE. Lastly, some of the fibers tested in this study were encased in a polymer cladding, which could have affected the true electromechanical behaviors of individual fibers.

Very recently, a study on characterizing mechanical, dielectric, and piezoelectric properties of individual PZT fibers was done by Wyckoff [16]. His study, to the best of our knowledge, provides the first look into accurately characterizing the electromechanical properties of individual fibers. In this study, PZT-5A fibers with 250 μm diameters were tested using both a parallel electrode configuration and an IDE configuration. Electromechanical tests to determine the induced stress coefficient were performed using a function generator-voltage amplifier combination to deliver the voltages to the electrodes and a dynamic mechanical analyzer (DMA) to measure the stresses induced in the fibers during testing. For the parallel electrode setup, two brass spherical electrodes were secured into the tensile grips of the DMA. Then, Wyckoff cut PZT fibers into small 2mm lengths and installed the fibers between the brass spheres using very small indents on the tips of the spheres to align the fiber vertically. The fibers were poled under a 2 MV/m electric field and then tested under various alternating current (AC) electric fields ranging from 0.1-1 MV/m at a frequency of 100 mHz. For the IDE setup, Wyckoff created a special IDE assembly using screen-printed electrodes adhered to acrylic plates. This assembly allowed a fiber to be inserted and held between two IDEs without the use of an epoxy matrix. Fibers were cut to 70 mm lengths, and an individual fiber was installed between the IDEs so that portions of the fiber stuck out on both ends of the assembly. Then, the assembly was installed into the DMA by clamping the ends of the fiber in the tensile grips. The fiber was again poled in a 2 MV/m field and tested under the same range of AC fields at 100 mHz.

For both styles of testing, a non-linear behavior was observed in the fibers, as expected. So, a modified Rayleigh law was applied to the data in order to determine the piezoelectric coefficients of the fibers. For the parallel electrode setup, a plot of the

induced strain coefficient (e_{33}) as a function of applied electric field can be seen in Figure 1.18. The piezoelectric e_{33} coefficient was determined to be about 2.8 C/m^2, which was about 20% of the reported bulk PZT value of 15.8 C/m^2. This result drastically deviated from the common assumption that PZT fiber properties are roughly 65-75% of the bulk PZT property values [12]. Similarly, a plot of the IDE e_{33} coefficients can be found in Figure 1.18. The reported IDE e_{33} value was 1.5 C/m^2. The IDE coefficient was, as expected, below the parallel electrode value due to the non-uniform field in the fiber produced by IDEs.

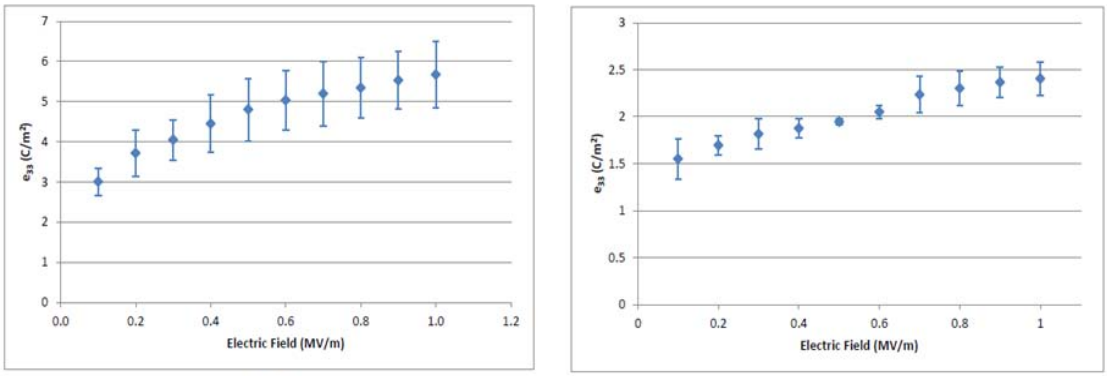

Figure 1.18: Individual fiber piezoelectric e_{33} coefficients found between parallel electrodes (a) and IDEs (b) [16]

Due to a lack of literature with which to compare the e_{33} coefficient results, two simple FEA models were produced in order to verify the results. Using fiber property data gathered from his study as well as a few assumed properties of 70% of the bulk PZT values, a model of a fiber between parallel electrodes predicted an e_{33} value of about 6 C/m^2 which also showed significant deviation from the assumed 65-75% rule of thumb. Similarly, a model of a fiber between IDEs predicted an e_{33} value of about 4 C/m^2. Even though the FEA models displayed deviation from the 65-75% property assumption, differences in experimental and model values still existed due to a few potential issues with the experimental processes.

Additionally, Wyckoff [16] performed parallel electrode d_{33} tests on the fibers using a linear variable differential transformer (LVDT) on a lock-in amplifier. Fibers

were tested through a range of electric fields from 0.1-1 MV/m at frequencies of 0.2, 1, and 5 Hz. The induced strains in the fibers were measured and recorded by the LVDT, and the d_{33} coefficient data as a function of electric field was plotted. The d_{33} coefficient values were found to be 516 pm/V, 477 pm/V and 432 pm/V. All three of these values were above the bulk PZT value of 374 pm/V, which was unexpected. Wyckoff explains that the discrepancy can likely be attributed to the fact that strain values collected were not true representations of free-strain. Similarly to previous research, the drawback of Wyckoff's experiments done for d_{33} testing of individual fibers is that tests were done under a parallel electrode configuration. The results, therefore, cannot be directly compared to true fiber behavior in a typical AFC.

1.5 Scope of Thesis

1.5.1 Goals and Tasks

The goal of this thesis is a better understanding of the fiber's piezoelectric properties to improve the design and manufacture of AFCs for many applications. Not only can more accurate models of AFCs be created, but superior engineered materials for the electrodes and the epoxy matrix can be chosen to complement the fiber's true electromechanical properties. The objective is to experimentally determine the piezoelectric e_{33} and d_{33} properties of individual PZT fibers for use in active fiber composites. This objective is achieved by improving upon the e_{33} experiments previously performed on the fibers to obtain better coefficient values as well as developing and implementing a new d_{33} experiment for the fibers. Systematic testing and improvements in testing are conducted on the fibers using an assembly created to mimic fiber use in an AFC. The specific tasks related to this work are:

Task 1. Experimental characterization of the parallel electrode fiber e_{33} value

Task 2. Experimental characterization of the IDE fiber e_{33} value

Task 3. Experimental characterization of IDE fiber d_{33} value

Task 4. Verification of IDE d_{33} results using FEA

1.5.2 Organization of Thesis

Chapter 1 provides background information on piezoelectricity as well as a summary of research studies done on designing and characterizing AFCs and determining PZT fiber electromechanical characteristics. Specifically, Chapter 1 highlights the overall small amount of research done on individual fiber piezoelectric characterization, which gives motivation towards completing the goals of this thesis. Chapter 2 provides the general materials and procedures used in order to experimentally determine the desired piezoelectric coefficients of the PZT fibers. The first coefficient tested is the induced stress coefficient (e_{33}). Experimental strategies are systematically implemented to improve the experimentally determined coefficient values for both parallel electrodes and IDEs and bring them closer to values generated via FEA modeling.

The second coefficient focused on is the induced strain coefficient (d_{33}) of the material. Experimental characterization is conducted for the IDE setup only due to the limitations of the testing equipment. Additionally, IDE fiber coefficients are mainly focused on since they directly relate to fibers used in AFCs. Chapter 3 of this thesis provides detailed results on the parallel electrode and IDE e_{33} experiments. Brief discussions of each improvement's impact on the coefficients determined in relation to FEA models previously generated are also provided. Chapter 3 also provides the results of the IDE fiber induced strain coefficient experiments as well as a brief discussion of the results in relation to bulk PZT. Additionally, using a relationship between the piezoelectric d_{33} and g_{33} coefficients, the experimentally obtained d_{33} value will be used to find the g_{33} value of PZT fibers. Since values of the IDE d_{33} values of PZT fibers has not been published previously, verification of the experimentally obtained values through FEA modeling is necessary. Chapter 4 outlines the development of an FEA model of a fiber in an IDE setup as well as the conditions used to mimic IDE use. This model is used in an effort to validate the experimental results of the induced strain coefficients obtained in Chapter 3. Chapter 5 summarizes the findings of this thesis as well as the conclusions drawn from the data collected. Additionally, recommendations for future work are given.

Chapter 2
Experimental Characterization of the Piezoelectric Coefficients of PZT Fibers

2.1 Introduction and Fiber Materials

In this chapter, the different methods and equipment used to characterize the piezoelectric coefficients of the PZT fibers, specifically the piezoelectric d_{33} and e_{33} coefficients, are detailed. The experimental techniques used are based on methods for coefficient determination of the fibers previously designed and implemented in our Electroactive Materials Characterization Lab (EMCLab) by Wyckoff [16]. All experimental methods and procedures were carried out on PZT 5A fibers.

PZT 5A is a specific composition of PZT that has been doped in order to achieve specific properties. As explained by Damjanovic [26], doping allows for the ability to create a wide range of materials with a wide range of functions; but mostly, doped forms of PZT usually fall into two different categories: (1) “soft” and (2) “hard”. Soft PZT is created using a donor dopant mechanism. In the chemical structure, donor dopants like La^{+3} are used in place of Pb, or possibly dopants like Nb^{+5} are used in place of (Zr,Ti). As a result, soft PZT materials exhibit low conductivity and high dielectric loss, they have low coercive fields, they are easy to pole and depole, and they have high piezoelectric coefficients. Hard PZT is created via an acceptor doping process. In an acceptor doping mechanism, Pb is replaced with cations like K^{+}, or (Zr,Ti) is replaced with acceptors like Fe^{+3}. As a result, hard PZT materials exhibit higher conductivity and much lower dielectric losses, they have higher coercive fields, and they are harder to pole and depole. PZT 5A is a “soft” PZT material and is the material of choice for all of the experiments done here because of the commercial availability of PZT 5A fibers, its ease of poling at low coercive fields, and its significantly better inherent piezoelectric properties.

PZT 5A in bulk material form has been extensively investigated, and in particular, the piezoelectric strain (d_{33}) coefficient, the piezoelectric stress (e_{33}) coefficient, and the coercive field values for the bulk material have been well documented and are readily available. Table 2.1 provides the electromechanical properties of interest for bulk PZT 5A from Berlincourt and Krueger [31].

Table 2.1: Electromechanical properties of interest for bulk PZT 5A [31]

Properties of Bulk PZT 5A	
Relative Permittivity (ε_r)	1700
Coercive Field (E_c) [MV/m]	1.2
Induced Stress (e_{33}) [C/m^2]	15.8
Induced Strain (d_{31}) [pm/V]	-171
Induced Strain (d_{33}) [pm/V]	374

These property values, however, are not the same for PZT 5A when the material is in fiber form. According to Guillot *et al*. [12], manufacturers of PZT 5A fibers estimate that the electromechanical properties of the fibers are about 65-75% of the bulk material values. This difference in property values can be attributed to the manufacturing process of the fibers. Specifically, the differences arise from density changes resulting from changing porosities in the material. When bulk PZT undergoes its sintering process, low porosities in the resulting material are desired. Low porosities (less than 5%) produce better electromechanical responses in the material [16, 32]. Any pores that are created during the PZT fabrication process can be attributed to the evaporation of the organic compounds found in the pre-sintered PZT powder. PZT fibers, however, tend to experience larger porosities than bulk PZT materials.

In a study done by Kornmann and Huber [11], PZT fibers that were manufactured using three different methods were studied: one was an extrusion process and the other two were spinning methods. These additional manufacturing processes tend to increase

the levels of porosity in the resulting sintered material. During their study, they found that some of the fibers had shown significant porosity, reaching levels of up to 20% porosity. From an electromechanical standpoint, this high porosity within the material has significant impact on the properties of the fibers. Having less material per given volume (lower density) means that there is less material to respond mechanically to electric fields, or there is less material to produce charge when mechanically stimulated. This is why PZT fibers are estimated to have electromechanical properties of only about 65-75% of the bulk material values. For this study, all of the electromechanical properties of interest being tested are compared to the estimated theoretical values of PZT 5A fiber properties.

The fibers being used for this study were supplied by Advanced Cerametrics Inc. located in Lambertville, NJ[1]. These fibers were manufactured using an extrusion and sintering process. Each fiber is roughly 250 μm in diameter and has an initial length of about 200 mm. An image of the fibers supplied for testing can be found in Figure 2.1.

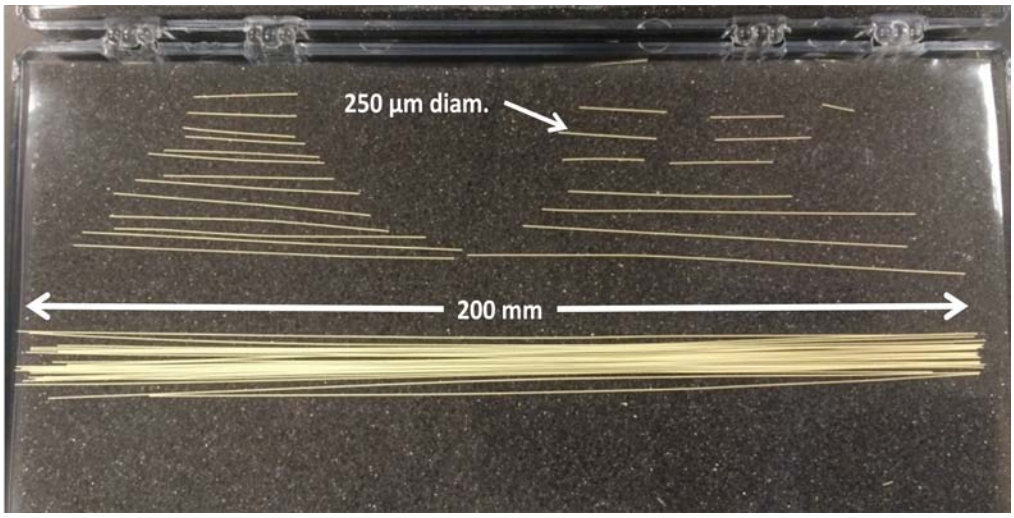

Figure 2.1: PZT fibers supplied by Advanced Cerametrics Inc.

[1] Advanced Cerametrics Inc. no longer exists

2.2 Experimental Equipment

2.2.1 Fiber Poling Equipment

Poling is the process in which a large electric field is passed through a ferroelectric material, re-orienting the dipoles in the material to align with the field direction. If a large enough electric field is applied (above the material's coercive field), then a resulting spontaneous remnant polarization remains when the electric field is removed. For all poling procedures, a function generator-voltage amplifier combination was used. An HP 33120A function generator is connected via a coaxial connection to a Trek model 6069D-6 voltage amplifier. The function generator is set to DC output and sends an output voltage signal to the voltage amplifier. The amplifier is set up to multiply the incoming signal by 1000 and output the resulting voltage.

2.2.2 Electromechanical Testing Equipment

The main goal in this study is to characterize the electromechanical properties of individual PZT 5A fibers. The first piece of equipment used to do this was a Dynamic Mechanical Analysis (DMA) RSA-G2 machine manufactured by TA Instruments. Different testing grips can be installed into the DMA for tensile tests, compression tests, and three point bending tests of a material. Figure 2.2 shows the DMA as well as the different grips than can be used. During testing, the DMA used in conjunction with a TA Instruments developed software called TRIOS [33] is utilized to apply or record stresses and/or strains in a material. The TRIOS software is used to customize the desired testing parameters. For example, boundary conditions like constant stress or constant strain conditions can be set as well as any pre-conditions necessary before tests commenced like pre-loading forces. Additionally mechanical loading effects such as sinusoidal strains and varying strain rates can be specifically programmed into an experiment. During testing for this thesis, the DMA and software were used to record the forces in the fibers.

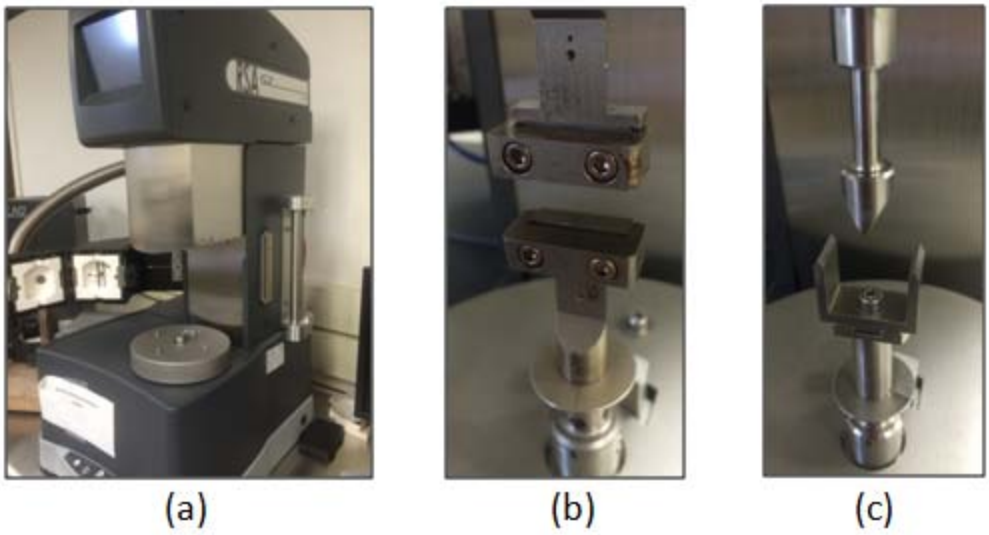

Figure 2.2: TA Instruments DMA used for e_{33} testing (a), tensile/compression grips (b), 3-point bending grips (c)

In order to characterize the piezoelectric properties of the PZT fibers, both force and voltage data needed to be captured simultaneously. The DMA-TRIOS software combination, however, was only capable of measuring and recording mechanical quantities. Therefore, the experimental setup was modified to include a National Instruments Data Acquisition System (DAQ) used in conjunction with the LabView software [34]. The DAQ-LabView combination provided the ability to record force and voltage data simultaneously. The DAQ was connected to the DMA and the HP function generator. Forces output by the DMA and voltage signals output by the HP function generator were read by the DAQ and recorded in the LabView program. Although simultaneous force-voltage data was obtained, the force data recorded in LabView was recorded as a potential difference value in the DAQ and was therefore in units of volts. Therefore, the force data in the TRIOS software was then used to convert the forces in Volts to forces in Newtons. Figure 2.3 provides a simplified schematic of the setup used for electromechanical testing of the fibers.

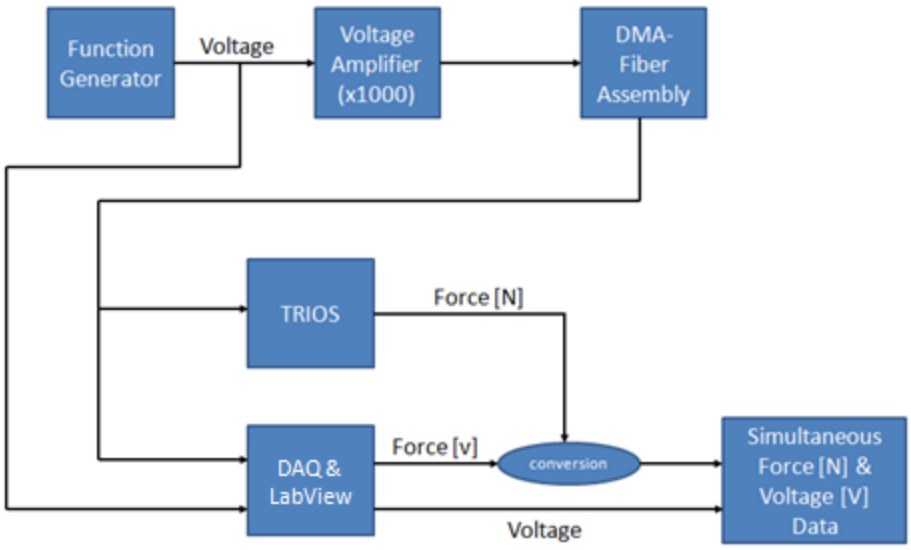

Figure 2.3: Electromechanical testing equipment setup

The final piece of equipment used for electromechanical testing was an MTI-Instruments 2100 Fotonic Sensor fiber optic probe sensor. This piece of equipment was used specifically to measure the mechanical deformation or displacement (later converted to strain) of a fiber as various electric fields were applied to the fiber. This sensor operates via the emission and receiving of light. Fibers capable of transmitting and receiving light are grouped together in a fotonic probe. To measure deformations of a sample, the probe tip is aligned perpendicular to the surface of deformation on the sample. With the probe tip aligned, light from a tungsten halogen lamp is passed through the transmitting fibers and emitted out of the probe tip toward the sample's surface. Light is then reflected off of the sample surface and captured by the receiving fibers. The captured light is then transmitted back to the MTI sensor, and its intensity is monitored. The amount of light absorbed and monitored by the sensor is linearly proportional to the distance of deformation of the sample. For this thesis study, a high resolution probe and high resolution setting were used on the sensor for testing since deformations of the fiber were on the micron scale of motion. This setup allowed for deformation changes to be resolved to 0.01 μin. Additionally, since the PZT fiber was not reflective in nature, a small piece of reflective tape was placed on the tip of the fiber to increase the amount of light reflected from the fiber-optic probe for sensing purposes.

2.2.3 Parallel Electrode Setup

Due to the difficulty of manipulating and testing individual PZT fibers, there is no commercially-available experimental setup that can test the fibers between parallel electrodes. As previously mentioned in Section 1.4.3, the study conducted by Wyckoff [16] required testing of PZT fibers between parallel electrodes. So, an experimental setup in which individual PZT fibers could be tested using a parallel electrode setup was designed and fabricated. This setup, shown in Figure 2.4, consisted of two spherical brass electrodes that acted as the parallel electrodes. Since a fiber was to be held between the brass spheres, small indentations were drilled into the spheres, which would not only help with fiber alignment but would help with holding the fiber in place during testing as well. These brass spheres were screwed onto 3D printed plastic mounts with a ring terminal sandwiched between the spheres and plastic mounts. The ring terminal supplied the voltage connection to one sphere and the grounding connection to the other. The electrode – plastic mechanisms were clamped into the tensile grip attachments for the DMA. The 3D printed mounts acted as electric insulators, isolating the voltage circuit from the rest of the DMA. For this thesis study, the same parallel electrode setup created by Wyckoff [16] is used for fiber testing.

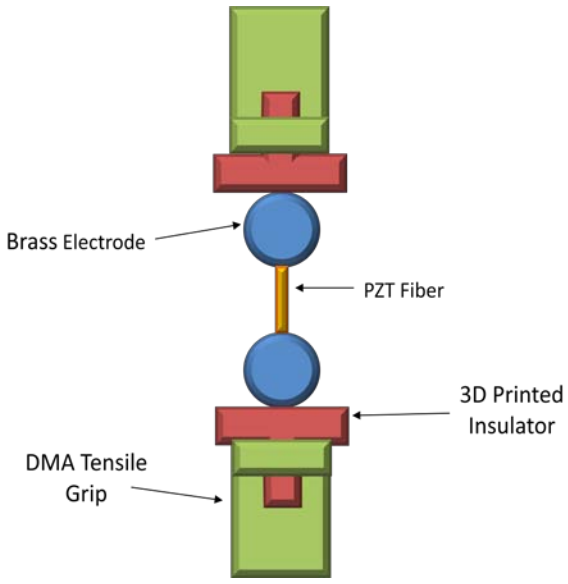

Figure 2.4: Parallel electrode setup concept

2.2.4 IDE setup

Additionally in Wyckoff's [16] study, a custom-made IDE assembly was designed that would allow for individual fiber testing in order to mimic the fiber's response in an AFC, but without the presence of an epoxy matrix. This IDE assembly used screen printed mirrored electrodes made from a silver-polycarbonate bus ink. These electrodes were printed onto Mylar sheets using a screen printing machine and screens specially ordered from UTZ Technologies. Details of the screen printing process can be found in Appendix A. The electrodes are cut and adhered to laser cut acrylic plates very carefully to ensure that the mirror electrodes are completely and properly aligned. Then, fine gauge copper wires acting as voltage and ground connections are attached to the square terminals of the electrodes using Kapton tape. Lastly, the two halves of the IDE assembly are aligned and loosely fastened together using plastic metric screws and nuts of size M2. A concept image of an IDE assembly can be seen in Figure 2.5.

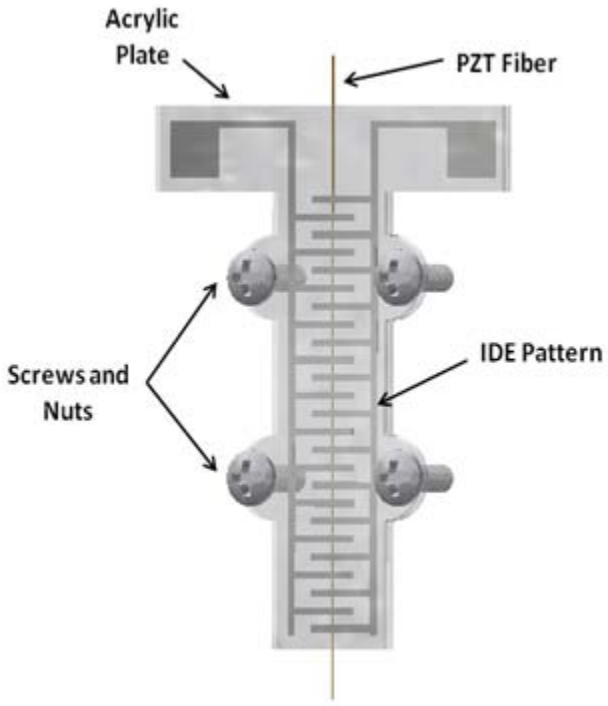

Figure 2.5: IDE assembly setup concept

As previously mentioned, this assembly was designed to test individual fibers; so, the IDE design by Wyckoff was a scaled down version of the typical IDE design used for AFCs [16]. Typical IDEs for commercially available AFCs are 140 mm long and 15 mm wide. Wyckoff's version was reduced to a size of 36 mm long and 7.5 mm wide. In addition to the size reduction, the gap distance between the electrode fingers was altered from the typical size of 500 µm. To help reduce arching between the electrodes, since an epoxy matrix would no longer be present, the electrode gaps were increased to 750 µm. The electrodes themselves were kept at a 500 µm width. This design, in comparison to the typical AFC IDE design, can be seen in Figure 2.6.

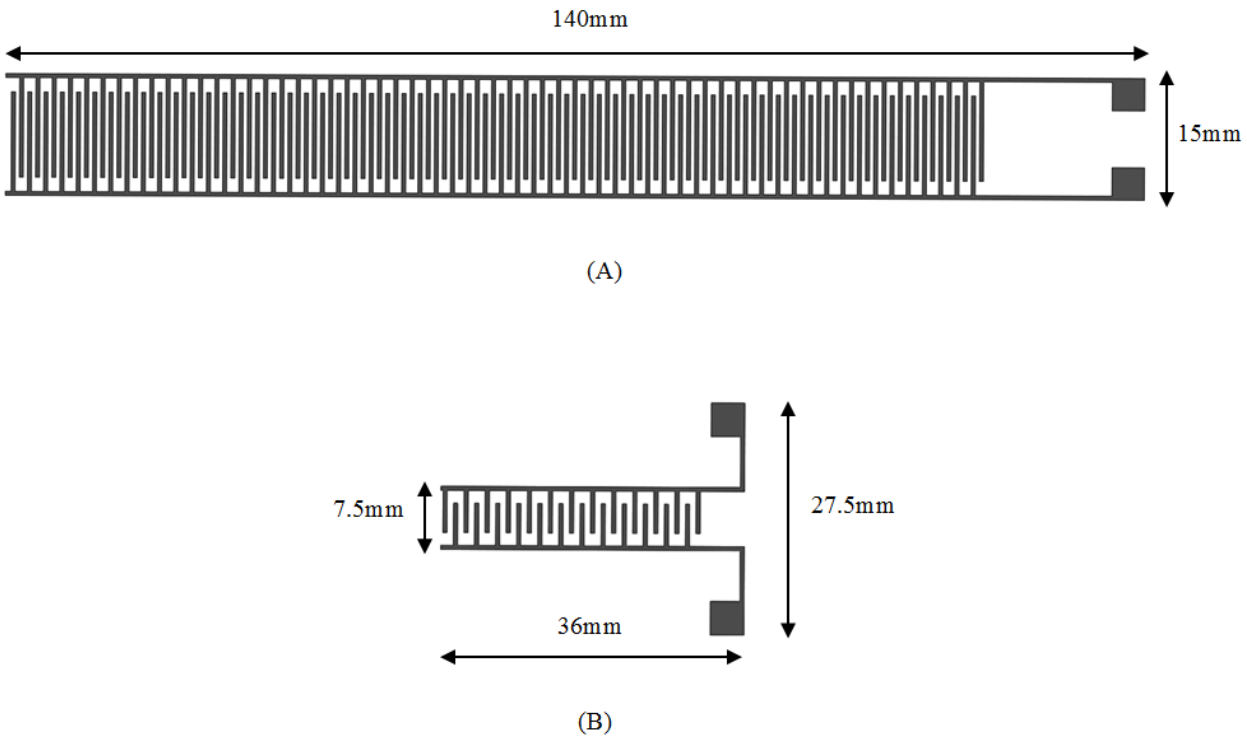

Figure 2.6: Wyckoff IDE design (bottom) compared to AFC IDE design (top) [16]

2.3 General Poling Procedure

Poling the PZT fiber to align the dipoles requires applying a large DC electric field. The electric field applied to the material during poling has to be above the coercive

field of the material, as previously discussed in Section 1.2. From previous work done [16], the coercive field for the PZT 5A fibers was determined to be 1.5MV/m. Therefore, for all fiber poling, an electric field of 2MV/m is used to ensure proper dipole reorientation in the material. For the PZT fibers, the poling process was challenging because the fibers are extremely brittle in nature. Fibers were poled directly in the characterization setup to eliminate the need to manipulate them further which could cause breaking and failure.

For both the parallel electrode and IDE configurations, the same poling process is utilized. To begin, the function generator is connected to the high voltage amplifier to control its voltage output. When powered on, the function generator is put into DC voltage mode and is set to zero volt to start. Then, the high voltage amplifier's lead and ground connections are attached to the fiber electrodes (brass spheres for the parallel setup and the IDE wires for the IDE setup). Once all connections are made, the high voltage amplifier is turned on, and the voltage on the function generator is ramped up in 0.1 kV increments to a voltage equivalent to a 2 MV/m electric field. The voltage incremental increases were spanned roughly three seconds apart to allow time for the DMA to expand the testing gap and equalize the stress set for poling. The final voltage corresponding to 2MV/m is always the same for the IDE setup since the electrode gap is always 750 μm, but it changes for the parallel electrodes setup based on the actual length of the fiber (the length of the testing gap). Samples are poled at 2 MV/m for 15 minutes to allow for sufficient time for the dipoles within the PZT fibers to reorient themselves and align with the applied electric field. Finally, the electric field is removed using the same voltage increments spaced roughly three seconds apart, and the fiber is ready for electromechanical testing.

2.4 Electromechanical e_{33} Testing

2.4.1 Parallel Electrode e_{33} Testing Procedures

The induced stress (e_{33}) coefficient is defined in the stress-charge form of the piezoelectric constitutive equations, found in Equations (2.1) and (2.2) [35]. A complete

description on what each variable means as well as what each numbered subscript means can be found in Section 1.3. The reason why this form of the piezoelectric constitutive equations was chosen is because the e_{33} coefficient through actuation is more straightforward to obtain through FEA modeling [16] using the condition outlined in Section 3.1.1 and shown in Equation (3.1).

$$T_3 = c_3^E S_3 - e_{33} E_3 \tag{2.1}$$

$$D_3 = e_{33} S_3 + \varepsilon_3^S E_3 \tag{2.2}$$

All parallel electrode e_{33} electromechanical tests were performed using DMA. As previously mentioned, a custom electrode setup was designed in order to perform the fiber testing [16]. The setup shown in Figure 2.4 used two brass sphere electrodes that were electrically insulated using 3D printed plastic mounts. These combination electrode-mount members were inserted into the tensile grips on the DMA. First, the top mount was slid into the loosened grip and aligned in the center of the grip. A variable torque screwdriver was set to 50 cNm of torque, and the screws on the DMA grips were tightened. A 50 cNm torque was used to ensure that the mounts and electrodes did not move during the entire testing process. Then, the second mount was inserted into the loosened bottom grip. The grip was then only slightly tightened but still allowed for manual adjustments of the mount. The top grip with the inserted electrode and mount was moved very close to the bottom assembly. Then, the electrodes were aligned with one another, using the small indents on the spheres while visually inspecting for proper vertical alignment. Once the indents were aligned, the bottom DMA grip was tightened further using the torque screwdriver still set at 50 cNm. The TRIOS software was then used to tare the transducer holding the new mass of the electrodes and to zero out the new setup, where a zero gap corresponds to the tips of the spheres just touching. To complete the setup, the electrical lead wires from the spheres were connected with the hot wire and ground connections of the high voltage amplifier.

Next, the PZT fibers were cut into many small pieces of about 2 mm in length. The length was selected to keep the voltage required in the range of about 0V to 4kV. At the same time, this length would provide a wide range of electric fields that could be applied to the fiber. For each test, a small fiber specimen is grabbed using a pair of fine tip tweezers and is carefully placed between the indents on the sphere electrodes. To do this, the testing gap distance is set in the TRIOS software to a value of 0.12 mm below the length of the fiber. A testing gap smaller than the fiber's length is necessary because of the indents on the electrodes. The fiber is slightly recessed into the indents, decreasing the amount of fiber that is actually between the tips of the sphere electrodes. This smaller testing gap is what is used for determining what voltage to apply equivalent to a 2 MV/m electric field. Figure 2.7 shows the actual experimental setup for parallel electrode testing.

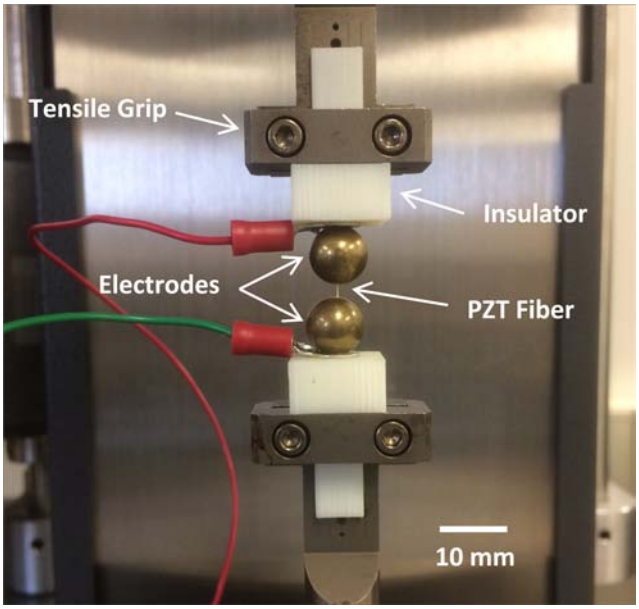

Figure 2.7: Parallel electrode experimental setup in the DMA

Once the fiber is in place, a compressive pre-load force of 0.5 N is applied to the fiber in order to help hold the fiber in place during the poling process. This pre-load, equivalent to a 10 MPa stress, was previously experimentally observed to produce the largest piezoelectric response in the fibers [16]. Once the pre-load was set, the function

generator and high voltage amplifier were set up as described in Section 2.3, and poling commenced.

In the previous work [16], the fiber was under a constant strain boundary condition during both poling and testing procedures. Although constant strain was desired for testing, a constant strain during the poling phase was later determined to be problematic. During fiber poling, a 2 MV/m electric field is applied to the fiber, and the fiber normally expands as the dipoles reorient themselves in line with the field. Blocking a fiber from expanding would create compressive stresses which may inhibit dipole orientation. Therefore, in this work, the blocked stress poling boundary condition in the TRIOS software was changed to a constant stress boundary condition. Under this condition, the DMA would allow the fiber to expand during the poling procedure while maintaining the same pre-load stress.

Using this new boundary condition, the DC voltage applied to the fiber is slowly ramped up to the voltage equivalent to a 2 MV/m electric field and is held there for 15 minutes to pole the fiber. Then, the field is slowly removed, and the function generator is put into AC voltage mode. After the poling process, the constant strain boundary condition is re-applied, and the fiber is tested under various sinusoidal electric fields ranging from 0.1MV/m to 1 MV/m (0.2MV/m to 2 MV/m amplitudes) at a frequency of 0.1 Hz. Additionally, a DC offset equal to the peak electric field is also applied so that only positive voltages are seen by the fiber. This is to ensure that the DMA is already reading compressive forces since positive voltages will cause the fiber to want to expand. As the fiber tries to expand, the constant strain (blocked stress) condition keeps the fiber from expanding, so the stress within the fiber increases as voltage increases.

During testing, as the AC electric field signals are applied, the TRIOS software records the force values output by the DMA in units of Newtons. At the same time, the DAQ records the voltage output from the function generator and the force from the DMA in units of Volts. The reason for using the DAQ is to have simultaneous voltage and force measurements. The peak-to-peak force found in the TRIOS software is used to

convert the force signal from the DAQ into values in Newtons. This process concept is shown in Figure 2.3. Then, from the force data, stresses can be calculated using the cross sectional area of the fiber. Lastly, the piezoelectric e_{33} coefficient is calculated from the maximum peak to peak value of stress divided by the maximum peak to peak electric field value using Equation (2.1) with the modification explained in Section 1.3.3. A concept of this calculation process is shown in Figure 2.8.

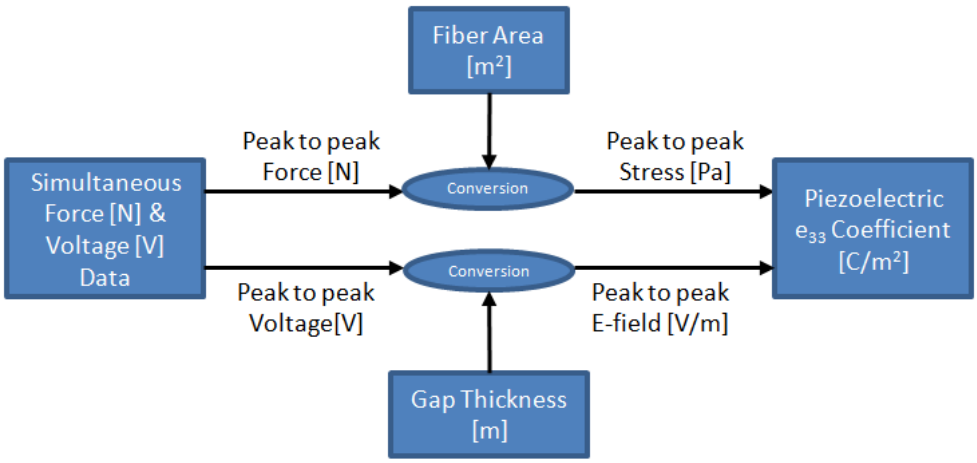

Figure 2.8: e_{33} measurement process

2.4.2 IDE e_{33} Testing Procedure

All IDE e_{33} electromechanical testing was performed using the DMA, where the tests were again modeled after those done previously by Wyckoff [16]. A special IDE assembly had to be created in order to test individual PZT fibers. A detailed description of these IDE assemblies can be found in Section 2.2.4. In order to replicate the concept shown in Figure 2.5, a fiber was cut to a length of about 75 mm. Then, the nuts and bolts attaching the acrylic plates were loosened enough to allow for the plates to be held separated from one another. The 75 mm fiber was carefully inserted between the plates and aligned in the middle of the screen printed electrodes so that the fiber was perpendicular to the electrode gaps. The plates were then lightly pressed together to hold the fiber in place while the plastic nuts were manually tightened. The nuts were tightened enough to hold the fiber in place between the electrodes and acrylic plates, but were not so tight that motion along the length of the fiber was restricted. It is unknown what force

was applied while fastening the assembly. The variable torque screwdriver was not used since it could not measure and apply torques small enough.

The IDE assembly with the fiber was then installed into the top tensile grip of the DMA. This step was particularly difficult due to the extreme brittleness and long length of the fiber specimen. The fiber needed to be aligned vertically between the grips since the DMA would only be able to read and record vertical forces or the vertical components of forces. To help with ensuring vertical installation, small grooves found on the tensile grips shown in Figure 2.2 (b) were used to help position the fiber. Once the fiber was aligned in the top grip, the two bolts of the grip were hand-tightened.

Using the TRIOS software, the DMA transducer was tared to eliminate the tensile force reading caused by the attached IDE assembly. The top grip was then slowly lowered, and the other free end of the fiber was inserted into the bottom DMA tensile grip. Before tightening, the testing gap was set in the TRIOS software to 50 mm. Although the acrylic plates were only about 38 mm long, a 50 mm gap was used to ensure that the IDE assembly was electrically insulated from the DMA. Any current passing through the DMA could damage the machine and potentially harm the user. Once the gap was set, the fiber was aligned (if necessary) to a vertical position, and the grip was tightened. A piece of electrical tape was placed onto each side of the bottom tensile grip. These pieces of tape were there as additional electrical insulation from the wires protruding from the IDE assembly. Although the wires were not in contact with the grip, the tape ensured that the wires could not come into contact with the DMA during testing. An image of a fully installed fiber and IDE assembly into the DMA grips can be seen in Figure 2.9.

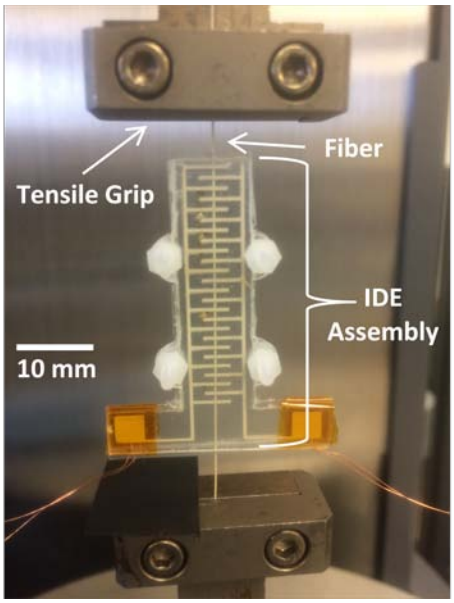

Figure 2.9: IDE experimental setup in the DMA

Once the assembly was installed, the electrical leads from the assembly were connected to the Trek high voltage amplifier, and the function generator was set to DC output mode. Before poling, the fiber was put under a tensile pre-load of 2 MPa. When the pre-load settled to 2 MPa, poling commenced. Similarly to the parallel test procedure, the poling boundary conditions were altered from the previous study [16] for the reasons discussed in the previous section.

Using this new boundary condition, the DC voltage applied to the fiber is slowly ramped up to a voltage equivalent to a 2 MV/m electric field. The field is held for 15 minutes in order to pole the fiber. Then, the field is slowly removed, and the function generator is put into AC voltage mode. After the poling process, the constant strain boundary condition is re-applied in the TRIOS software, a tensile pre-load of 5 MPa was applied to the fiber, and the fiber is tested under various sinusoidal electric fields ranging from 0.1MV/m to 1 MV/m at a frequency of 0.1 Hz. A tensile pre-load of 5 MPa was chosen to ensure that when the larger electric fields were applied during testing, the fiber would not enter into the compressive force zone. Normally, brittle materials are capable of withstanding significant compressive stresses. However, since perfectly vertical alignment could not be guaranteed with the setup used, compressive forces may have

damaged and broken the long, brittle fibers during testing. As the fiber tries to expand, the constant strain (blocked stress) condition keeps the fiber from expanding. Since the fiber is pre-loaded with a tensile stress, the stress within the fiber decreases as voltage increases.

Similarly to the parallel electrode tests, the TRIOS software records the force values output by the DMA in units of Newtons. At the same time, the DAQ records the voltage output from the function generator and the force from the DMA in units of Volts. The peak to peak force found in the TRIOS software is used to convert the force signal from the DAQ into values in Newtons. Lastly, the force data is converted into stresses, and the piezoelectric e_{33} coefficient is calculated from the maximum peak to peak value of stress divided by the maximum peak to peak electric field value using Equation (2.1) and the modification from Section 1.3.3, the process of which is again shown in Figure 2.8.

2.5 Electromechanical d_{33} Testing

The d_{33} coefficient is defined in the strain-charge form of the piezoelectric constitutive equations, found in Equations (2.4) and (2.4) [35]. Again, a complete description on what each variable means as well as subscripts can be found in Section 1.3.

$$S_3 = s_3^E T_3 + d_{33} E_3 \tag{2.3}$$

$$D_3 = d_{33} T_3 + \varepsilon_3^T E_3 \tag{2.4}$$

Due to limitations of the testing equipment used for d_{33} testing, only the IDE configuration could be tested. All IDE d_{33} coefficient testing was performed using the Trek high voltage amplifier, the HP function generator and an MTI Instruments 2100 model fotonic fiber optic sensor. To begin, a fiber was cut to a length of 45 mm. Then, the IDE assembly concept shown in Figure 2.5 is replicated using the same procedure

described in the previous section. Next, a small piece of reflective mirror tape is cut and placed on the tip of the fiber. This was done by placing the tape piece onto a flat surface sticky side up. Holding the fiber in the IDE assembly perpendicular to the flat surface, the fiber was brought closer to the tape and lightly tapped the tape, adhering it to the fiber. This step was done with the utmost care to avoid damaging or breaking the fiber. The entire assembly was then adhered via double-sided tape to a flat surface that could be moved in plane bi-axially using a combination of two perpendicular micrometers. Lastly, the wire leads of the IDE assembly were connected to the high voltage amplifier, and the function generator was set into DC output mode.

Since the fiber ends are not being held by any external fixture, the fiber experiences a zero stress (free strain) boundary condition for poling and testing, which is highly desired so that Equation (2.3) can be modified as explained in Section 1.3.3. For poling, the voltage output on the function generator is slowly ramped up to a voltage equivalent to a 2 MV/m electric field. This electric field is held at 2 MV/m for 15 minutes to allow sufficient time for the dipoles in the fiber to reorient and align with the field. Then, the field is slowly removed, and the function generator is set to AC voltage output mode. Next the fiber optic sensor probe is installed into a fixture to hold it in place, and it is slowly and carefully aligned axially with the fiber end with the reflective tape on it for calibration. The calibration process in detail, which was outlined in the instruction manual of the fiber optic sensor, can be found in Appendix B.

Once the fiber optic sensor was properly calibrated, testing commenced. Similar to e_{33} testing, a range of sinusoidal AC voltages are applied to the fiber equivalent to electric fields ranging from 0.1 MV/m to 1 MV/m. When each field is applied, the fiber expands and contracts, which is known as the piezoelectric strain in the material. For each electric field application, the maximum and minimum values displayed on the sensor are recorded. These values are in units of volts and need to be converted into units of micrometers using a conversion factor. The factor used for this study is 0.00052 μm/mV, which can be found on the probe itself. Once displacement is known, strain can be calculated using the active area of the IDE (24 electrode gaps * 750 μm). Lastly, the

peak-to-peak value of strain induced in the fiber is divided by the peak to peak value of the applied electric field in order to determine the piezoelectric d_{33} coefficient using Equation (2.3) and the modification from Section 1.3.3. A flow diagram of this calculation process can be seen in Figure 2.10.

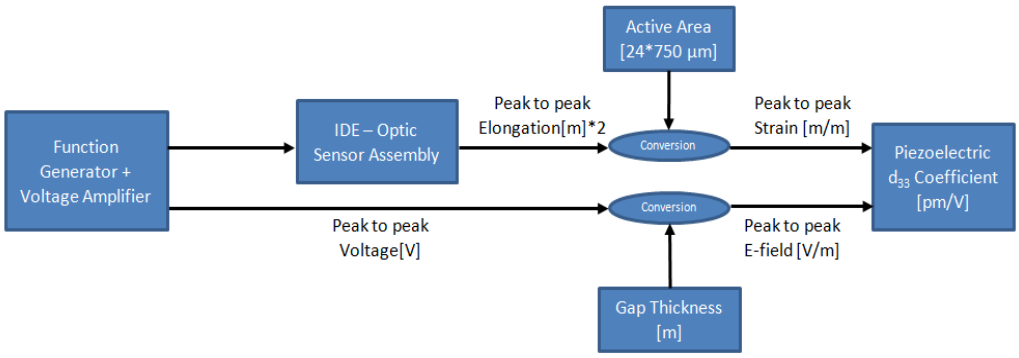

Figure 2.10: d33 measurement process

In this chapter, the experimental materials used, equipment utilized, and processes applied in this study were outlined. Two different electrode configurations were discussed for electromechanical characterization purposes: (1) parallel electrodes and (2) interdigitated electrodes. Additionally, two piezoelectric coefficients, the e_{33} and the d_{33} coefficients, and their related equations were discussed. The next chapter will present in detail the experimental processes utilized as well as the results of the experiments conducted in order to characterize these coefficient values using the different electrode configurations.

Chapter 3
Determination of the Experimental Piezoelectric Coefficients: e_{33} and d_{33}

In this chapter, the focus is on improving the experimental setups from [16] in order to improve the determination of the e_{33} values. Additionally, the results of the experimental procedure designed for testing the d_{33} coefficient of the fibers are presented and discussed. Lastly, the piezoelectric charge coefficient, g_{33}, of individual PZT fibers is calculated based on measured d_{33} and ε_{33}.

3.1 Parallel Electrode Experiments: e_{33} results

3.1.1 The Effect of Boundary Conditions

The piezoelectric e_{33} coefficient is a relational value quantifying the converse piezoelectric effect where stress is induced in a piezoelectric material when an external electric field is applied and is defined in Equation (2.1). This relationship can be seen when a zero-strain condition is applied to Equation (2.1) and becomes:

$$T_3 = -e_{33} E_3 \tag{3.1}$$

In previous work [16], a blocked stress boundary condition, otherwise known as a zero-strain boundary condition, was applied during both the poling and testing phases of e_{33} characterization. However, as discussed in Section 2.4.1, applying this type of boundary condition was determined to be problematic. When a PZT fiber is poled, a high DC electric field is applied to the fiber and the dipolar domains within the fiber rotate and reorient themselves with the applied field. This reorientation is typically accompanied with an expansion of the fiber. If the fiber is blocked from expanding during poling, then poling is inhibited. Therefore, when the poling electric field is removed, the remnant polarization in the fiber is lower than the optimum value. Since piezoelectric responses

scale with the remnant polarization, a lower remnant polarization in the fiber will result in an overall weaker electromechanical performance. The induced stress coefficient results from this previous study are given in Table 3.1. Although all of the reported values deviated from the bulk PZT e_{33} coefficient of 15.8 C/m^2, the experimental values more importantly deviated from the predicted values, and this deviation was likely partly due to the problematic poling boundary condition used.

Table 3.1: Experimental and model predicted values from a previous study [16]

	Experimental (C/m^2)	Predicted (C/m^2)
Parallel Electrode Setup	2.8	6
IDE Setup	1.5	4

For this study, instead of applying a blocked stress boundary condition, a constant stress condition (free-strain) condition was used. Under a constant stress boundary condition, the DMA allows the fiber to expand during the poling phase while simultaneously maintaining a constant pre-stress to the fiber. The fiber expansion during poling provides a chance for the dipolar domains to fully align with the electric field, increasing the overall potential remnant polarization in the fiber. Once inserted, a 4 MPa pre-stress was applied to the fiber and the fiber was poled in a 2 MV/m electric field. After poling, the constant stress boundary condition was changed to a blocked stress (zero-strain) boundary condition, the pre-stress in the fiber was increase to 10 MPa, and testing commenced. Data was collected from nine fibers tested under these conditions using the process outlined in Section 2.4.1.

Under each electric field tested, the fibers display a hysteresis-like behavior between the stress induced in the fiber and the electric field applied. An example of this behavior is shown in Figure 3.1. As mentioned previously in Section 2.4.1, the fibers were tested under AC electric fields ranging from 0.1 to 1 MV/m at 0.1 Hz. Additionally a DC offset equal to the field strength was applied to ensure only positive fields were applied to the fiber. Therefore, in Figure 3.1, the fiber tested under a 1 MV/m AC field with a +1 MV/m DC offset saw fields ranging from 0 to 2 MV/m rather than ± 1 MV/m.

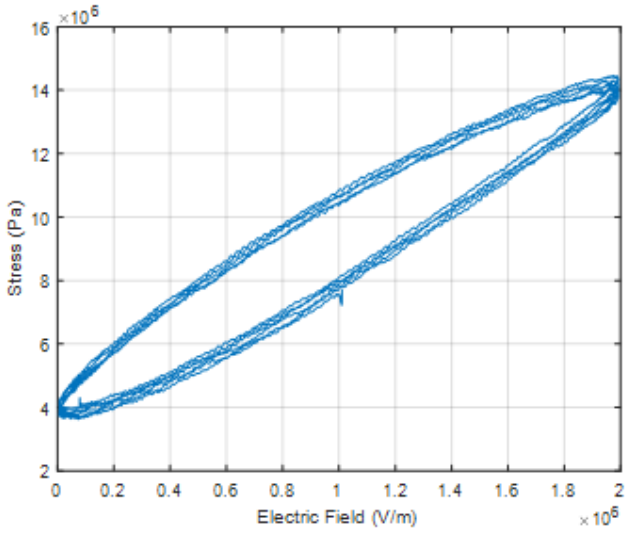

Figure 3.1;Hysteresis behavior of a PZT fiber in a parallel electrode setup tested at 0.1 Hz under a 1 MV/m AC electric field with a +1 MV/m DC offset applied

The e_{33} coefficient was extracted from each hysteresis loop using the peak-to-peak (maximum and minimum) stress and peak to peak electric field values, as explained in Section 2.4.1. Then, the e_{33} values from the nine fibers tested were averaged and plotted against their corresponding AC electric fields, as shown in Figure 3.2. As can be seen on the plot, the e_{33} values all tested at 0.1 Hz ranged from about 3.8 ± 0.7 C/m^2 at a 0.1 MV/m electric field to about 5.1 ± 0.7 C/m^2 at a 1 MV/m electric field.

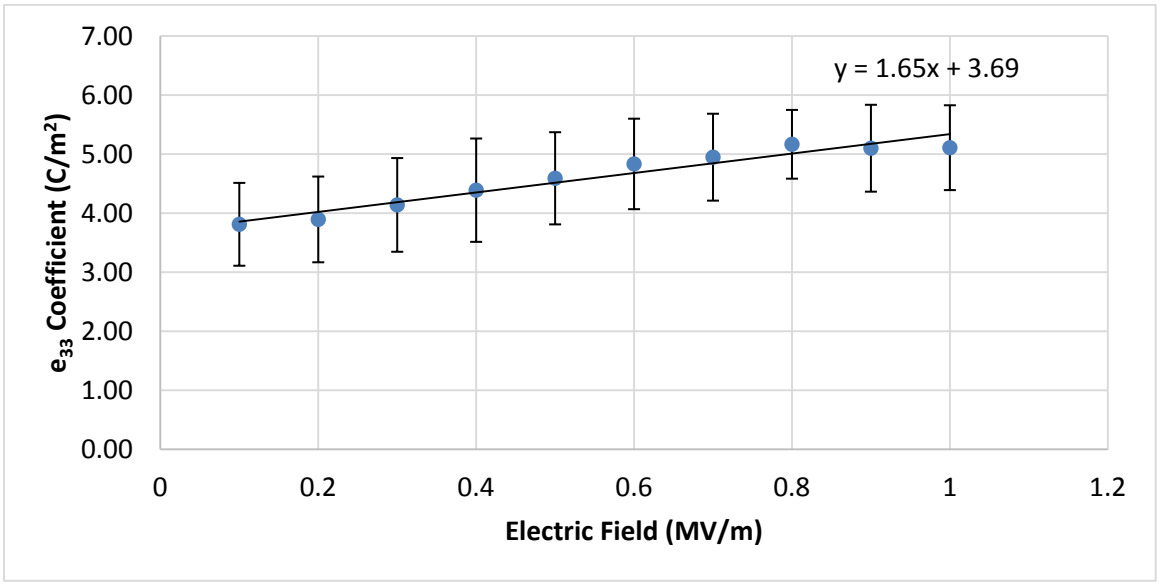

Figure 3.2: Parallel electrode e_{33} results using a constant stress poling boundary condition

Experimental results show that the e_{33} coefficients of the fiber vary in a non-linear fashion with the applied AC electric field. According to Damjanovic and Demartin [36], this behavior common to ferroelectric materials can be modeled using a modified version of the Rayleigh Law, which was originally discovered to characterize the nonlinear behavior of ferromagnetic materials. In their article, Damjanovic and Demartin explain that a portion of the Rayleigh law is as follows:

$$\mu = \mu_{init} + \alpha H_o \tag{3.2}$$

where μ is the magnetic permeability, μ_{init} is the permeability at zero magnetic field, alpha is the Rayleigh coefficient, and H_o is the applied magnetic field. By applying principles of ferroelectrics, the Rayleigh law in Equation (3.2) can be transformed into:

$$e_{33} = e_{33,init} + \alpha E \tag{3.3}$$

If the principles of Equation (3.3) are applied to Figure 3.2, then the slope of a linear fit trendline represents the Rayleigh coefficient, α, and $e_{33,initial}$ coefficient, which refers to the e_{33} value at zero electric field applied, is the y-intercept of the trendline. For characterization purposes, the $e_{33,initial}$ value determined is used for comparison with the published predicted value [16]. Under the altered poling boundary condition, the $e_{33,initial}$ value determined is 3.7 C/m^2.

Table 3.2: Comparing the new poling condition parallel e_{33} value to previously published data

	Experimental e_{33} (C/m^2)	FEA Model Predicted e_{33} (C/m^2)
Published parallel e_{33}	2.8 [16]	6 [16]
New Poling Boundary Condition	3.7	

As can be seen in Table 3.2, the new poling boundary condition improved the measured piezoelectric response of the PZT fibers in a parallel electrode setup, but the

new value still deviated from the predicted response using FEA analysis under a blocked stress testing condition at low electric fields.

3.1.2 The Effect of the Pre-load Magnitude

After reviewing the results from the experiments run with the altered poling boundary condition, the measured e_{33} response of the fiber improved and was closer to the FEA-predicted value but still low. Therefore, the question arose "what else could be improved in the experiment?" The value of the pre-load applied to the fiber during testing was the next major factor that could possibly account for difference between the experimental and model predicted values. A pre-load range of 10 - 20 MPa was originally determined to produce the greatest e_{33} piezoelectric output [16]; so, a pre-load of 10 MPa was used for the testing portion of the experiments. However, this pre-load was determined for the blocked stress condition used by the previous study [16]. Since this boundary condition was modified in the current study, investigating a better pre-load value is done next.

For an ideal experiment, the boundary condition used for testing would be a true zero strain starting condition. This means that no pre-load stress would be applied to the fiber before testing commenced. However, implementing this boundary condition is not possible with the testing equipment used in this study. Therefore, for the next round of experiments, fibers were installed between the electrodes, and a 4 MPa pre-load stress was applied. A value of 4 MPa was chosen because it was 60% lower than the original 10 MPa applied but was large enough to allow for good contact between the fiber and the electrodes. Data was collected from six fibers tested under these conditions.

As before, the e_{33} coefficients were extracted from the hysteresis loops using the peak to peak stress and electric field values. The e_{33} coefficients for each electric field were averaged and then plotted against their respective AC electric field. This plot can be seen in Figure 3.3. The e_{33} values all tested at 0.1 Hz ranged from about 4.2 ± 0.55 C/m^2 at a 0.1 MV/m electric field to about 5.4 ± 0.7 C/m^2 at a 1 MV/m electric field. Using the modified Rayleigh law from Equation (3.3), the $e_{33,initial}$ value reported from

this round of testing was 4.2 C/m^2. Changing the testing pre-load stress expectantly did improve the e_{33} response in a PZT fiber from a value of 3.7 C/m^2 to 4.2 C/m^2.

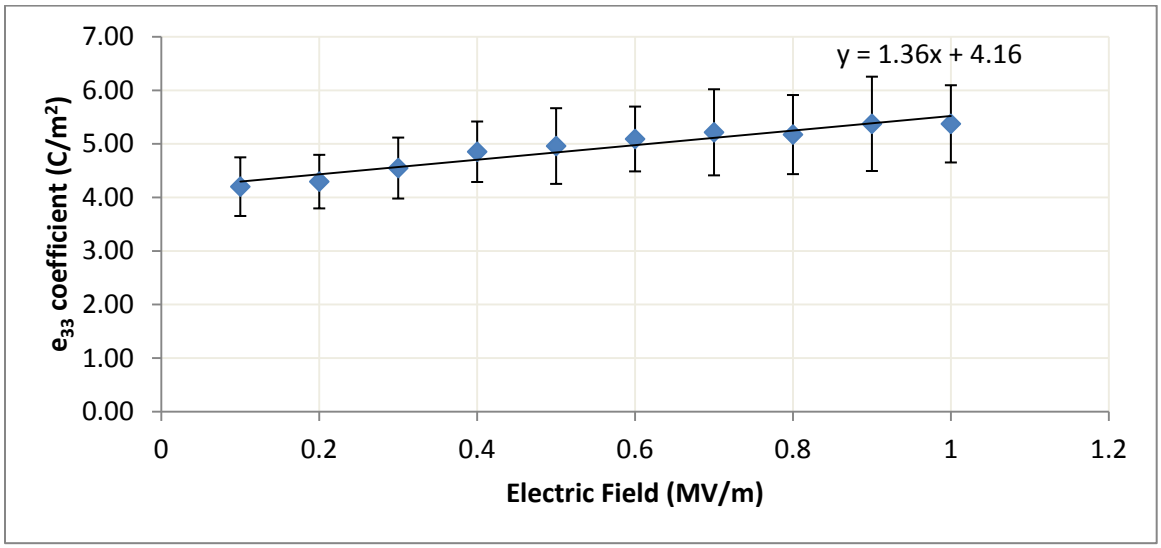

Figure 3.3: Parallel electrode test e_{33} results using a 4 MPa testing pre-load

3.1.3 The Effect of Electrode Contact

As mentioned in the previous section, a high enough pre-load stress had to be applied to the fiber to ensure that the fiber was in good contact with electrodes. As mentioned in Section 2.4.1, a fiber is cut to the desired 2 mm length using a single edge, flat razor blade. Since the PZT fibers are inherently brittle, the result is a rough fracture surface profile due to cutting. Scanning electron microscopy (SEM) was utilized to view these rough surface profiles, and these SEM images can be seen in Appendix D. Additionally, the indents on the electrodes themselves do not provide a flat surface for the fiber tips to press against; rather, they exhibit a slightly beveled profile since they were created using small drill bits. The proposed issue with having these rough surface profiles was that pressing the fiber against the brass electrodes likely caused the small "peaks" to crush into a powder. This would form a barrier between the electrodes and the rest of the fiber, decreasing electrical contact. In order to solve this problem, the fiber tips are dipped in silver ink before being put in contact with the electrodes [16]. Images of silver dipped fiber tips can also be found in Appendix D.

An additional benefit of adding silver to the fiber ends is that the silver, being a softer material than PZT, would conform to the electrode indent, enhancing the electrode's ability to hold the fiber in place. With both tips coated, the fibers were placed onto a paper grid and were covered, allowing the silver paint to dry for a 24 hour period. After the 24 hour drying period, fibers were loaded into the parallel electrode assembly, and testing commenced. The dry silver ink was again much softer than the PZT fiber, which allowed the ink to better conform to the indents on the electrodes, improving both the mechanical and electrical connections between the fiber and the electrodes. Due to the enhanced mechanical contact between the fiber and electrodes, a lower pre-load stress of 2 MPa was implemented for both the poling and testing procedures. Then the fiber was tested using the same boundary conditions and sinusoidal electric fields as before. Data was collected from six fibers tested under these conditions.

The piezoelectric e_{33} coefficients were extracted from the hysteresis loops generated for each electric field tested. Then, as before, the coefficients for each electric field were averaged and plotted against their respective electric field, shown in Figure 3.4. The resulting stress coefficients ranged from about 4.6 ± 0.45 C/m^2 at a 0.1 MV/m electric field to about 5.8 ± 0.8 C/m^2 at a 1 MV/m applied electric field. Applying the modified Rayleigh law from Equation (3.3), the reported $e_{33,initial}$ value extracted as the y-intercept of a linear fit trendline to the plot in Figure 3.4 was about 4.8 C/m^2. This value showed that the enhanced contact between the fiber and electrodes due to the silver paint did increase the observed electromechanical stress response in the fibers. Table 3.3 shows the progressive improvement of the measured parallel electrode e_{33} value obtained from each experimental alteration implemented.

Table 3.3: Induced stress coefficients measured from each parallel electrode experimental alteration implemented

Testing Alterations	Experimental e_{33} (C/m^2)	FEA Model Predicted e_{33} (C/m^2)
Published parallel e_{33}	2.8 [16]	6 [16]
Poling Boundary Condition	3.7	
Lowering Pre-Stress	4.2	
Silver-dipped Fibers	4.8	

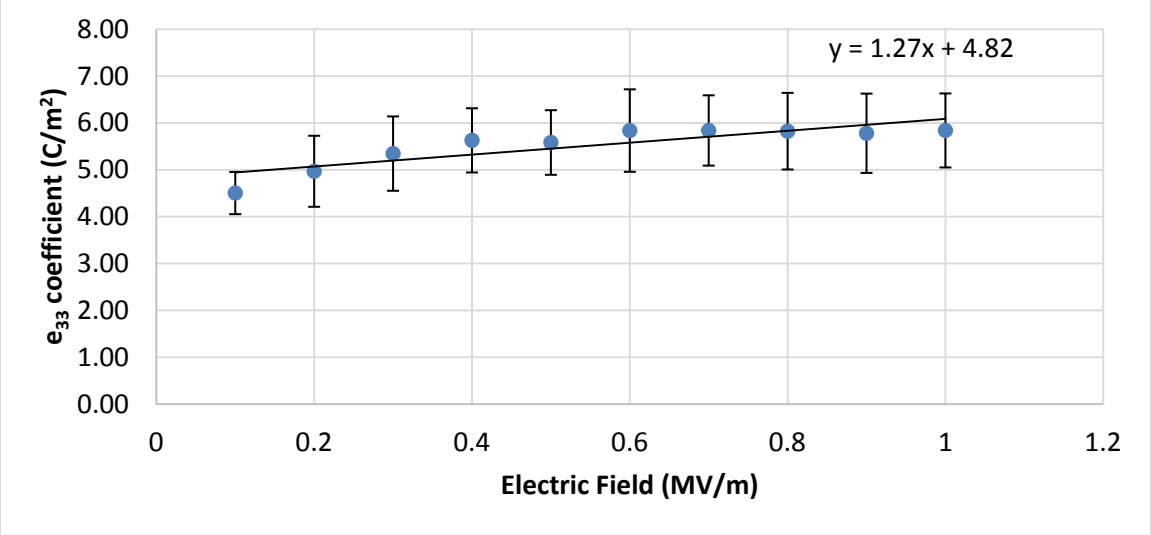

Figure 3.4: Parallel electrode test e_{33} results using silver-tipped fibers and a 2 MPa pre-load stress

The newest reported value of 4.8 C/m^2 is the closest yet to the FEA model predicted value of 6 C/m^2, but it is still not as high as was expected. One major factor that could possibly account for the deviation between model and experimental values is the difficulty of fiber installation. The piezoelectric constitutive equations and modified Rayleigh law equation used for this study refer to electric fields applied and stresses induced along the fiber's length, also known as the '33'setup. Applying these equations to the data gathered in the experiments assumes that the fibers are perfectly installed meaning that they are completely vertically aligned. However, perfect installation is nearly impossible with the current setup, and repetitive alignments are impossible. When a fiber is installed at an angle off of the vertical axis, the dipoles within the fiber do not align in the true '33' direction, which would skew the true e_{33} capabilities of the fiber. Furthermore, only the vertical components of the induced stresses would be read by the

DMA, rather than the true stress levels being induced in the fiber, skewing results. An additional source of error could be from the value reported by the FEA model. According to Wyckoff [16], the parallel model was created using some properties estimated based on bulk PZT properties. Additionally, the model was created as a linear model since only a very low electric field was applied. These assumptions could affect the predicted induced stress response of the fibers between parallel electrodes, contributing to the difference between experimental and predicted coefficient values.

3.2 Interdigitated Electrode Experiments: e_{33} results

3.2.1 The Effect of Boundary Conditions

Similarly to the parallel electrode setup, the IDE experimental process used in previous work [16] incorporated a zero strain (blocked stress) boundary condition on the fiber during both the poling phase the sinusoidal electric field testing phase. The same issue, therefore, was present for IDE experiments. During the poling phase, as the large electric field is applied to the fiber, the fiber wants to expand, but a blocked stress condition keeps it from doing so. The result is poorer dipolar orientation with the field, and therefore poorer remnant polarization in the fiber when the field is removed. As the first experimental improvement, the poling boundary condition in the TRIOS software was changed to a constant stress boundary condition which would allow fiber expansion during poling. Fibers were cut to roughly 75 mm lengths and carefully installed into the IDE assembly as described in Section 2.4.2. The assembly was then installed into the tensile grips of the DMA using a 50 mm testing gap, and the fiber was placed under a 2 MPa tensile stress for poling using the new constant stress boundary condition. After poling, a blocked stress boundary was applied to the fiber as well as a tensile 5 MPa stress to help vertically align the fiber assembly as well as keep the fiber from entering the compressive stress zone. Since perfectly vertical installation could not be guaranteed, a compressive force may damage or break the fiber. Data was collected from five fibers tested under these conditions.

Due to the irreversible domain wall movement that occurs in ferroelectric materials, the PZT fiber in the IDE assembly exhibited a hysteresis-like electromechanical induced stress behavior, similar to fiber's response in a parallel electrode setup. An example of this hysteresis behavior can be seen in Figure 3.5. Unlike the fiber's responses in parallel electrodes, this IDE hysteresis plot shows a negative correlation between stress induced in the fiber and electric field applied to the fiber. This is due to fact that the fiber is initially loaded with a tensile stress to keep it out of the compressive zone. As positive electric fields are applied during testing, the fiber expands, decreasing the value of force the DMA records. For the parallel electrode tests, the expansion behavior of the fiber results in an increasing force value measured by the DMA. For IDE tests, this expansion behavior results in a relaxation of the force values measured by the DMA. Additionally, since the pre-load tensile stress value was far enough away from the compressive stress zone, no voltage DC offset was used. Therefore, the plot in Figure 3.5 shows electric fields ranging from -1 MV/m to 1 VM/m rather than from 0 MV/m to 2 MV/m like the parallel electrode hysteresis plot shows.

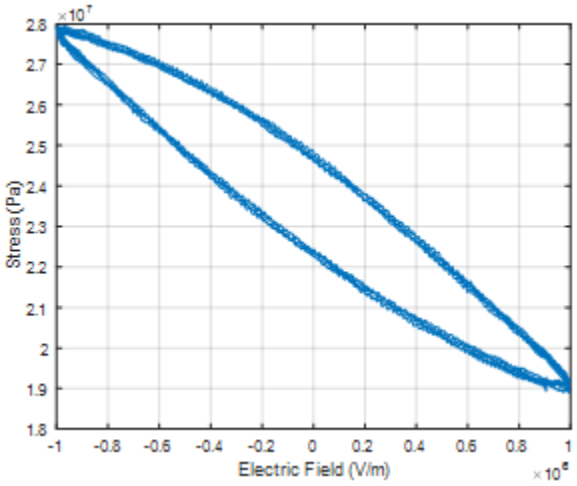

Figure 3.5: Hysteresis behavior of a PZT fiber in an IDE assembly tested at 0.1 Hz under a 1MV/m AC electric field with no DC offset applied

Using the same method exploited in the parallel electrode fiber tests, e_{33} coefficient are extracted from the hysteresis loops using the peak-to-peak stress and electric field values. Using this method negated the effects of the negative stress to field correlation. Then, the e_{33} coefficients at each electric field from the five fibers tested

were averaged, and the average values were plotted against their respective AC electric fields as shown in Figure 3.6.

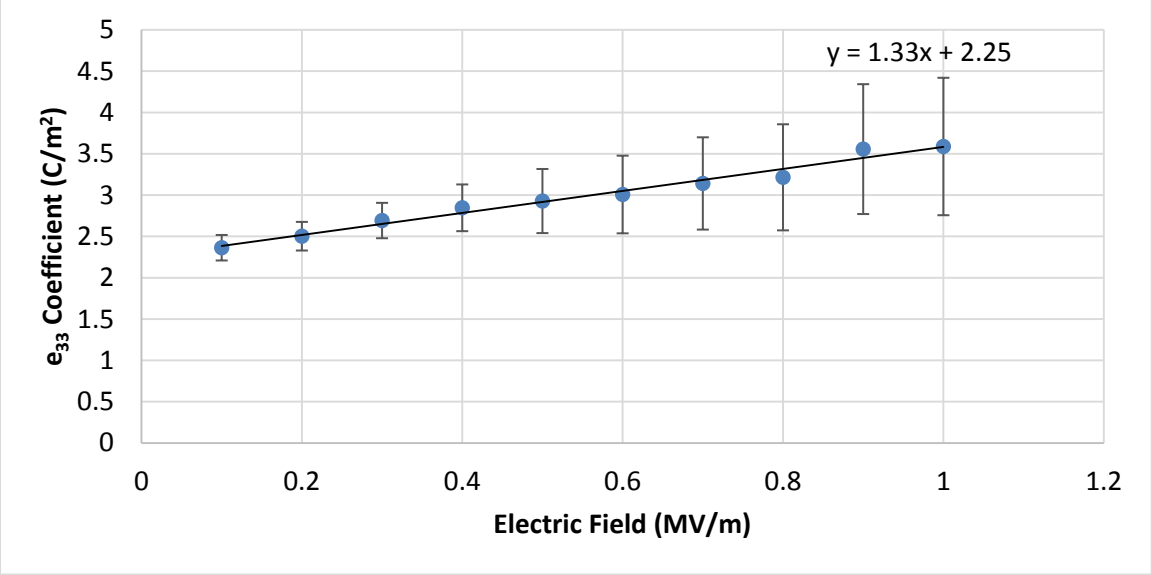

Figure 3.6: IDE test e_{33} results using a constant stress poling boundary condition

According to the plot, the observed induced stress response of a PZT fiber in an IDE assembly increases with increasing applied electric fields. The recorded values ranged from about 2.4 ± 0.15 C/m^2 at 0.1 MV/m electric field to about 3.6 ± 0.8 C/m^2 at a 1.0 MV/m electric field. Then, the same modified Rayleigh law equation used for parallel testing was paralleled to a linear fit trendline applied to the plotted e_{33} data. The resulting reported $e_{33,initial}$ value using the new poling boundary condition was 2.3 C/m^2. This value, as shown in Table 3.4, is expectantly higher than Wyckoff's observed electromechanical stress response of 1.5 C/m^2 [16]. However, there was still a gap between the obtained value and the FEA model predicted value of 4 C/m^2 found under blocked stress testing conditions at a low electric field.

Table 3.4: Comparing the new poling condition IDE e33 value to previously published data

	Experimental e_{33} (C/m^2)	FEA Model Predicted e_{33} (C/m^2)
Published IDE e_{33}	1.5 [16]	4 [16]
New Poling Boundary Condition	2.3	

3.2.2 The Effect of Varying Fiber Properties

As briefly mentioned in the previous section, the fiber-IDE assembly was tested in the DMA using a 50 mm test section gap, an example of which is shown in Figure 3.7. The IDE assembly itself was only about 38 mm long, leaving a 12 mm space for aligning the assembly in such a way that only the PZT fiber came in contact with the tensile grips of the DMA. Having the IDE assembly touch the grips could have resulted in unwanted stress concentrations, skewing potential electromechanical results as well as possibly putting the fiber at risk of breaking.

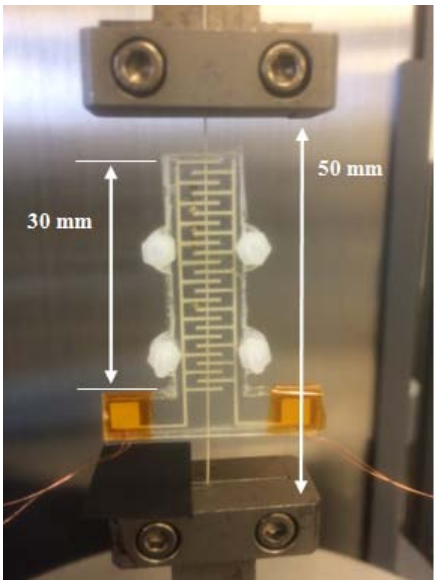

Figure 3.7: IDE assembly installed into the DMA for testing

In the currently used testing setup, only about 30 mm of the 50 mm section of PZT fiber in the gap is actually poled and affected by the electric fields applied. As was previously studied by Wyckoff [16], poled and unpoled PZT fibers do not share identical mechanical and dielectric properties. This means that a significant portion of the fiber in the testing section (40%) had properties that differed from those of the remaining portion of poled fiber. Therefore, it was questioned as to whether or not the unpoled fiber in the testing gap was the cause of the smaller than expected measured e_{33} values. Furthermore, the large portion of upoled fiber may be creating unnecessary and unwanted torsion and

bending stresses in the fiber due to the difficulties of installation. So, the next major improvement to the testing setup was a decrease in the testing section gap.

PZT fibers were cut to 70 mm lengths and carefully installed into the IDE assembly. Then, the fiber-IDE assembly was installed into the DMA grips using a 45 mm testing gap. The 5 mm gap decrease allowed for a smaller amount of unpoled fiber in the testing section. The assembly was again installed in such a way that only the fiber was in contact with the tensile grips. Once the assembly was in place, testing commenced using the same procedure as before. Data was collected from five fibers tested under these conditions. The induced stress coefficients were extracted from the hysteresis loops, and the average values were plotted against their respective electric fields. This plot can be found in Figure 3.8.

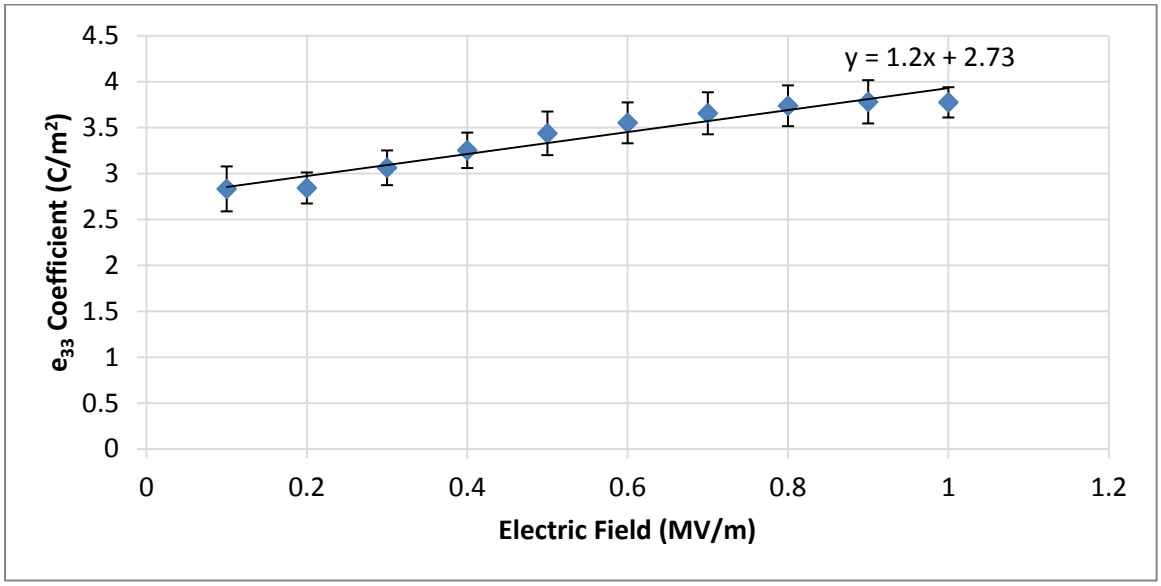

Figure 3.8: IDE test e_{33} results using a 45 mm testing gap

The obtained e_{33} values ranged from about 2.8 ± 0.24 C/m^2 at a 0.1 MV/m electric field to about 3.8 ± 0.2 C/m^2 at an applied 1 MV/m electric field. Applying the modified Rayleigh law in Equation (3.3), the reported $e_{33,initial}$ value is about 2.7 C/m^2. This value is an improvement over the previously obtained $e_{33,initial}$ value, confirming the

expectation that the significant portion of unpoled fiber in the testing section is indeed impacting the true electromechanical induced stress response of an individual PZT fiber.

3.2.3 A New IDE Design

From the e_{33} results of the decreased gap test, the first thought was to decrease the gap further. However, decreasing the gap by another 5 mm would only leave 2 mm of space to properly align the IDE assembly so that only the fiber would be touching the grips, which would have proven to be quite challenging. Then, it was realized that the current IDE design encompassed about 6-8 mm of unpoled fiber within the assembly itself. With a simple redesign, the IDE assembly could be shortened by 5 mm while maintaining an identical electrode finger pattern, and the redesign was implemented. A concept comparison of the new design to the old design can be seen in Figure 3.9.

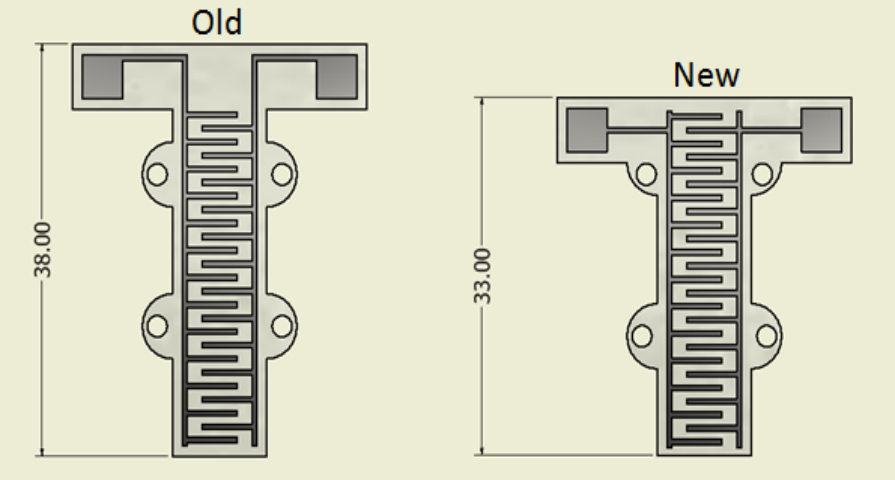

Figure 3.9: A comparison of the new IDE design to the old design

Mirrored screens of the new design were ordered and new electrodes were screen printed using the process explained in Appendix A. Additionally, a new acrylic plate was designed, and plates were laser cut. New IDE assemblies were pieced together using the same process described in Section 2.2.4. Fibers were cut to 60 mm lengths and were carefully installed into a new IDE assembly. The fiber-IDE combination assembly was then installed into the tensile grips of the DMA using a 40 mm testing gap. As before,

the assembly was installed in such a way so that only the fiber was in contact with the grips. With this new IDE design and 40 mm testing gap, only about 10 mm of the fiber was unpoled, decreasing the percentage of unpoled fiber from the original 40% down to 25%. The fiber-IDE assembly was tested using the same procedures as before, and data was collected from six fibers tested under these conditions.

From the stress-electric field hysteresis loops generated, the e_{33} coefficient values were extracted from the slopes of linear fit trendlines to the loops, and the average coefficients were plotted against their respective electric fields, shown in Figure 3.10. The induced stress coefficients gathered ranged from about 3.5 ± 0.24 C/m^2 at an applied electric field of 0.1 MV/m to about 4.6 ± 0.3 C/m^2 at a 0.1 MV/m electric field. Applying the modified Rayleigh law equation, the reported $e_{33,initial}$ value improved to about 3.5 C/m^2, which is desirably close to the predicted value of 4 C/m^2, further supporting the idea that the unpoled fiber in the testing section is influencing the true electromechanical induced stress behavior of a PZT fiber. Table 3.5 shows the progressive increase in the obtained IDE e_{33} response coefficient of the fiber from each experimental alteration implemented.

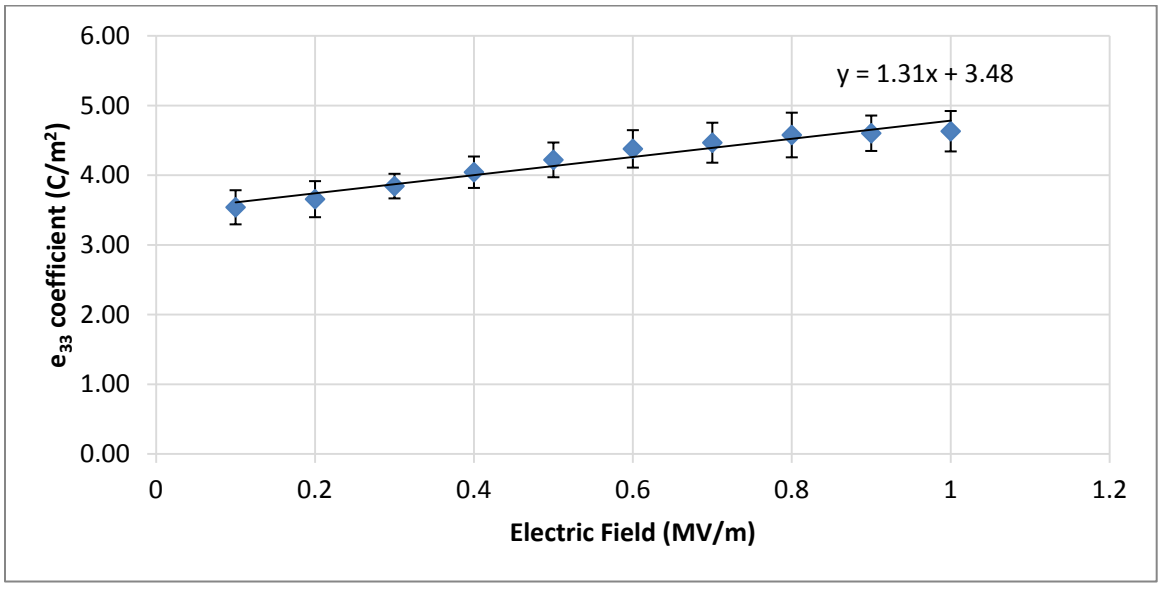

Figure 3.10: New IDE test e_{33} results using a 40 mm gap

Table 3.5: Induced stress coefficients measured from each IDE experimental alteration implemented

Testing Alterations	Experimental e_{33} (C/m^2)	FEA Model Predicted e_{33} (C/m^2)
Published parallel e_{33}	1.5 [16]	4 [16]
Poling Boundary Condition	2.3	
45 mm Testing Gap	2.7	
New IDE Design	3.5	

The latest reported value is close to the model predicted value, but there is still a slight difference in the values. This difference in values can be attributed to various factors in both the experiments and the FEA model previously created by Wyckoff [16]. For the experiments conducted in this study, one major factor that is likely affecting the measured behavior of the fibers is the remaining amount of unpoled fiber in the testing section. Even with the new IDE design, a quarter of the testing section is composed of unpoled PZT fiber, which has mechanical and electromechanical properties that differ from poled PZT fiber [16]. Based on the results from decreasing the testing gap, eliminating this remaining unpoled fiber from testing section might help close the gap between the experimental results and the model predicted results. Additionally, due to the difficult nature of assembly installation into the DMA, unwanted torsion and bending stresses could potentially be present, skewing the true electromechanical responsive nature of the PZT fiber.

As mentioned, the model created by Wyckoff [16] could also have contributed to the difference in experimental and predicted behavior of fibers between IDEs. Similar to the parallel model, Wyckoff's IDE model was created using piezoelectric strain properties estimated from bulk PZT property values; it was also similarly created as a linear model since only a very low electric field was applied. Furthermore, the IDE model assumes that the fiber between the electrodes is poled uniformly through the fiber based on the properties applied. In reality, though, the directions of poling would follow the same non-uniform behavior as the electric field created by the IDEs; so, the model's uniform poling of the fiber could affect the true predicted response of the fiber between IDEs.

3.3 Interdigitated Electrode Experiments: d_{33} results

The piezoelectric d_{33} coefficient is most often defined as a quantification of the converse piezoelectric effect, an effect where strains are induced in a material from the application of an external electric field. This relationship can be seen when a zero stress, or free strain, boundary condition is applied to Equation (2.3) and becomes:

$$S_3 = d_{33} E_3 \tag{3.4}$$

The experimental setup used in this study utilizes the free strain boundary condition in order to characterize the PZT's induced strain coefficient directly. For the experiment, a fiber was cut to a length of about 45 – 50 mm and inserted into the IDE assembly. A small piece of reflective tape was applied to the fiber as explained in Section 2.5. The fiber-IDE assembly was adhered to a flat surface capable of translating in an X-Y plane via two micrometers. The fiber was poled under a 2 MV/m DC electric field using the function generator and high voltage amplifier. Lastly, before testing began, the assembly was aligned with the fiber optic sensor probe and the sensor was calibrated; a detailed explanation of the fiber optic sensor setup and calibration can be found in Appendix B. Once all of the equipment had been properly set up and calibrated, testing began. The same AC electric fields applied during e_{33} testing ranging from 0.1 MV/m to 1 MV/m were applied at a 0.1 Hz frequency. A total of ten fibers were tested under each electric field load. For each field application, the fiber expanded and contracted according to the magnitude of the field applied.

For each electric field applied, a d_{33} coefficient was determined using the process outlined in Section 2.5. Similarly to the process used for e_{33} testing, the resulting d_{33} coefficient values from the ten fiber tests were averaged and plotted against their respective AC electric fields. This plot can be found in Figure 3.11.

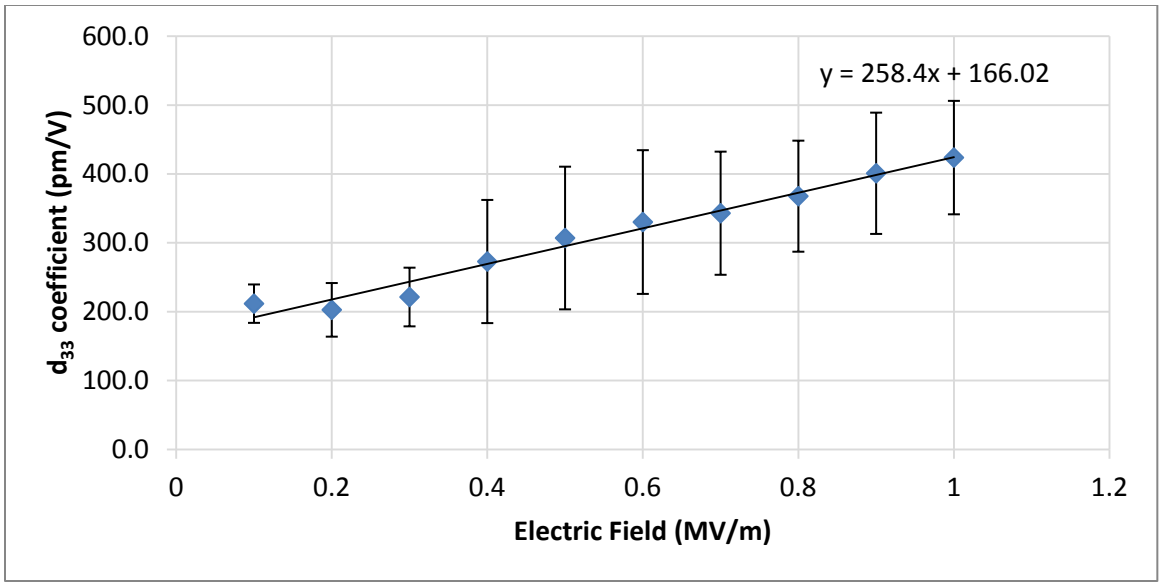

Figure 3.11: Averaged IDE test d_{33} coefficient results

Experimental results show that the d_{33} coefficients of the fiber vary in a non-linear fashion with the applied AC electric field. This non-linear behavior, as explained by Damjanovic and Demartin [36], can be modeled using a modified version of the Rayleigh Law of ferromagnetics. In a similar manner as was done for e_{33} testing, applying certain ferroelectric principles to the portion of the Rayleigh Law in Equation (3.2) results in another modified Rayleigh Law equation of the form:

$$d_{33} = d_{33,init} + \alpha E \tag{3.5}$$

Correlating Equation (3.5) with a linear trendline fit to the plot in Figure 3.11, the slope of the trendline represents the modified Rayleigh coefficient, α, and the y-intercept of the trendline represents the $d_{33,initial}$ value. For fiber characterization purposes, the $d_{33,initial}$ value is used as the reported induced strain coefficient for a fiber in an IDE setup. Applying the modified Rayleigh law, a d_{33} value of about 166 pm/V was determined for PZT fibers in an IDE setup. This value is significantly lower than the reported value of 374 pm/V for bulk PZT [31]. At first glance, this value is well below the general assumption that fiber properties are about 65-75% of the bulk material property values. One factor that could contribute to this discrepancy is the fact that proper alignment of

the testing setup is difficult and not feasibly repeatable at the moment. Proper alignment refers to a setup in which the fiber is coaxially aligned with the fiber optic probe, and the reflective tape on the tip of the fiber is perpendicular to the probe tip. For the actual testing setup, though, alignment was all done via visual inspection, which is inherently prone to error. Additionally, even though the fiber optic sensor could be setup in a high resolution mode, displacement readings at very low electric fields (0.1 MV/m and 0.2 MV/m) were not necessarily accurate.

Another source of error could be from imperfections of the printed IDEs. Calculations assume perfect 750 μm electrode gaps and perfect 500 μm wide electrodes, but in practice, the electrodes and gaps are nowhere near perfect. Using an optical microscope, several printed electrodes were studied. Widths of the electrodes and gaps were recorded and averaged. Studying various electrode widths and gap widths revealed that the average electrode width was about 506 ± 16 μm, and the average gap width was about 748 ± 14 μm. As can be seen by the standard deviation, the electrode and gap widths were not consistent in size, which would effectively alter the net strength of the electric field applied in each gap. Additionally, the amount of fiber that is actually in this "active" section in the gap would also change. An example of the electrode and gap widths under an optical microscope can be seen in Figure 3.12. Official conclusions about the validity of the measured d_{33} responses, however, cannot be made due to a lack of published data on individual fiber properties in an IDE setup.

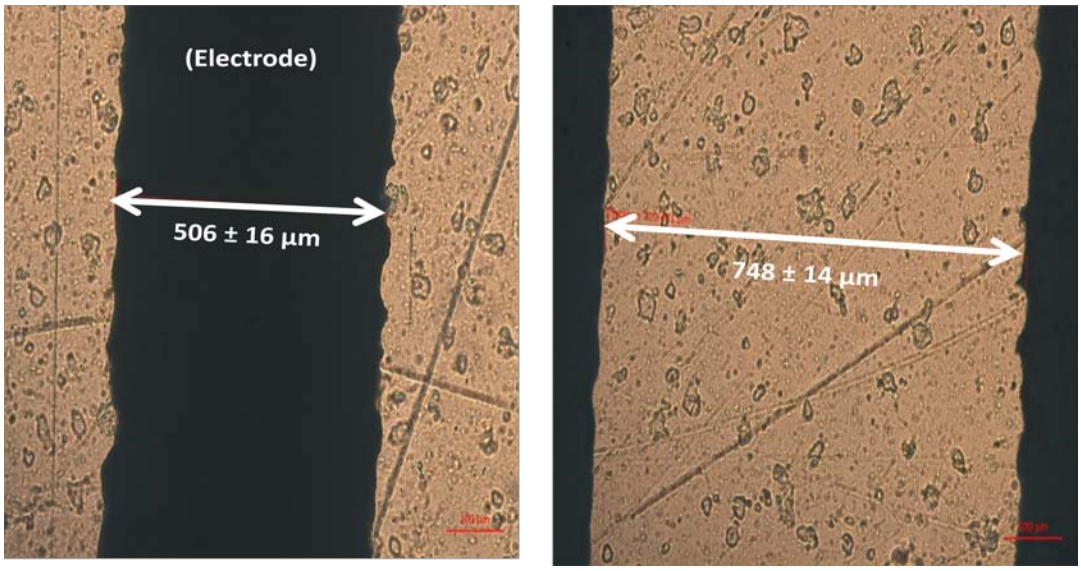

Figure 3.12: Optical microscope images of an IDE electrode (left) and an IDE electrode gap (right)

3.4 Calculation of g_{33} Coefficient

The piezoelectric characteristics that have been focused on in this study refer to a PZT fiber's electromechanical behavior as an actuator through the converse piezoelectric effect. For both e_{33} and d_{33} testing, external electric fields were applied and stresses and strains were measured. However, active fiber composites, as discussed in Section 1.1, are also used as sensors. This means that it is important to also characterize PZT's piezoelectric sensing coefficients. Similarly to how the converse effect is commonly characterized by the induced mechanical stresses and strains, the direct effect is commonly characterized by induced electrical charges and voltages. Due to thermodynamic considerations [26], the piezoelectric strain coefficient, d_{33}, is the same for the converse and direct effect. It was found to be 166 pC/N in an IDE setup.

Another commonly used sensing piezoelectric coefficient is the g_{33} coefficient, also known as a voltage coefficient. This coefficient is defined in the strain-voltage form of the piezoelectric constitutive equations. The strain-voltage equations are:

$$S_3 = {s_3}^D T_3 + g_{33} D_3 \tag{3.6}$$

$$E_3 = -g_{33}T_3 + \beta_3{}^T D_3 \tag{3.7}$$

However, a relationship exists between the *d* coefficient, the *g* coefficient, and the material's permittivity, *ε*. When a piezoelectric material is open-circuited, charge starts to build on the surface, generating an electric field across the material, much like a capacitor. Under these conditions it can be seen that the electric field is a function of the *g* coefficient and stress, where the *g* coefficient can be defined by the strain coefficient and the material's absolute dielectric permittivity [26]. This relationship is shown in Equation (3.8).

$$g_{33} = \frac{d_{33}}{\varepsilon_3} \tag{3.8}$$

Using this relationship, the g_{33} coefficient of the PZT fibers can be calculated using experimentally determined values. The d_{33} value that was applied to this equation was 166 pm/V, the value experimentally determined in this study. The permittivity value applied was extracted from the experimentation performed by Wyckoff [16]. In his study, he experimentally determined that the PZT fibers in an IDE setup exhibited a relative permittivity of about 830 ± 100. As discussed in Section 1.3 and shown in Equation (1.6), a material's relative permittivity is defined as its dielectric permittivity divided by the permittivity of free space, ε_o. Therefore, the dielectric permittivity for PZT fibers is about 7.35 ± 88 nF/m. By applying experimentally determined values for PZT fibers in an IDE setup, the g_{33} coefficient for a PZT fiber in an IDE setup is predicted to be 22.6e-3 ± 2.5e-3 Vm/N.

The predicted voltage coefficient for PZT fibers in an IDE assembly is interestingly close to the voltage coefficient reported for bulk PZT. As bulk PZT's coefficient value is published as 24.8e-3 Vm/N [31], the experimentally predicted value for PZT fibers is roughly 90% of bulk material. This experimental result contradicts the general assumption that all PZT fiber electromechanical property values are 65 – 75% of

bulk PZT's properties [12]. However, applying this assumption to Equation (3.6) generates an interesting hypothesis. If a PZT fiber's induced strain coefficient and its permittivity are both reduced by 65 – 75% due to factors present in the manufacturing processes, then according to Equation (3.8), the voltage g_{33} coefficient would remain unchanged. The experimental characterization of PZT fiber properties seems to support this idea that the g_{33} sensing coefficient of a fiber is nearly identical with that of the bulk PZT value.

In this chapter, experimental processes and improvements for characterizing PZT fiber e_{33} and d_{33} coefficients were outlined and explained. Additionally, a fiber's potential g_{33} coefficient response between IDEs was calculated based on experimental d_{33} and permittivity values. The experimental process improvements implemented into e_{33} testing produced coefficient values more similar to FEA model predicted values for both parallel electrode and IDE testing configurations. Experimental results for a fiber's d_{33} coefficient between IDEs show significant deviation from the published bulk material coefficient value. However, the validity of this value deviation cannot be verified due to a lack of published data for a PZT fiber's d_{33} response between IDEs. Therefore, FEA models were created to help verify the experimental d_{33} coefficient obtained in this study, and these models are outlined in the next chapter.

Chapter 4
FEA Modeling of PZT Fibers

In this chapter, finite element analysis (FEA) models are developed to verify the experimental data gathered for the induced strain coefficient (d_{33}) study of individual PZT fibers. Due to a lack of literature on the d_{33} response of individual fibers, these models were created to obtain values with which to compare the experimental response values, similar to the e_{33} models created in a previous study [16]. Details of model setup, verification, and resulting tabulated d_{33} values are discussed in the following sections.

4.1 Modeling a Fiber using Two Electrode Configurations: Parallel and IDE

4.1.1 Parallel Electrode Fiber Model

The first FEA model created in this study was a model representing a PZT fiber in a parallel electrode setup. Experimentally, testing a fiber in a parallel electrode setup was not feasible with the fiber-optic sensor equipment used in this study. In a parallel electrode setup, the electrodes are located at the tips of the fibers. Since the fiber-optic sensor tracks the motion of the fiber's tip, the electrode itself along with the electrical leads supplying the voltage would need to move simultaneously with the fiber. Due to their small-scale size and highly brittle nature, applying a parallel electrode of this nature was deemed too challenging for the style of testing performed in this study. Additionally, the DMA setup used for e_{33} testing could not be utilized for parallel or IDE d_{33} testing because the very small deformations of the fiber at low electric fields would not be accurately captured by the DMA. Therefore, a computer model was developed to predict the induced strain behavior of a fiber in a parallel electrode setup for comparison with published values for bulk PZT.

A 3D simulation software package called ABAQUS/ CAE [37] was used due to the convenience of applying piezoelectric material properties and modeling electromechanical behaviors as well as its availability. To begin, a 3D geometric model was generated, which consisted of a single, short section of a PZT fiber. The parameters

necessary as inputs to the model were the PZT fiber's material properties and the boundary conditions that best describe d_{33} testing. The fiber was modeled with a length of 750 μm and with a 250 μm cross-sectional diameter.

In ABAQUS, a PZT material for the fiber was created by programming in the fiber's mechanical elasticity, dielectric permittivity, density, and predicted piezoelectric behaviors. The density was input as a single, uniform value, whereas the elasticity, permittivity, and predicted piezoelectric properties were each input as a property matrix. The PZT properties used were extracted from the experimentation results of a PZT fiber in a parallel electrode setup presented by Wyckoff [16], and each property value/matrix can be found in Appendix C. Most significantly, the piezoelectric strain behavior properties used in the model were estimated as 70% of bulk PZT's properties as a first "guess" of fiber behavior. The resulting d_{33} coefficient predicted by the model will be compared to the estimated 70% "guess" in order to determine the validity of the initial property value programmed into the model.

Once the geometry of the fiber, shown in Figure 4.1, was created and the PZT material properties programmed into the model were applied to the fiber geometry, boundary conditions were placed on the fiber. Table 4.1 provides the values of the boundary conditions applied in this model. A fully constrained mechanical boundary condition was applied to one end of the fiber (Face A), constraining it from motion along the direction of its length (z-direction). The other end (Face B) was left unrestricted along the z-direction, which would allow the fiber to expand under an applied electric field load. Pairing the mechanical boundary conditions at Faces A and B together created the free strain boundary condition used to obtain Equation (3.4). Next, the parallel electrode setup was applied by utilizing two electric potential boundary conditions on the ends of the fiber. On Face A, a positive electric potential condition was applied, and on Face B, a ground (zero) electric potential condition was applied. Pairing the two electric potential boundary conditions produced a low electric field of 0.1 MV/m in the fiber.

Table 4.1: Boundary conditions applied to the parallel electrode model

Boundary Condition	Applied To	Value
Fully Constrained	Face A	x=y=z=0 mm
Positive Electric Potential	Face A	75 V
Ground Electric Potential	Face B	0 V

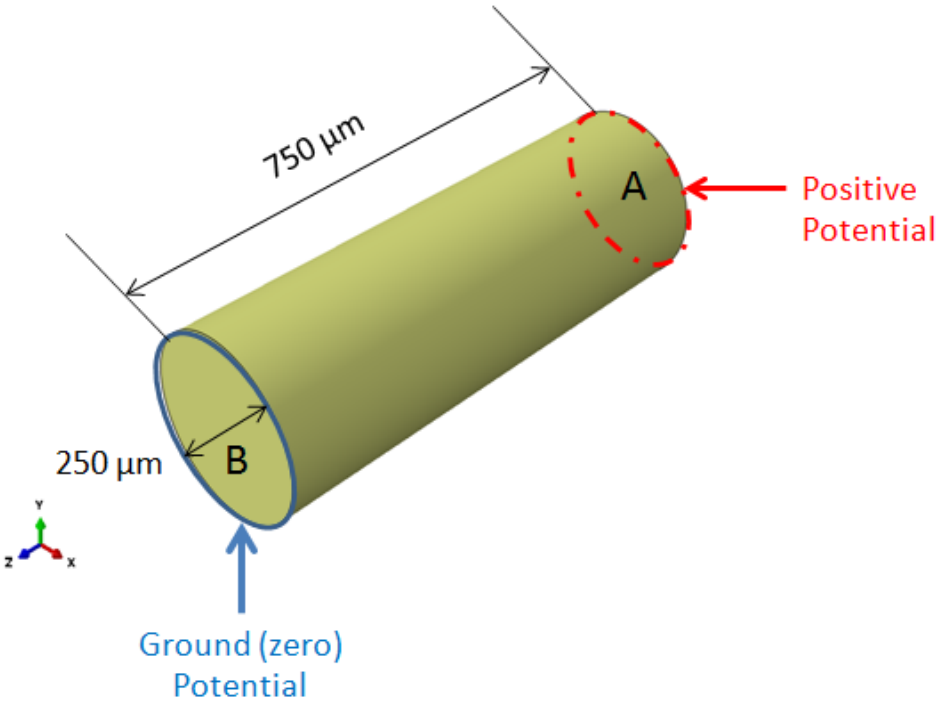

Figure 4.1: Parallel electrode fiber FEA model

A mesh of the default hex elements with a global seed size of 3.5e-5 was applied to the fiber. Hex elements allowed for faster computing times (about 10 seconds), and due to the relatively simple geometry of the model, tetrahedral elements were not necessary. The element types were then changed from the default "3D stress deformable" elements to linear piezoelectric elements. This change was essential to allow the fiber to utilize the piezoelectric properties defined in the material properties. For analysis, a low electric field of strength 0.1 MV/m was applied to the PZT fiber in order to extract the resulting d_{33} coefficient of the fiber. To do this, the positive electric potential boundary condition was set to a voltage value of 75V, which over a testing length of 750 µm, corresponds to a 0.1 MV/m field. The elongation induced in the fiber from the application of the electric field was extracted from the model using the

displacements of the mesh elements calculated by the model. Then, the strain in the fiber was calculated by dividing the total elongation by the initial length of the fiber. Lastly, the induced strain coefficient of the fiber was calculated by dividing the strain by the applied 0.1 MV/m field using Equation (3.4). As a result, the FEA model of a fiber in parallel electrodes generated a d_{33} coefficient of about 257 pm/V. An image of the displacements calculated in the fiber can be seen in Figure 4.2.

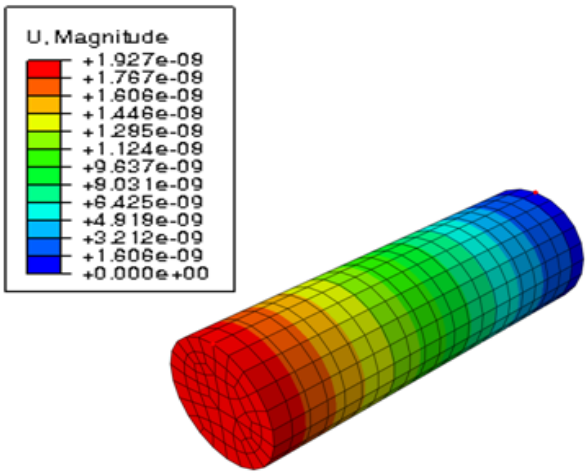

Figure 4.2: Displacements (shown in meters) of the meshed elements in the parallel electrode setup

The d_{33} coefficient value reported for bulk PZT is 374 pm/V [31]. The d_{33} coefficient calculated with the parallel electrode setup model was consequently about 69% of the reported bulk material value. This indicates that the initial assumption that the PZT induced strain fiber properties are about 70% of those of bulk PZT is a valid one.

4.1.2 IDE Fiber Model

Since the d_{33} experiments performed in this study were done using a fiber in an IDE assembly, it was necessary to create an FEA model using an IDE setup. Although the experimental testing assembly was comprised of the fiber, silver electrodes printed onto Mylar sheets, acrylic plates, and plastic nuts and bolts, only the electrodes and fiber were modeled in ABAQUS. The other elements excluded did not play a role in the electromechanical behavior of the fiber. For modeling simplification, a single part was

created with different partitions acting as the different materials in the model. Additionally, to decrease model complexity and drastically reduce computational time, a representative volume element (RVE) was used. In the experimental IDE setup used in this study, there were 24 electrode gaps, which their lengths in summation were taken as the active area of the fiber during testing. However, due to symmetry, the fiber in the IDE assembly behaves equally in magnitude electromechanically in each of the 24 electrode gaps; so, a single IDE gap was modeled as the RVE.

To begin, a solid rectangular prism with a cross-section with dimensions 500 μm x 270 μm was extruded to a length of 1250 μm. Next, a circular partition of diameter 250 μm was created through the center of the prism to act as the fiber. Then, four more rectangular partitions with 250 μm lengths were formed for the electrodes of the IDE: two positive and two ground electrodes. This left a 750 μm gap between the electrodes. A cross-sectional view of the RVE can be seen in Figure 4.3.

After partitioning the necessary elements of the model, three materials were defined. The first was the PZT fiber material, which utilized the same material properties as those applied to the PZT fiber in the parallel electrode model. The second material was a silver material applied to the electrodes. Lastly, a vacuum material was created and applied to the remaining areas of the initial prism. Since the RVE was created by partitioning out sections from a single element to start, having these “vacuum” portions prevented errors in the model, so ABAQUS would run the analysis. The material property values/matrices applied to the PZT fiber were identical to those used in the parallel model. Again, these fiber properties, as well as the material properties used for the silver electrodes, can be found in Appendix C.

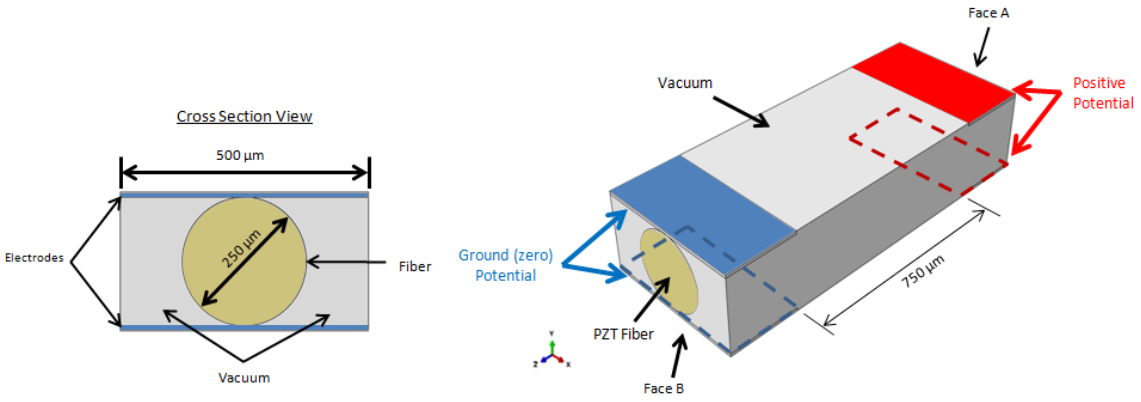

Figure 4.3: IDE RVE: Red areas act as the positive electrodes and blue as the ground electrodes. Dashed outlines indicate electrodes on the bottom of the RVE

After the three different materials were applied to their respective sections of the RVE, boundary conditions were applied. Table 4.2 provides the values of these boundary conditions. Mechanically, two conditions were applied. First, the exterior electrode surfaces (top and bottom) were constrained in the y-direction. Second, Face A was fully constrained. Face B was able to freely move along the z-axis when an electric field load was applied. The combination of the mechanical boundary conditions at Faces A and B created the free strain environment along the fiber's length needed to use Equation (3.4) for d_{33} calculations. In order to generate the electric field, electric potential boundary conditions were applied to the electrodes. The two electrodes near Face A (red faces) were given a positive electric potential condition, and the other two electrodes (blue faces) were given a ground (zero) electric potential condition. The combination of these electric potential boundary conditions created a low electric field of strength 0.1 MV/m through the fiber's length.

Table 4.2: Boundary conditions applied to the IDE model

Boundary Condition	Applied To	Value
Vertical Constraint	Top and Bottom Surfaces	y=0 mm
Fully Constrained	Face A	x=y=z=0 mm
Positive Electric Potential	Red Faces	75 V
Ground Electric Potential	Blue Faces	0 V

Due to the greater geometric complexity of this configuration, the model is more involved than the parallel electrode one; therefore, the mesh had to be created using tetrahedral elements. This is because the combination of rounded and square interfaces within the model's geometry could not be accurately modeled using hexagonal mesh elements. The tetragonal elements were changed from the default "3D stress deformable" type to a linear piezoelectric element type. In order to determine the d_{33} coefficient of the PZT fiber in an IDE assembly, it was first necessary to determine the extension of the fiber. This, however, was not as straightforward as it was for the parallel electrode fiber model. Only the elongations of the mesh elements of the fiber in the testing section (within the electrode gap) were desired.

A mesh sensitivity study was done to ensure that an accurate value for fiber extension within the testing gap was recorded. The importance of a mesh sensitivity study is that there is a trade-off between mesh size, accuracy of results, and computational time. Fewer and larger elements require much less computational time, but can result in overshooting the value for the testing section elongation. Conversely, meshes with a greater number of smaller elements require much longer computational times but yield more accurate results. Therefore, the d_{33} analysis of the IDE model would be run with various meshes to ensure proper coefficient characterization. A progression of mesh refinement can be seen in Figure 4.4. In this image, the seed size numbers refer to the rough length of each element's edges assigned by ABAQUS.

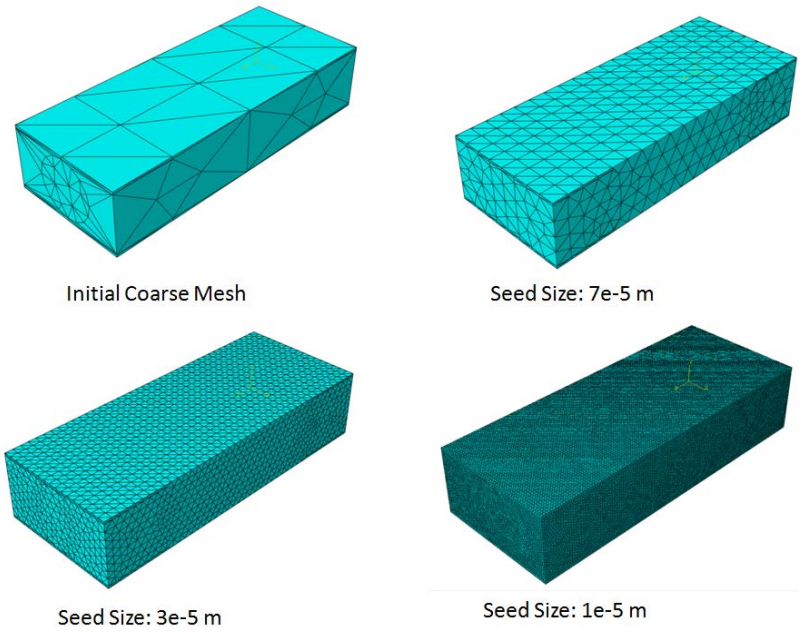

Figure 4.4: Mesh refining for IDE RVE

To begin, a coarse mesh was automatically applied by the software. The positive electric potential boundary condition on the positive electrodes was given a value of 75V, which corresponded with a 0.1 MV/m electric field when applied across the 750 μm testing gap. The elongation of the fiber between the electrodes was extracted from the model and was transformed into strain by dividing by the original testing gap length. Lastly, using Equation (3.4), this strain value was divided by the applied 0.1 MV/m electric field to obtain the d_{33} coefficient value. For this mesh, the calculated induced strain coefficient for the PZT fiber was about 234 pm/V. This result was very close to the parallel electrode fiber model value of 256 pm/V. The global seed size was reduced multiple times and tested at each reduced seed size. Each seed size reduction resulted in an increase in the number of elements in the mesh. For each mesh, the total number of elements and the number of warning elements were recorded as well as the d_{33} values extracted from the model. A table with these values with their corresponding seed size is shown in Table 4.3.

Table 4.3: Mesh refinement data

Global Seed Size	No. of Elem.	Warning Elem.	Warning %	d_{33} (pm/V)
.0005	2167	310	14.3%	234.3
.0003	2917	369	12.7%	204.0
.0002	3119	348	11.2%	197.3
.0001	4949	631	12.8%	195.7
.00007	5249	566	10.8%	193.3
.00005	14226	261	1.83%	188.0
.00004	22545	226	1%	186.7
.00003	42891	368	.86%	186.4
.00002	136662	645	.47%	185.2
.00001	822405	1625	.2%	184.9

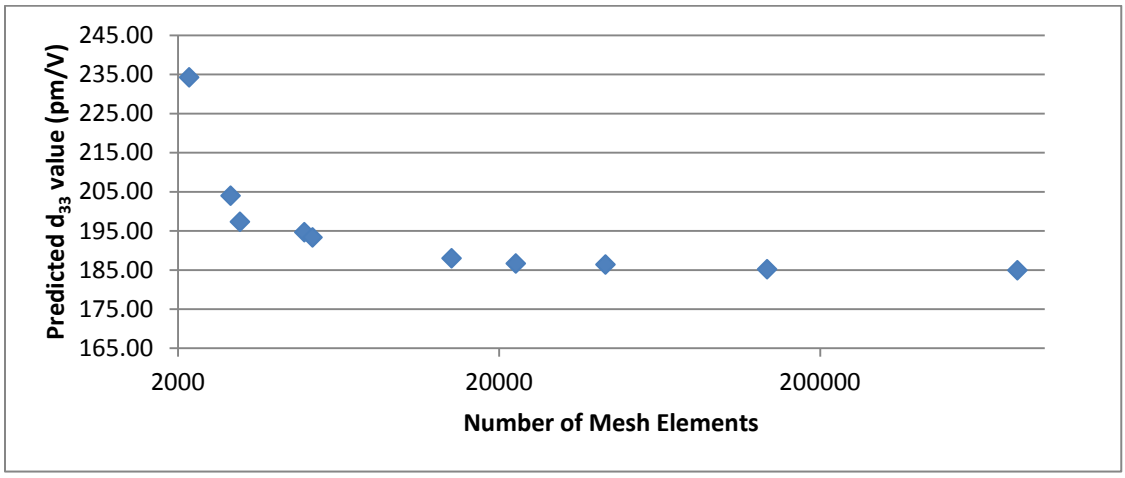

Figure 4.5: Predicted d_{33} values in relation to mesh refinements: d_{33} values settle at around 100000 mesh elements

As can be seen from the data in Table 4.3, the final seed size reduction produced six times more elements, but the resulting reported d_{33} value showed no significant change. This can also be seen in Figure 4.5 where the predicted induced strain coefficient horizontally asymptotes. After about 100,000 mesh elements, the d_{33} response in the fiber plateaus to a value of about 185 pm/V; further refining the mesh beyond this number of elements greatly increase the computational time without producing an appreciable change in the d_{33}. For example, the final refined mesh took about 10 minutes

to complete whereas the previous refined mesh (136662 elements) took about 1.5 minutes to run. So, the model predicted d_{33} coefficient for a PZT fiber in an IDE assembly is 185 pm/V.

4.2 Comparisons

4.2.1 Comparison of Parallel Model to IDE Model Results

As expected, the parallel electrode fiber model and the IDE fiber model generated two different d_{33} coefficients. The IDE fiber model value of 185 pm/V is about 72% in value of the parallel electrode fiber model. This reduction in value for the IDE model can be attributed to the electric field differences in the models. In the parallel model, the electric field that passes through the PZT fiber is uniform throughout the fiber whereas the electric field in the IDE model is very non-uniform through the fiber, as discussed in Section 1.1 and shown in Figure 4.6. The net electric field produced by the IDEs is directed along the fiber's length, but its magnitude is lower than that of the same field applied in a parallel electrode setup.

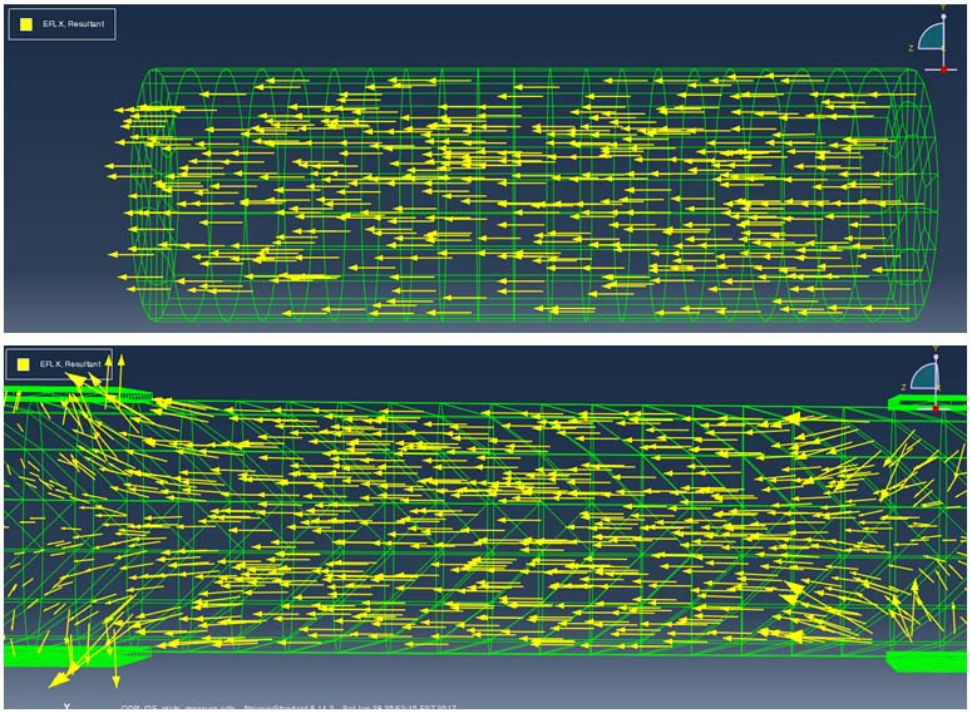

Figure 4.6: Electric field lines in the parallel electrode model (top) and IDE model (bottom)

Figure 4.6 shows the differences in the resulting electric field lines between the parallel electrode model and the IDE model. In the IDE model, the magnitude of the net electric field along the fiber's length can be altered and maximized by changing the electrode gap or changing the sample's thickness, which was studied by Hagood *et al*. [7].

The IDE design that was used for this study has an electrode gap to sample thickness (p/h) ratio of 5. According to Figure 1.10, a "p/h" ratio of 5 produces a relative strain of about -1.6. This means that the IDE design used in this study theoretically should produce a d_{33} coefficient in a material that is 1.6 times larger than the d_{31} coefficient for that material between parallel electrodes. Bulk PZT between parallel electrodes normally has a relative strain -2.19 which can be found by:

$$\frac{d_{33}}{d_{31}} = \frac{374\ pm/V}{-171\ pm/V} = -2.19 \tag{4.1}$$

Since the IDE design used would theoretically produce a relative strain of only -1.6, then it can be expected that the resulting d_{33} coefficient produced by in the IDE setup would be about 73% of the parallel electrode value (-1.6/-2.19).

Taking another look at the induced strain coefficients produced by the parallel and IDE FEA models, the IDE model produced a value of 185 pm/V, which is roughly 72% in value of the parallel electrode model value of 256 pm/V. This result aligns with the expectations of the IDE geometry used in this study, validating the obtained d_{33} coefficients from the FEA models in relation to one another.

4.2.2 Comparison of IDE d_{33} Experimental to Model Values

As mentioned previously, the induced strain coefficient of an individual PZT fiber in an IDE assembly determined through experimental means was about 166 pm/V. This value deviates from the 185 pm/V model predicted value. This deviation can be

attributed to various factors in the experimental process explained in Section 3.3 as well as factors in the models.

For the models, differences between the experimental and FEA values for d_{33} could be attributed to the material properties programmed into the FEA model. Some of the elastic and permittivity properties were experimentally obtained values that were extracted from the study done by Wyckoff [16]. The remaining values, including all of the strain matrix values, were estimated from the properties of bulk PZT. Since the properties used were nearly all estimations, they may not be accurately representative of the properties of a typical PZT fiber.

Additionally, the models were created and run as linear models since linear models are relatively simple to create, and only very low electric fields were applied to the fibers. In actuality though, PZT fibers exhibit non-linear piezoelectric behaviors. Lastly, when applying the piezoelectric strain properties to the fibers in the models, the direction of these properties were assumed to be uniform in both cases. For the parallel electrode case, this assumption is valid since the electric field applied is uniform. In an IDE, however, the poled dipoles are not uniaxially aligned, so the strain properties are not actually equal in magnitude and direction throughout the fiber. These factors, in combination with the potential experimental errors, could be the cause of the deviation in experimental and model recorded d_{33} values.

In this chapter, the development of the FEA models used for experimental verification was outlined. The predicted d_{33} responses of fibers between parallel electrodes and IDEs are presented, and the IDE-predicted result is compared to the parallel electrode-predicted value using expectations based on the geometry of the IDEs used in this study. Lastly, the IDE-predicted coefficient is compared to the experimentally-obtained d_{33} coefficient of a PZT fiber. The next chapter summarizes the results of this thesis study and provides recommendations for future work with the PZT fibers being studied here.

Chapter 5
Conclusions and Recommended Future Work

5.1 Summary of Work

Originally designed to improve structural health monitoring of systems, AFCs can also be used in an array of other applications as sensors and actuators since they exhibit both the direct and converse piezoelectric effects. A typical AFC manufactured today utilizes 250 μm diameter PZT fibers as the active piezoelectric material that is embedded in a protective epoxy matrix. Since their development, many studies have been performed on AFCs in order to optimize their piezoelectric behavior. Different fiber geometries, epoxy materials, and even different electrodes have been tested. As a result, the fabrication of AFCs has become somewhat of a standardized process utilizing specific materials and electrode geometries. Specifically, AFCs currently utilize the IDE pattern because this electrode pattern allows for the application of the electric field through the length of the fiber, greatly enhancing its piezoelectric capabilities by taking advantage of the so-called 33-mode. However, despite all of the research done with AFCs studying the mechanical effects of different materials or the mechanical properties of the PZT fibers themselves, very little research has focused on characterizing the electromechanical behavior of individual PZT fibers. A major step in AFC optimization is studying fibers on an individual basis. With properly characterized properties, conclusions can be drawn as to whether or not AFCs can really be optimized any more than they already have. To the best of our knowledge, only one study done by a previous member of our research group, Nicholas Wyckoff [16], characterized individual fibers electromechanically while mimicking their behavior in an AFC. This research study focused on extending Wyckoff's research further to characterize additional piezoelectric properties of individual PZT 5A fibers in an environment that mimicked a typical AFC.

To begin, improvements to Wyckoff's induced stress experimental processes for both parallel electrode and IDE setups were introduced. In order to close the gap

between experimental and FEA model predicted e_{33} values for individual PZT fibers, several different testing parameters were studied for both the parallel electrode setup and the IDE setup. All induced stress coefficient testing was performed using the DMA in conjunction with the TRIOS software. Electric fields were applied to the fibers using a function generator and voltage amplifier combination. For parallel testing, specially fabricated electrodes were used in the DMA. For IDE testing, IDE assemblies composed of electrodes screen printed onto Mylar sheets and adhered to acrylic plates were fabricated and used. Voltage and force data were simultaneously collected in Labview using a DAQ, and the resulting e_{33} coefficients were extracted from the data. Each parameter change made to the experimental processes resulted in new sets of induced stress coefficients for the PZT fibers.

After incorporating several changes to the e_{33} experimentation processes, the focus turned to characterizing the induced strain (d_{33}) coefficient of the PZT fibers. Due to limitations of the experimental equipment used for this study, the d_{33} coefficient of a PZT fiber was only characterized in an IDE setup. Using a function generator and voltage amplifier combination, several AC electric fields of varying strengths were applied to the fiber. Fiber elongations and contractions were measured using a fiber-optic sensor. From the length change data, d_{33} coefficients were extracted for individual PZT fibers in an IDE setup. With no values in the literature with which to compare the experimental results, focus was turned to FEA modeling. Two models were generated to study the d_{33} coefficient of PZT fibers: (1) one with a parallel electrode setup and (2) one with an IDE setup. The models were run to help verify the findings from the d_{33} experiments.

5.2 Conclusions

In Wyckoff's study [16], an FEA model predicted the e_{33} value of a PZT fiber to be about 6 C/m^2 in a parallel electrode setup and about 4 Cm^2 in an IDE setup. However, the experimental e_{33} values were only about 2.5 C/m^2 in a parallel electrode setup and 1.5 C/m^2 in an IDE setup. In this current study, focus was on improving the experimental

conditions and techniques to obtain better e_{33} values. Focusing on parallel electrode experimentation, the first major change was altering the fiber poling boundary condition. Originally, Wyckoff applied a blocked stress condition, which kept the fiber from expanding during poling, reducing its remnant polarization after poling. After changing this boundary condition to a constant stress condition in this study, the fiber was able to expand during poling, and the resulting e_{33} coefficient exhibited a nonlinear behavior ranging in value from about 3.8 – 5.1 C/m^2 for electric field values from 0.1 – 1 MV/m. Using a modified Rayleigh law to model this nonlinear behavior, an initial value of 3.7 C/m^2 was extracted. Continuing the experimental improvement process, different testing parameter changes including boundary condition changes, load changes, and experimental setup changes were tested. As a result, the experimentally obtained value for the induced stress piezoelectric coefficient between parallel electrodes was 4.8 C/m^2. This value was only about 30% of the reported bulk material value of 15.4 C/m^2 [31]. However, the model predicted e_{33} value in a parallel electrode setup was 6 C/m^2 [16], so the measured parallel electrode e_{33} coefficient from this study was 80% of the model predicted value. After considering the changes made to the experimental process, it was surmised that the remaining deviation in values was likely caused by the pre-load in the fiber during testing. For the experimental equipment utilized, in order to keep the fiber in place between the electrodes, a pre-load stress was applied. This pre-load stress magnitude was eventually minimized, but it still caused a constant compressive strain in the fiber.

Since this pre-load strain was maintained as constant through each round of testing due to the blocked force boundary condition applied, it was essentially assumed to be negligent when using Equation (2.1) to calculate the e_{33} coefficient. However, this pre-strain could be skewing the resulting electromechanical behavior data by pushing the dipoles further out of alignment with the fiber's length, decreasing its piezoelectric response. Experiments set up to eliminate this pre-strain could help verify this hypothesis. A testing setup utilizing a horizontal fiber alignment on a flat surface between electrodes could eliminate the need for a compressive stress to hold the fiber in place. Another source of error could be a result of the significant difficulty of properly

installing a fiber into the testing assembly. Proper alignment involved installing the fiber in a perfectly vertical position between the electrodes. However, the size of the fibers used for testing as well as the larger size of the alignment indents on the electrodes made repeatable fiber alignment difficult. If the fiber is not perfectly aligned with the applied electric field, then the resulting e_{33} data gathered is not representative of the fiber's true '33' direction. An offset alignment would result in only the vertical components of stress being recorded instead of the total levels of stress being induced in the fiber. Lastly, the model predicted value extracted from Wyckoff's [16] study was used as a comparative value for the parallel e_{33} coefficient measured in this study. However, the parallel electrode FEA model created by Wyckoff carried a few general assumptions as described in Section 3.1.3. These assumptions could alter the true predicted response of the fibers, contributing to the difference between the experimental and predicted parallel e_{33} coefficient values.

Focusing now on the experimentation using the IDE setup, the first major experimental alteration made was again changing the poling boundary condition. The blocked stress condition was changed to a constant stress condition, which allowed fiber expansion during poling. This parameter change yielded e_{33} values ranging from 2.4 – 3.6 C/m^2 in electric fields applied from 0.1 – 1 MV/m. Again applying the modified Rayleigh law to model the nonlinear electromechanical behavior of the fiber, the resulting e_{33} value reported from the boundary condition change was 2.3 C/m^2. The next experimental procedure change made was a decrease in the testing gap. Originally, about 40% of the fiber in the 50 mm testing gap was unpoled. According to Wyckoff's research study [16], poled and unpoled PZT fibers exhibit differing mechanical properties. This conclusion lead to the conclusion that a significant portion of the upoled fiber in the testing section was skewing the true e_{33} results of the fiber. Therefore, the testing gap was reduced by 5mm, and the e_{33} value reported increased to 2.7 C/m^2.

In an effort to further reduce the amount of unpoled fiber found in the testing section, a new IDE design was created. This design utilized the same active electrode area as the original design, but reduced the inactive area by 5 mm. As a result, the

amount of unpoled fiber in the testing section was reduced to 25%. The experiments using this new IDE design yielded an induced stress coefficient of 3.5 C/m^2 for the PZT fiber. Again this value was well below the one reported for bulk PZT, making it less than 25% of the bulk value. However, the FEA model predicted e_{33} coefficient of a fiber in an IDE setup was 4 C/m^2, so the experimentally measured value from this study was about 90% of the predicted value. One source of error causing this experiment to model discrepancy is likely the remaining portion unpoled fiber in the testing section. Proven with the new IDE design, reducing the amount of unpoled fiber improved the recorded electromechanical behavior of the fiber. Similar to parallel electrode testing, another source of error could be from the significant challenges of fiber installation. For the IDE setup, however, installation difficulties occur twice during testing. The first occurs when the fiber is being inserted into the acrylic IDE assembly. Proper installation requires that the fiber not slide across the electrodes to avoid damaging either the fiber or the electrodes. Additionally, the nuts and bolts used to secure the fiber in the assembly need to be lightly applied to avoid crushing the fiber. The second installation challenge occurs when placing the fiber-IDE assembly into the DMA tensile grips. Completely vertical alignment was again difficult, but the much larger lengths of fiber being tested increase the probability that unwanted torsion and bending stresses were present in the fiber during testing. Lastly, similar to parallel electrode testing, the IDE FEA model created by Wyckoff [16] carried a few general assumptions as described in Section 3.2.3. These assumptions could be affecting the predicted response of a fiber between IDEs, contributing to the difference between experimental and predicted IDE e_{33} coefficient values.

After e_{33} testing, the focus was shifted to experimentally characterizing d_{33} coefficient of PZT fibers in an IDE setup. Testing with a fiber-optic sensor yielded d_{33} coefficient values ranging from 212 – 424 pm/V for applied electric fields of 0.1 – 1 MV/m. Similar to the e_{33} calculation procedure, a modified version of the Rayleigh law was applied to the d_{33} data gathered. The result was a reported induced strain coefficient value of 166 pm/V for a fiber in an IDE setup. This value was well below the value of 374 pm/V reported for bulk PZT. However, with no value reported in the literature on

d_{33} in an IDE configuation, d_{33} characterization efforts were turned to analytical modeling of the fiber. Two FEA models were developed to study the electromechanical strain behavior of PZT fibers. The first was a simple model that utilized a parallel electrode setup. Even though parallel electrode d_{33} experimentation was not performed, this model was created to compare the theoretical d_{33} behavior of PZT fibers in comparison with the bulk PZT reported value. The resulting induced strain coefficient determined with the parallel electrode model was 256 pm/V. This value is roughly 70% of the reported bulk PZT value, which aligns with the generally accepted assumption that PZT fibers have properties roughly 65-75% of those reported for bulk PZT. Furthermore, the simple parallel electrode fiber model was developed to help validate the results of the more complex IDE fiber model.

The electrode design of the IDEs used in this thesis should theoretically produce an electric field directionality of about 75% in comparison with parallel electrodes. This means that the IDE fiber FEA model generated should produce a resulting d_{33} coefficient that is roughly 75% in value of the parallel electrode d_{33} value. After developing and running the IDE fiber model in ABAQUS, a value of 185 pm/V was found for the induced strain coefficient of the fiber. This value is roughly 72% of the parallel model value, reinforcing the validity of the model. However, the experimental IDE d_{33} value and the model predicted value were 10% different from one another (the experimental value of 166 pm/V was 90% of the predicted value). This deviation is likely attributed to any alignment imperfections between the fiber, the reflective tape, and the fiber-optic probe. Dealing with such a small scale of actuation could easily result in a significant decrease in strain values recorded.

Similar to FEA models in Wyckoff's [16] study, some of the property values in the two FEA models in this study for d_{33} characterization were estimated values since testing has not been extensively performed on individual PZT fibers. These estimations they may not be accurately representative of the properties of a typical PZT fiber and could have caused error in the evaluated d_{33} coefficient of the PZT fiber. In order for these models to be more accurate, systematic characterization of individual PZT fiber

properties needs to be continued. Additionally, the d_{33} models were developed as linear models since only a very low electric field was applied; but, this linear assumption could affect predicted coefficient responses, contributing to the differences between the experimentally obtained and model predicted d_{33} values. Lastly, the piezoelectric strain properties applied to the fiber in both models were assumed to be uniform through the fiber. Although this assumption is valid for the parallel electrode model, the dipoles of a fiber in an IDE configuration are not uniaxially aligned since the initial poling electric field is non-uniform. This means that the strain properties applied to the fiber in the IDE model would not actually be equal in magnitude and direction throughout the fiber, potentially contributing to the difference in values.

As AFCs can be used as both sensors and actuators, it is important to characterize both the direct piezoelectric effect coefficients along with the converse piezoelectric effect coefficients of PZT in order to fully understand PZT's electromechanical behavior in an AFC. Since the direct effect and converse effect *d* coefficients are thermodynamically identical, the induced charge d_{33} coefficient of a PZT fiber in an IDE setup would likely be about 166 pC/N. Furthermore, the induced voltage coefficient of the fiber was extracted through a simple mathematical relationship between the *d* coefficient and the fiber's permittivity. The g_{33} coefficient calculated for a PZT fiber in an IDE setup was 22.5e-3 Vm/N, which was interestingly close to the reported bulk PZT value of 24.8e-3 Vm/N, which does not align with the assumption that all piezoelectric coefficients of a PZT fiber are roughly 65 – 75% of bulk PZT values. However, taking a look at the mathematical relationship used to calculate the g_{33} coefficient, if both the d_{33} coefficient and permittivity of the fiber are reduced by the same amount (70%), then the g_{33} coefficient would remain unchanged. Further testing could confirm or deny this prediction.

In an effort to help further optimize the design of AFCs, this thesis was focused on characterizing properties of PZT 5A fibers. Specifically, experiments were designed and carried out in order to try and obtain electromechanical behavior stress and strain coefficients of the fibers. Generally, the piezoelectric properties of PZT fibers are

assumed to be roughly 65 – 75% of the values reported for bulk PZT. Through the experiments performed in this study, however, it was found that the fiber properties do not all follow this trend. For example, the model predicted e_{33} value of a fiber from Wyckoff's study was about 40% of the bulk value where the model predicted d_{33} value for a fiber in this study was about 70% of the bulk value. Furthermore, the mathematically predicted g_{33} value of a PZT fiber was about 90% of the bulk material value published. The goal that inspired this study is that systematic characterization of individual PZT fiber properties will lead to the design of better AFCs, driving their optimization progression onward. The results discussed thus far are a big step towards realizing that goal.

5.3 Suggested Future Work

In general, this study resulted in better piezoelectric coefficients for individual fibers as a result of improvements introduced to the experimental measurement techniques. Further improvement could also be made to the experimental processes used to determine the e_{33} and d_{33} coefficients of individual PZT fibers such as proper fiber alignment, which was a large issue in all of the experiments performed for this study mostly due to the fact that all fiber installation and alignment were performed manually. If experimentation is to be continued on studying the e_{33} coefficients, a way to achieve a more perfect alignment consistently for both parallel and IDE tests is recommended to help eliminate this factor. For d_{33} experimentation, proper co-axial alignment of the fiber and the probe could improve the coefficient values obtained. Additionally, the d_{33} experiments done in this study were only performed using an IDE configuration due to limitations of the testing equipment. It was not feasible to place a fiber between parallel electrodes while measuring elongations with the fiber-optic sensor setup used. Furthermore, the DMA setup could not be used because small deformations at very low electric fields would not be accurately captured by the DMA. For full property characterization, however, it is suggested that d_{33} tests also be performed in a parallel electrode setup to help further validate the parallel electrode FEA fiber model. This could be done by finding a way to properly apply a mobile parallel electrode and utilizing the same fiber-optic setup. Parallel electrode d_{33} testing could also possibly be done by

studying the changes in the fiber's length while observing the entire length of the fiber rather than measure distances from the fiber's tip.

Additional research should be done on characterizing other properties of individual PZT fibers, especially the piezoelectric sensing coefficient, g_{33}. The g_{33} coefficient determined in this study, which was calculated, showed an interesting and unexpected result. Although the actuation coefficients of PZT fibers decrease in value from bulk PZT, the sensing coefficient seemed to remain similar. Experimental determination of the g_{33} coefficient of a fiber would shed some light on this unexpected finding. Similarly to the e_{33} and d_{33} studies, since there is no experimental data to compare g_{33} results to, FEA models would need to be developed to help validate the data obtained through experimentation.

Further fiber property characterization could also help improve the FEA models of the individual fibers. Many of the material properties input into the model are estimated property values from bulk PZT. Since AFC can and do vary in design, full PZT fiber material property characterization would allow for more accurate models of AFCs for whatever application design is desired.

References

[1] T. Takagi, "A Concept of Intelligent Materials," *Journal of Intelligent Material Systems and Structures,* vol. I, pp. 149-156, April 1990.

[2] N. W. Hagood and A. A. Bent, "Development of Piezoelectric Fiber Composites for Structural Actuation," in *34th AIAA Structures, Structural Dynamics, and Materials Conference*, La Jolla, pp. 3625-3638, 1993.

[3] A. A. Bent and N. W. Hagood, "Piezoelectric Fiber Composites with Interdigitated Electrodes," *Journal of Intelligent Material Systems and Structures,* vol. VIII, pp. 903-919, 1997.

[4] H. Atitallah, "Characterization and Modeling of Active Fiber Composites," 2015.

[5] N. W. Hagood, C. von Flotow and A. von Flotow, "Modelling of Piezoelectric Actuator Dynamics for Active Structural Control," *Journal of Intelligent Material Systems and Structures,* vol. I, pp. 327-354, 1990.

[6] E. F. Crawley and J. de Luis, "Use of Piezoelectric Actuators as Elements of Intelligent Structures," *AIAA Journal*, vol. 25, pp. 1373-1385, 1987.

[7] N. Hagood, R. Kindel and K. Ghandi, "Improving Transverse Actuation of Piezoceramics using Interdigitated Surface Electrodes," in *SPIE*, pp. 341-352, 1993.

[8] G. A. Rossetti, A. Pizzochero and A. A. Bent, "Recent Advances in Active Fiber Composites Technology," in *12th IEEE International Symposium on Applications of Ferroelectrics*, pp. 753-756, 2000.

[9] A. A. Bent and N. W. Hagood, "Improved performance of piezoelectric fiber composites using interdigitated electrodes," in *SPIE - The International Society for Optical Engineering*, pp. 196-212, 1995.

[10] R. Gentilman, K. McNeal and G. Schmidt, "Enhanced performance active fiber composites," in *SPIE - The International Society for Optical Engineering*, pp. 350-359, 2003.

[11] X. Kornmann and C. Huber, "Microstructure and mechanical properties of PZT fibres," *Journal of the European Ceramic Society,* vol. 24, pp. 1987-1991, 2004.

[12] F. M. Guillot, H. W. Beckham and J. Leisen, "Hollow Piezoelectric Ceramic Fibers for Energy Harvesting Fabrics," *Journal of Engineered Fibers an Fabrics,* vol. VIII, no. 1, pp. 75-81, 2013.

[13] R. Dittmer, F. Clemens, A. Schoenecker, U. Scheithauer, M. Rojas-Ismael and T. Graule, "Microstructural Analysis a nd Mechanical Properties of Pb(Zr,Ti)O3 Fibers Derived by Different Processing Routes," *Journal of the American Ceramic Society,* vol. 93, no. 8, pp. 2403-2410, 2010.

[14] L. J. Nelson, C. R. Bowen, R. Stevens, M. Cain and M. Stewart, "Modelling and measurement of piezoelectric fibres and interdigitated electrodes for the optimisation of piezofibre composites," in *SPIE - The International Society for Optical Engineering*, pp. 556-567, 2003.

[15] J. Heiber, A. Belloli, P. Ernmanni and F. Clemens, "Ferroelectric Characterization of Single PZT Fibers," *Journal of Intelligent Material Systems and Structures,* vol. 20, pp. 379-385, 2009.

[16] N. Wyckoff, "Systematic Characterization of PZT 5A Fibers with Parallel and Interdigitated Electrodes," M.S. thesis, Dept. Mech. Eng., The Pennsylvania State Univ., 2016.

[17] A. J. Brunner, M. Barbezat, C. Huber and P. H. Flueler, "The potential of active fiber composites made from piezoelectric fibers for actuating and sensing applications in structural health monitoring," *Materials and Structures,* vol. XXXVIII, pp. 561-567, 2005.

[18] A. J. Brunner, M. Birchmeier, M. M. Melnykowycz and M. Barbezat, "Piezoelectric Fiber Composites as Sensor Elements for Structural Health Monitoring and Adaptive Material Systems," *Journal of Intelligent Material Systems and Structures,* vol. XXII, pp. 1045-1055, 2009.

[19] X. Kornmann, C. Huber, M. Barbezat and A. J. Brunner, "Active Fiber Composites: Sensors and Actuators for Smart Composites & Structures," in *11th European Conference on Composite Materials*, No. B074, 2004.

[20] H. A. Sodano, G. Park and D. J. Inman, "An investigation into the performance of macro-fiber composites for sensing and structural vibration applications,"

Mechanical Systems and Signal Processing, vol. XVIII, pp. 683-697, 2004.

[21] A. Belloli, D. Niederberger, S. Pietrzko, M. Marart and P. Ermanni, "Structural Vibration Control via R-L Shunted Active Fiber Composites," *Journal of Intelligent Material Systems and Structures,* vol. 18, pp. 275-287, 2007.

[22] R. B. Williams, G. Park, D. J. Inman and W. K. Wilkie, "An Overview of Composite Actuators with Piezoelectric Fibers," in *IMAC XX*, pp. 421-427, 2002.

[23] A. A. Bent, N. W. Hagood and J. P. Rodgers, "Anisotropic Actuation with Piezoelectric Fiber Composites," *Journal of Intelligent Material Systems and Structures,* vol. 6, pp. 338-349, 1995.

[24] S. B. Kerur and A. Ghosh, "Active Vibration Control of Composite Plate Using AFC Actuator and PVDF Sensor," *International Journal of Structural Stability and Dynamics,* vol. 11, no. 2, pp. 237-255, 2011.

[25] R. Paradies and P. Ciresa, "Active wing design with integrated flight control using piezoelectric macro fiber composites," *Smart Materials and Structures,* vol. 18, no. 3, 2009.

[26] D. Damjanovic, "Ferroelectric, dielectric and piezoelectric properties of ferroelectric thin films and ceramics," *Reports on Progress in Physics,* vol. 61, pp. 1267-1324, 1998.

[27] S. R. Moheimani and A. J. Fleming, "Chapter 2 Fundamentals of Piezoelectricity," in *Piezoelectric Transducers for Vibration Control and Damping*, Springer Science & Business Media, 2006, pp. 9-35.

[28] E. Defay, Integration of Ferroelectric and Piezoelectric Thin Films, John Wiley & Sons, 2013.

[29] J. P. Rodgers, A. A. Bent and N. W. Hagood, "Characterization of interdigitated electrode piezoelectric fiber composites under high electrical and mechanical loading," in *SPIE*, pp. 642-659, 1996.

[30] A. Belloli, B. Castelli, X. Kornmann, C. Huber and P. Ermanni, "Modeling and Characterization of Active Fiber Composites," in *SPIE*, pp. 78-88, 2004.

[31] D. Berlincourt and H. H. A. Krueger, "Techncial Publication TP-226 Properties of

Piezoelectricity Ceramics," Morgan Electro Ceramics, Stourport-on-Severn, UK.

[32] E. Barabanova, O. Malyshkina, A. Ivanova, E. Posadova, K. Zaborovskiy and A. Daineko, "Effect of porosity on the electrical properties of PZT ceramics," *Functional materials and Nanotechnologies,* vol. 49, no. 1, 2013.

[33] TRIOS, "Software Downloads & Support," TA Instruments, [Online]. Available: http://www.tainstruments.com/support/software-downloads-support/downloads/#ffs-tabbed-11.

[34] LabVIEW, National Instruments, [Online]. Available: http://www.ni.com/labview/.

[35] IEEE Standard on Piezoelectricity. *ANSI/IEEE Std 176-1987*, IEEE, NY, 1988.

[36] D. Damjanovic and M. Demartin, "The Rayleigh law in piezoelectric ceramics," *Journal of Physics D: Applied Physis,* vol. 29, pp. 2057-2060, 1996.

[37] A. CAE, "Dassault Systemes," [Online]. Available: https://www.3ds.com/products-services/simulia/products/abaqus/abaquscae/.

Appendices

Appendix A

IDE Screen Printing Process

The electrode of the IDE assembly is created through a screen printing process. This process is performed using a Presco Thick Film Screen Printer, two screens with mirrored electrode patterns purchased from UTZ Technologies, a silver polycarbonate bus ink, Mylar sheets that are 0.1mm thick, and methanol for cleaning the screens and printer. An image of the screens purchased from UTZ technologies is shown in Figure A.1. The Presco screen printer, which can be seen in Figure A.2 uses compressed air to function. Compressed air raises and lowers the printing frame, moves the squeegee back and forth, and moves the sample stage under the printing pattern. An additional electric vacuum is used to create a vacuum zone on the sample stage that holds the sample in place while printing occurs. Two foot pedals are used to control the printing process. One pedal causes the printer to perform a single print, and the other pedal, when depressed, releases the vacuum so the substrate can be removed and another put in its spot. Outlined here are the major steps of the screen printing process.

Figure A.1: IDE printing screens

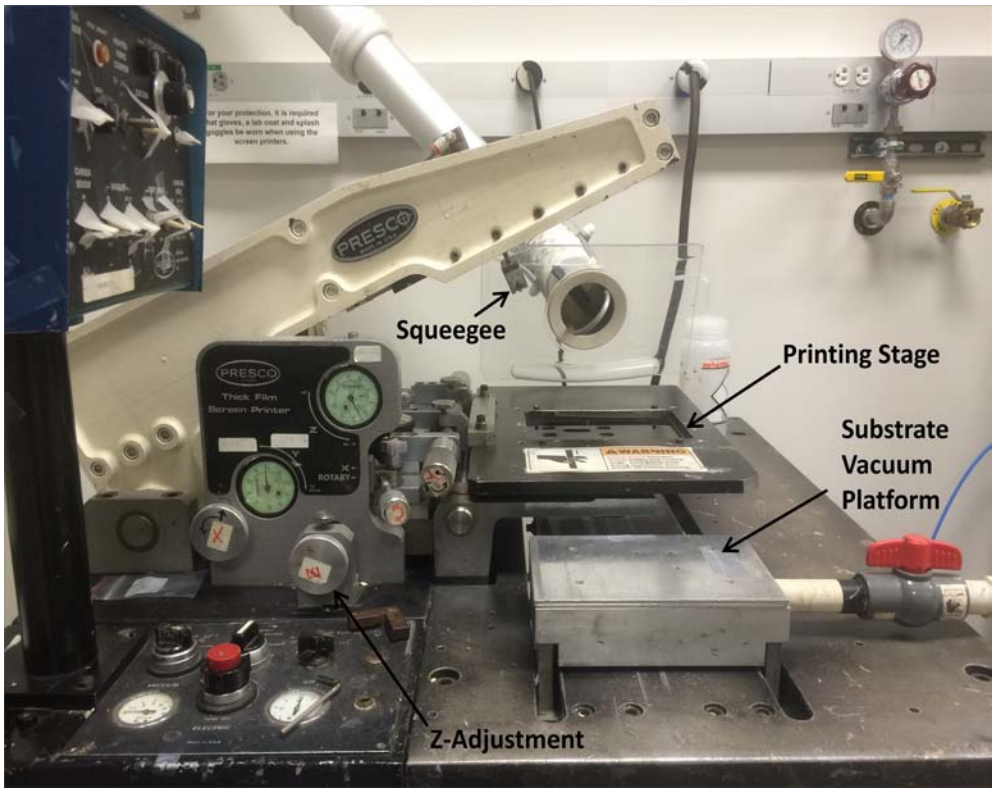

Figure A.2: Screen printer setup

Step 1: Screen setup

To begin, the screen with the desired IDE pattern that is to be printed is attached to the printing stage. This is done using four threaded allen head screws. The four holes in the corner of the screen's frame, shown in Figure A.3 are aligned with the holes passing through the printing stage. Four screws are passed through the printing stage and screwed into the screen frame, securing the screen in place. Next, the Z-adjustment knob is used to bring the bottom of the screen close enough to the substrate platform so that it almost touches the surface. From here, the Z-adjustment gauge is zeroed, and the knob is used to create a 0.3 mm gap. This gap between the bottom of the screen and the printing stage is necessary to allow the screen to immediately snap up off of the printing surface as the squeegee passes over the screen. Lastly, a Mylar substrate is placed onto the vacuum platform.

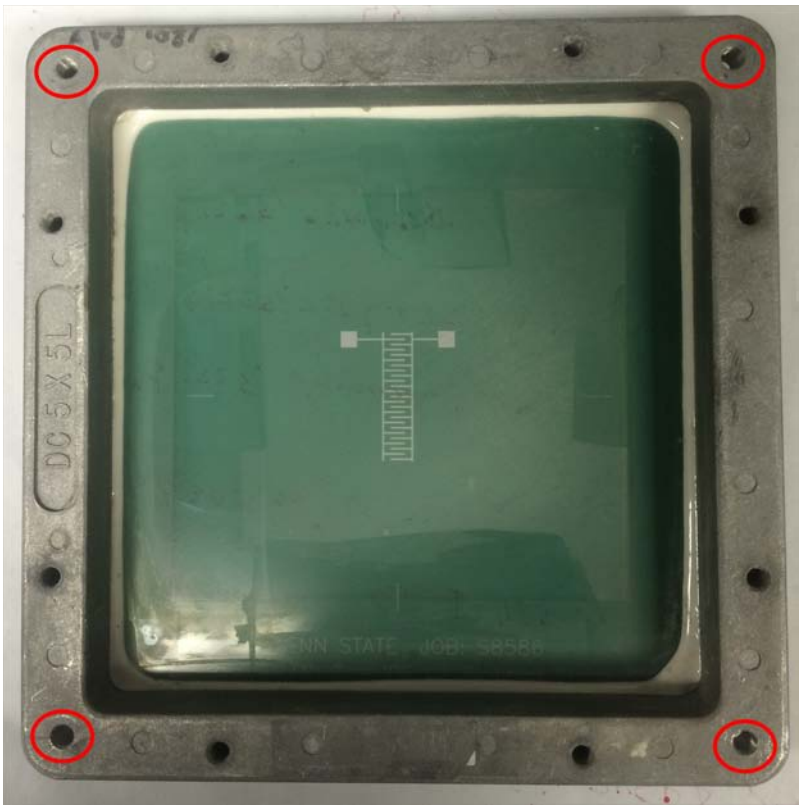

Figure A.3: IDE printing screen and frame

Step 2: Ink application and final adjustments

Once the screen is properly in place, the printing pressure from the squeegee needs to be determined. First, a line of the bus ink is placed on the screen between the squeegee and the pattern on the screen. Ink only needs to be placed in a width a little bit wider than the actual pattern. After the ink is in place, a print is run by depressing the printing pedal. If the print does not show on the Mylar substrate, the pressure of the squeegee is increase using the micrometer attached to it. The micrometer is turned one rotation and another print is done. This process is repeated until the first print appears. Lastly, the squeegee micrometer is turned two more rotations, and the setup is ready for printing.

Step 3: Printing and cleaning

For each print, a Mylar substrate is placed onto the vacuum platform. Once in place, and if there is ink still on the screen, the printing pedal is depressed and a print is

made. Then, the vacuum pedal is depressed releasing the Mylar sheet from the printing platform and another substrate is put in its place. This process continues either until the ink on the screen becomes too dry or thin to produce quality prints or when the number of desired prints is reached. If the ink becomes too thick (dry) or there is no longer enough to make a quality print, then the screen and squeegee must be cleaned before laying new ink down. For cleaning, two disposable lab towels are used. The methanol is sprayed onto the top of the screen and onto one of the disposable towels. The towel with the methanol is held under the screen while the other towel is used on top of the screen. Keeping the towels aligned, the screen is lightly scrubbed to remove the ink. Additionally, the squeegee is wiped off with the methanol towel. This process is done to avoid having clumps in the ink, which will ruin the print qualities. Once clean, new ink can be placed onto the screen and the printing process begins as before. When printing is finished, the same cleaning process is used to remove excess ink, the screen is removed from the printing stage, and the printer is shut down.

Appendix B

Fiber-Optic Sensor Calibration

For d_{33} testing of a PZT fiber in an IDE setup, an MTI-Instruments 2100 Fotonic Sensor fiber optic probe sensor was used to measure the length changes of the fiber. In order to properly measure these length changes, the sensor needs to be properly calibrated. When properly setup and calibrated, the fiber in the IDE assembly and the probe of the fiber-optic sensor will be co-axially aligned and extremely close to one another. To avoid any damage to the sensor probe, great care must be taken when making any position adjustments. Figure B.1 shows the calibrated alignment of a PZT fiber and the sensor probe. Figure B.2 shows the fiber-optic sensor used for this thesis study. Outlined here is the process used to setup and calibrate the d_{33} testing experiment.

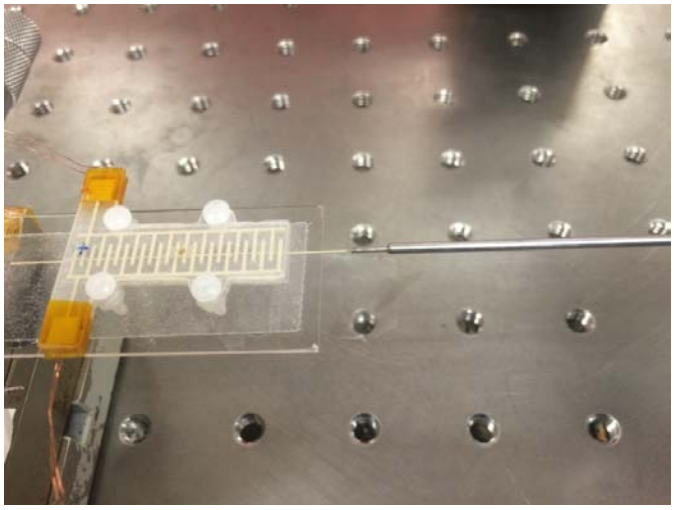

Figure B.1: PZT fiber in an IDE aligned with the fiber-optic sensor probe

Figure B.2: MTI-Instruments fiber-optic sensor

General alignment and calibration

Step 1:

The fiber-optic sensor is turned on and allowed to warm up for 30 minutes. Meanwhile, a fiber-IDE assembly that has already been poled and has a piece of reflective tape on the tip of the fiber is carefully adhered to a horizontal platform. At the same time, the sensor probe is vertically adjusted so that the fiber and the probe are co-axially aligned. After the 30 minute warm-up time, calibration and testing can begin.

Step 2:

The proper probe channel is selected on the sensor and the mode switch is moved to “CAL” to put the sensor into calibration mode.

Step 3:

When in the calibration mode, the fiber is moved closer to the tip of the sensor probe by using a micrometer built into the platform the IDE assembly is mounted on. The fiber is moved closer and closer to the probe until the maximum reading is achieved on the sensor display screen and the fiber (reflective tape) is almost touching the probe tip. This step should be done with the utmost care to avoid touching and potentially damaging the probe. The maximum reading must be located within 1% to avoid calibration error.

Step 4:

When the maximum value is found, the “CAL START” button is pressed and the sensor will automatically adjust the lamp in the probe to achieve a 10 volt reading.

Step 5:

The mode of the sensor changed from calibration to displacement. When this is done, the “over” light on the sensor should light up. The units should then be changed from volts to μm. At this point, two different ranges of operation can be chosen for use, as shown in Figure B.3. For the experiments carried out in this thesis, range 1 was desired. Range 1 is selected on the sensor and the fiber is moved closer to the probe until

the display screen reads a value of zero or close to zero. This zero value indicates that the gap is located in the center of range 1. Again, this step should be done with the utmost care to avoid damaging either the fiber or the sensor probe.

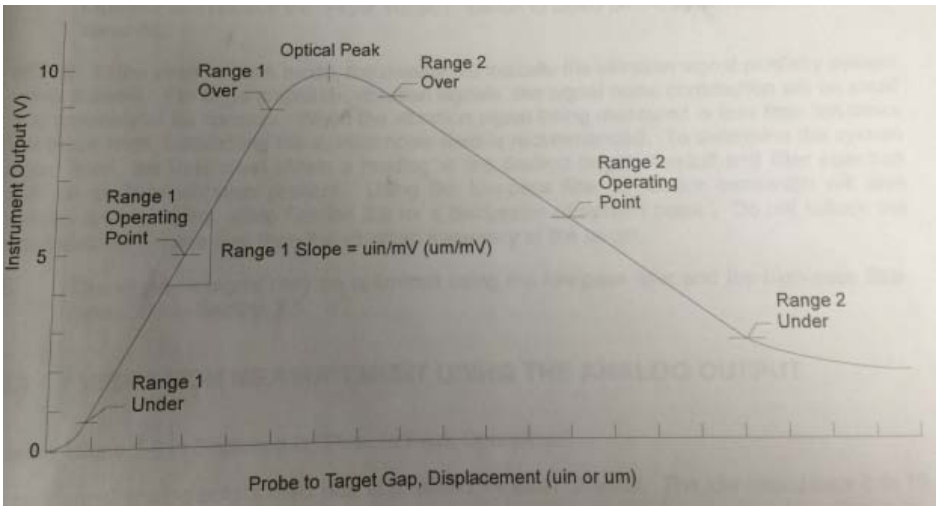

Figure B.3: Sensor calibration curve

High-resolution configuration

Due to the extremely small lengths of deformation induced in the fiber, the fiber-optic sensor has to be set into high-resolution mode following the calibration process. In order to do this, the "high gain" button on the sensor is selected, and the offset adjustment knob is rotated until the display screen reads a zero or near zero value. Lastly, the units are changed back to voltage units (mV) on the sensor for testing. Changes in voltage correlate to length changes of the fiber. These voltage units can be converted into length changes using the high-resolution conversion factor of 0.000052 μm/mV. The fiber-optic sensor is now setup and calibrated properly, and testing can commence.

Appendix C

Material Properties Programmed into ABAQUS Models

Table C.1: General material properties for ABAQUS models

Property	PZT Fiber	Electrode	Air
Density (kg/m3), ρ	7500	1070	1.225
Poisson's Ratio, ν	-	0.3	0
Elastic Modulus Y (Pa)	*Matrix 1*	3.00E+09	15
Permittivity, ε (F/m)	*Matrix 2*	3.32E-11	8.85E-12
Induced Piezoelectric Strain, d (m/V)	*Matrix 3*	*	*

** indicates a zero-matrix was applied*

Matrix 1: Stiffness matrix for a PZT 5A fiber

$$[c^E] = \begin{bmatrix} 6.7394 & 4.21 & 4.205 & 0 & 0 & 0 \\ 4.21 & 6.7394 & 4.205 & 0 & 0 & 0 \\ 4.205 & 4.205 & 6.2086 & 0 & 0 & 0 \\ 0 & 0 & 0 & 1.1789 & 0 & 0 \\ 0 & 0 & 0 & 0 & 1.1789 & 0 \\ 0 & 0 & 0 & 0 & 0 & 1.2641 \end{bmatrix} x10^{10}\ Pa$$

Matrix 2: Permittivity matrix for a PZT 5A fiber

$$[\varepsilon^T] = \begin{bmatrix} 10.04 & 0 & 0 \\ 0 & 10.04 & 0 \\ 0 & 0 & 9.868 \end{bmatrix} x10^{-9}\ F/m$$

Matrix 3: Induced piezoelectric strain matrix for a PZT 5A fiber

$$[d] = \begin{bmatrix} 0 & 0 & 0 & 0 & 4.09 & 0 \\ 0 & 0 & 0 & 4.09 & 0 & 0 \\ -1.2 & -1.2 & 2.62 & 0 & 0 & 0 \end{bmatrix} x10^{10}$$

Appendix D

Scanning Electron Microscopy Imaging of the PZT Fiber Tips

During the process of improving the performed e_{33} parallel electrode experiments, electrical contact between the brass electrodes and the fibers being tested was brought into question. Since the fibers were ceramic and brittle in nature, the process of cutting the fibers likely caused the fiber tips to partially fracture, leaving a rough surface profile. In order to see this rough profile, a scanning electron microscope was utilized. Examples of the resulting fiber fracture surface profiles from cutting can be seen in Figure D.1 (a).

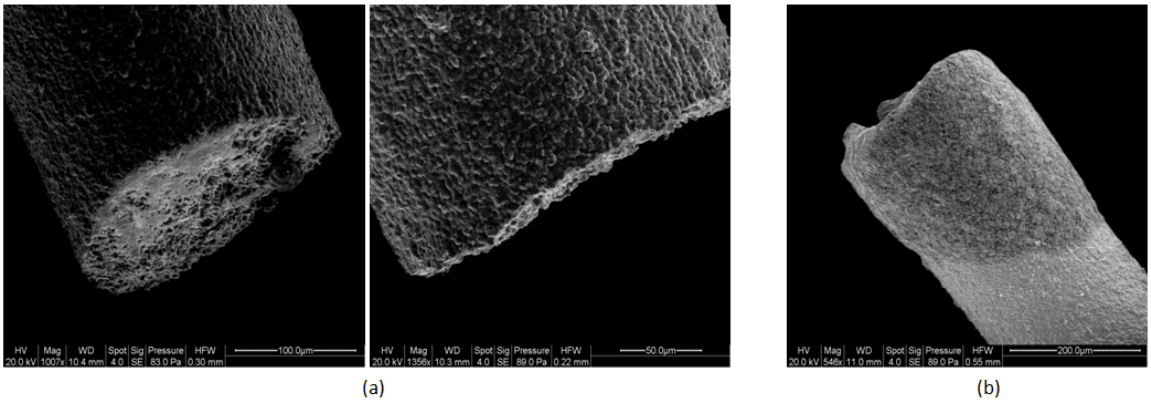

Figure D.1: PZT fiber partially fractured tip surfaces (a) and silver-tipped PZT fiber tip (b)

In order to help enhance electrical contact, it was proposed for the tips of the fiber to be dipped into a thin pool of silver ink to coat the ends. This coating would not only improve electrical contact, but would also conform better to the brass electrodes used in parallel electrode testing since the silver ink was a softer material than the PZT fiber. An example of a silver-tipped PZT fiber can be seen in Figure D.1 (b). As seen in this image, the silver coated the tip of the fiber well, but did not necessarily "smooth" the surface profile of the fiber tips. However, the silver ink profile, being a much softer material than the PZT fiber, easily conforms to the surface profile of the electrode indents. This creates a more "smooth" connection profile between the electrodes and the fiber, improving the electrical and mechanical connections.